



HAL
open science

Pulsed Laser Ablation in Liquid: towards the comprehension of the growth processes

Julien Lam

► **To cite this version:**

Julien Lam. Pulsed Laser Ablation in Liquid: towards the comprehension of the growth processes.
Other. Université Claude Bernard - Lyon I, 2015. English. NNT: 2015LYO10137 . tel-01226862

HAL Id: tel-01226862

<https://theses.hal.science/tel-01226862>

Submitted on 10 Nov 2015

HAL is a multi-disciplinary open access archive for the deposit and dissemination of scientific research documents, whether they are published or not. The documents may come from teaching and research institutions in France or abroad, or from public or private research centers.

L'archive ouverte pluridisciplinaire **HAL**, est destinée au dépôt et à la diffusion de documents scientifiques de niveau recherche, publiés ou non, émanant des établissements d'enseignement et de recherche français ou étrangers, des laboratoires publics ou privés.

Thèse de l'Université de Lyon:

Délivrée par:

Université Claude Bernard Lyon 1:

Ecole Doctorale de Physique et d'Astrophysique de Lyon

Diplôme de doctorat

(arrêté du 7 août 2006)

PULSED LASER ABLATION IN LIQUID: towards the comprehension of the growth processes

soutenue publiquement le 24 septembre 2015 par

Julien Lam

Sous la direction de **David Amans** en co-direction avec **Gilles Ledoux**

Devant le jury composé de:

- Président:** **Christophe Ybert**
Directeur de recherche, Université Lyon 1
- Rapporteurs:** **Andrew Orr-Ewing**
Professor, University of Bristol
- Jörg Hermann**
Directeur de recherche, Université Aix-Marseille
- Examineurs:** **Stephan Barcikowski**
Professor, Universität Duisburg-Essen
- Directeurs:** **David Amans**
Maître de conférence, Université Lyon 1
- Gilles Ledoux**
Chargé de recherche Université Lyon 1

Remerciements

Trois années, trois années dédiées à cette thèse et me voilà à la fin.

Mes premiers mots vont naturellement à David. Merci David, merci pour ton dévouement envers la science, merci pour la précision avec laquelle tu mènes ta recherche et pour ton appétence à partager ton savoir. Tu m'as appris sur la science bien évidemment mais aussi et surtout sur moi-même. Tu as été un remarquable directeur de thèse. Vient ensuite Gilles. Tu as toujours été là dans les moments de moins bien pour me rassurer, me conseiller et m'aiguiller. Ton recul et ta sérénité sont des qualités que j'aimerais posséder. Et oui, je ferai de mon mieux pour suivre ton conseil en gardant un oeil voire un pied dans l'expérimental. Je veux enfin remercier Christophe. Depuis la L3 et ce cours de mécanique quantique, les rencontres que tu m'as permises de faire et la bienveillance que tu m'as accordée sont des acteurs majeurs de mon envie de faire la recherche.

J'aimerais, de plus, remercier nos collaborateurs. Tout d'abord, Vincent, ton enthousiasme et ta gentillesse m'ont donné les forces pour avancer. Ensuite, Abdul, je te remercie pour tous tes conseils techniques (merci pour la conversion à Linux et à vim ;)) mais surtout pour tous le travail que tu as abattu. Sans toi, nous n'aurions jamais pu développer notre modèle de la nucléation. Je vais aussi remercier Samy pour l'intérêt que tu as manifesté pour notre travail. Et particulièrement, je veux souligner l'épatante manière que tu as de faire de la physique. Tu m'as appris que faire de la physique, c'est rendre simple les choses les plus compliquées. Enfin, je remercie Frederic et Karine pour l'expertise qu'ils nous ont apportée et pour leur soutien. Fred, je garderai en mémoire ton conseil juste avant l'oral et vais essayer au mieux de juste profiter. Quelques mots aussi pour nos autres collaborateurs, Camille, Arsène, Charly, Dimitry, Guillaume, Kristov, vous encadrer dans vos stages m'a beaucoup appris. Je vous remercie pour votre curiosité et votre souplesse dans le travail.

I also wanted to thank Jörg Hermann and Andrew Orr-Ewing for reviewing my manuscript. Both of your reports were very sharp and accurate. Thank you for delivering them in time. Then, I also acknowledge Stephan Barcikowski for having accepted to be member of my jury and for your challenging questions. I know that it is a long trip from Essen and I am happy you accepted to come to Lyon. Finally, my gratitude goes to Christophe Ybert. I am grateful for your commitment to my work and for your agreement to write the final report.

Je remercie aussi le laboratoire dans son ensemble. L'ambiance de travail y a été remarquable. Je me sens privilégié d'avoir pu travailler dans une telle atmosphère. A tous les membres du laboratoire qui ont participé de près ou de loin à mon quotidien, un grand

merci. En particulier, Florian, Jeremie, Amina et Stephan, je vous exprime ma sincère gratitude. Comment évoquer la joie d'aller au bureau sans évoquer les collègues doctorants? Adrien, Catherine, Simon, Menka, Daniel, Maxime, Ronan, Joseph, Alexandra, Florence... merci d'avoir été là. Finalement, c'est Nora et Antoine que je remercie. Vous m'avez rendu meilleur. Par nos discussions, vous m'avez poussé à réfléchir et à retirer mes ceillères. J'apprends encore mais vous m'avez montré une nouvelle voie.

Je souhaite remercier aussi ma famille pour le soutien permanent et pour m'avoir donné l'enseignement qui fait de moi ce que je suis aujourd'hui. Mes derniers mots vont pour Léonie. Tu m'as soutenu comme jamais personne ne l'avait fait. Ta force, tu me l'as transmise et c'est bourré d'optimisme que je me tourne vers notre avenir.

Contents

General introduction	1
1 On the use of Pulsed Laser Ablation in Liquid	5
1.1 A rapid and facile method to synthesize clean nanomaterials	6
1.1.1 Advantages of the method	6
1.1.2 Experimental implementations	7
1.2 A growth process requiring fundamental investigations	9
1.2.1 At the origin, a laser-matter interaction	9
1.2.2 Post-production processes	12
1.2.3 Intermediate time scales, a puzzling system	14
1.3 Conclusion	16
2 Synthesis of aluminum oxide nanoparticles	17
2.1 Techniques for material characterization	18
2.1.1 Transmission electron microscopy as specific characterization . . .	18
2.1.2 Overall characterization	19
2.2 Influence of the laser parameter towards the synthesis results	20
2.2.1 First attempts using a nanosecond ultraviolet laser	20
2.2.2 α -Al ₂ O ₃ obtained from picosecond infrared lasers	21
2.3 Conclusion	25
3 Underwater plasma spectroscopy, implementation and fundamental consequences	27
3.1 Plasma spectroscopy to probe the first time scales	28
3.1.1 The plasma, a source of light	28
3.1.2 Thermodynamic characterization of the plasma	29
3.1.3 Experimental setup	30
3.2 Investigation on the underwater aluminum oxide plasma	31
3.2.1 Challenges of plasma spectroscopy underwater	31
3.2.2 Electron density	32
3.2.3 Rotational temperature	34
3.2.4 Temporal evolution of the chemical composition	36
3.3 Challenges for equilibration in molecular plasma	40
3.3.1 Electronic equilibration, the McWhirter criteria	41
3.3.2 Rotational equilibration	46
3.3.3 Perspectives on the role of chemical reactions	50
3.4 Conclusion	56
4 A microscopic approach to the nucleation of nanoparticles	57
4.1 Classical nucleation theory and its limitations	58
4.1.1 Nucleation core	58

4.1.2	Beyond classical nucleation theory	60
4.2	Computational chemistry to investigate the intermediate clusters	62
4.2.1	Computational methods	63
4.2.2	The case of aluminum oxide clusters	66
4.3	A thermochemistry model for the gas composition and its experimental justifications	70
4.3.1	Theoretical model	70
4.3.2	Application for the ablation in air	73
4.4	An extension towards lower temperature	75
4.5	Conclusion	77
5	Out-of-equilibrium hydrodynamics of the expanding bubble	79
5.1	The shadowgraphy technique	80
5.1.1	Experimental setup	80
5.1.2	A review of the previous works	81
5.1.3	The Rayleigh-Plesset model of the bubble dynamics	83
5.2	The bubble dynamics in three different solvents	84
5.2.1	Qualitative considerations and consequences	84
5.2.2	Thermodynamic analysis	87
5.3	Conclusion	91
	Conclusion and perspectives	93
	Bibliography	97
	Résumé en français	113
	List of publications	117

A ceux qui ont su éveiller la curiosité...

General introduction

MANKIND has repeatedly wished for the biggest and the smallest possible. Such a dream led to wonders like the Eiffel Tower, the Pyramids and the Great Wall of China. On the other hand, the quest for smaller contributed to the growing interest towards nano-materials. The prefix nano was originally derived from the Greek word $\nu\tilde{\alpha}\nu\omicron\zeta$ which means "dwarf". It was only in 1960 that it had been officially used to designate the one billionth prefix. Since then, one calls nano-material any material possessing at least one of its dimensions sized between 1 and 1000 nanometers. While controversial for its hazardousness, one cannot deny the infinite possibilities offered by this new category of materials. Nowadays, nano-materials are already implemented in a variety of technologies. In particular, their small size can be used to probe confined length scales such as in medical diagnosis applications. In addition, at nanoscale, the surface effects are enhanced thus allowing to reach the scope of energy conversion or catalysis.

Besides the very peculiar physical properties of these materials, one of the remaining issue concerns the material design itself. Indeed, it is still challenging to produce rapidly, efficiently and accurately a nano-material. In order to engage in industrial applications, the nanoparticles must be generated at low cost and at high production rate. In the meantime, properties of the outcomes such as crystallinity, shape or size distribution ought to be controlled. Nowadays, lots of techniques are already employed to generate nanoparticles. On the one hand, there are various methods using chemical processes such as co-precipitation and sol-gel. On the other hand, physical techniques are also regularly used. One can mention for example laser deposition or laser pyrolysis. In these cases, one often adopts a bottom-up approach where a purely atomized or ionized gas recombines into molecules, clusters and nanoparticles. The first step is then to reach out-of-equilibrium conditions leading to an unstable system composed of atoms and ions. In a second step, the system is cooled down to cause nucleation and growth of the nano-material.

This thesis work is dedicated to pulsed laser ablation in liquid (PLAL) which is an original technique to synthesize nanoparticles. When a pulsed-laser is focused into a solid target immersed in water, the material is evaporated and turns into a plasma. Nucleation and growth occur in the liquid and nanoparticles are obtained. This method is versatile

due to the wide range of accessible materials. Moreover, the nanoparticles are directly stabilized in the solvent so there is no need for complexing agents and the nanoparticles are therefore described as ligand-free. However, various processes can occur during the synthesis and accordingly PLAL incorporates complicated mechanisms. Yet, enhancing the PLAL performances requires to overcome complexity in the fundamental understanding of these out-of-equilibrium processes involving multiple length and time scales. As a starting point, the laser interacts with the bulk target thus creating a hot and dense plasma. Thereafter, numerous authors reported the formation of an expanding bubble from which nano-materials are released. The aim of my thesis is to build an accurate understanding of these several components. I, indeed, implemented methods from different domains of expertise to probe the physical and the chemical mechanisms underlying the use of pulsed laser ablation in liquid.

In this thesis manuscript, I will begin by a general description of pulsed laser ablation in liquid where I will try to detail the main features of the technique, discuss the influence of experimental parameters and introduce challenges regarding the comprehension of PLAL. My second chapter will be related to the synthesis of aluminum oxide nanoparticles. I will motivate our work on this specific material and show that $\alpha\text{-Al}_2\text{O}_3$ nanoparticles can be obtained by PLAL under specific experimental conditions. The synthesized nanoparticles will then be used for pressure sensing applications. These promising results encouraged us to explore fundamentals of the growth processes occurring in PLAL. In the third chapter, I will therefore describe our work on underwater plasma spectroscopy as a tool to probe the very first time scales. In particular, we measured the chemical composition, the rotational temperature and the electronic density as a function of the time. This work also raised numerous questions towards the temperature equilibration inside a plasma composed of diatomic molecules. After investigating the first time scales, we used computational chemistry to build a model for the nucleation of the nanoparticles. We calculated stable structures of Al_xO_y and their associated thermodynamic properties. From these data, the chemical composition of a gas made of aluminum and oxygen atoms were calculated as a function of temperature, pressure, and aluminum to oxygen ratio. After showing the accuracy of this approach to reproduce experimental results obtained from laser induced plasma, we extended the calculation to lower temperature and followed the birth of alumina first seeds. This is the scope of my fourth chapter. For PLAL, this modeling requires a quantitative measurement of the bubble chemical composition especially the ratio between oxygen and aluminum atoms and of the bubble temperature. Therefore, in my last chapter, I will introduce our results on the bubble hydrodynamics. First, bubble images were acquired using an ultra-fast camera to measure an entire dynamical evolution for each laser shot thus overcoming reproducibility issues. Furthermore, we developed an analytical approach

based on cavitation models to demonstrate that the system evolution is mostly inertial and adiabatic. We deduced quantitative thermodynamic properties inside the bubble and proved that it is mainly composed of solvent molecules whose number does not vary significantly during the bubble evolution.

Chapter 1

On the use of Pulsed Laser Ablation in Liquid

"Those who do not remember the past are condemned to repeat it."

George Santayana

Contents

1.1 A rapid and facile method to synthesize clean nanomaterials . . .	6
1.1.1 Advantages of the method	6
1.1.2 Experimental implementations	7
1.2 A growth process requiring fundamental investigations	9
1.2.1 At the origin, a laser-matter interaction	9
1.2.2 Post-production processes	12
1.2.3 Intermediate time scales, a puzzling system	14
1.3 Conclusion	16

ON May 16, 1960, Theodore H. Maiman designed the first pulsed-laser using a ruby crystal and emitting at 694 nm [1]. Since then, lasers have been widely used for fundamental research but also for material processing. Laser-assisted fabrication of nanomaterials became indeed one of the various applications of pulsed-lasers [2–5]. To our knowledge, the first article involving underwater laser ablation for a nanomaterial synthesis was written by Lida et al. [6]. In this work, the aim was to generate submicronic particles for solid sampling applications. Since then, the technique has evolved drastically [7]. In this chapter, I will introduce advantages of the method for nanoparticle synthesis and describe how PLAL is currently carried out in most experiments. Then, I will also emphasize fundamentals of the mechanisms underlying PLAL and techniques usually employed to explore them.

1.1 A rapid and facile method to synthesize clean nanomaterials

In practice, PLAL consists of the use of an intense laser focused onto a solid target immersed in a liquid solvent. In this section, we will review the main advantages of the method towards nanoparticle synthesis and discuss its practical implementation.

1.1.1 Advantages of the method

Numerous techniques have been designed to generate nanoparticles. Chemical synthesis methods include co-precipitation methods, sol-gel methods or solvothermal processes [8]. On the other hand, physical approaches, such as pulsed-laser deposition [9], mechano-synthesis [10] and flame spray pyrolysis [11] are also used to synthesize nanoparticles. In comparison with these methods, we believe that PLAL possesses fundamental advantages because PLAL combines the physical processes of the laser-matter interaction with chemical mechanisms due to the use of liquid solvents.

Productivity Using flame spray pyrolysis, Groehn et al. obtained up to 500 g/hour [12]. In PLAL, the production rate is not there yet but it can still scale up to industrial applications. Sajti et al. proved the ability to reach few grams per hour synthesis [13]. In this article, using a kilohertz laser, they improved significantly the efficiency of the method. In general, PLAL nanoparticles are already sold by the company STREM and are competitive with respect to pricing and productivity.

Versatility Chemical methods benefit from a long period of trials before the synthesis results are optimized to reach the desired nanoparticle. In PLAL, trials for any novel material are quite straightforward. Although the synthesis results may sometimes be different from those expected, at first, one only needs to experiment with the corresponding target. As a consequence, PLAL is a very versatile technique. Indeed, a wide range of nanomaterials have been synthesized with this method eg. metals (Au, Ag, Pt, In, Fe, W, Cu and their alloys [14–16]), oxides (TiO_2 , SnO_2 , Eu_2O_3 , CeO_2 , LiCoO_3 , CeTbO_3 [17–19]), doped materials ($\text{Y}_2\text{O}_3 : \text{Eu}^{3+}$, $\text{Lu}_2\text{O}_2\text{S}:\text{Eu}^{3+}$, $\text{Gd}_2\text{SiO}_5:\text{Ce}^{3+}$, $\text{Lu}_3\text{TaO}_7:\text{Gd}^{3+}$, $\text{Y}_3\text{Al}_5\text{O}_{12}:\text{Ce}^{3+}$, $\text{Gd}_2\text{O}_3:\text{Eu}^{3+}$, $\text{Y}_2\text{O}_3:\text{Er}^{3+}$ [20–22]) and allotropes of carbon [23, 24].

Applications On the one hand, contamination from abrasive material can occur in milling and grinding methods. On the other hand, in chemical techniques, surfactants

are often required to stabilize the colloidal solution. Therefore, these two types of methods are limited in terms of purity. In PLAL, the nanomaterials are produced directly in the liquid without impurities and without any use of complexing agents. The surface effects are therefore significantly improved allowing for enhanced catalytic properties [25]. This attractive feature combined with the use of bio-compatible environment such as pure water enables one to tackle biological applications. Duran et al. and Petersen et al. studied for example the use of gold nanoparticles in biological environment [26, 27]. Finally, interaction with the liquid allows one to tune the results of the synthesis. For instance, the stability and the size distribution can be improved by adding surfactants in the liquid. In the work of Amans et al., 2-[2-(2-methoxyethoxy)ethoxy]acetic acid (MEEAA) was added in the water [21]. As a consequence, aggregation was prevented and the mean radius of Y_2O_3 nanoparticles went from 6.4 ± 2.9 nm to 1.9 ± 0.35 nm with a ligand concentration of 10^{-2} mol.L $^{-1}$. Also, the particles composing the solvent can change the chemical composition of the final products. C_3N_4 nanoparticles were synthesized using a graphite target in aqueous ammonia solution (NH_3) [28, 29].

To summarize, PLAL enables one to synthesize rapidly nanoparticles for a large variety of materials. This capability can be employed to build novel materials suitable for specific applications. Moreover, the technique provides highly pure nanomaterials of interest in catalytic and biological applications. For further details, please refer to reviews published in the past few years [30–32].

1.1.2 Experimental implementations

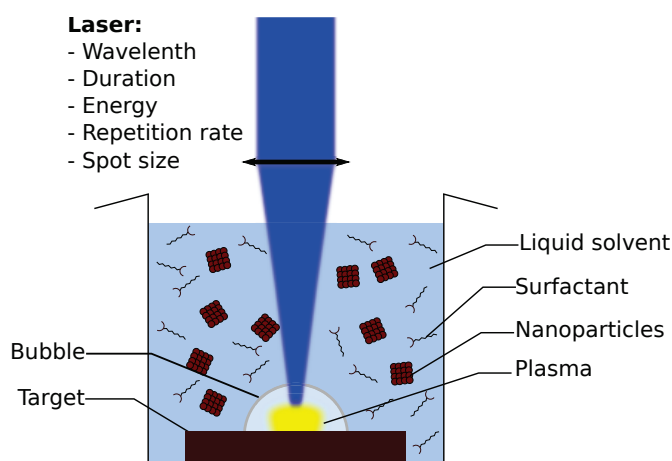


FIGURE 1.1: Sketch of the main experimental features of PLAL.

Several experimental parameters can be tuned to control the results of the synthesis.

Bulk target - The main components for the nanoparticle formation are provided by the target material. Yet, composition and crystal phase of the resulting nanoparticles do not necessarily match the target ones. Using a chromium target, for instance, PLAL can yield to a mixture of dodecahedral and tetragonal Cr_3O_4 but also to corundum-type Cr_2O_3 [33]. Similar phenomena are found in most base metals such as zinc, titanium and iron [34–37]. Underwater ablation of graphite carbon also exhibit a large variety of results eg. diamond, amorphous, graphite particles [23].

Laser parameters - The results of the synthesis can be affected by laser characteristics. First, increasing the repetition rate improves the method productivity since more laser shots are applied for the same experimental time. Then, ultra-violet (UV) and infra-red lasers (IR) are absorbed differently by the target. Tsuji et al. showed that the ablation efficiency increases with the wavelength [38] since less energy is absorbed by already synthesized nanoparticles and solvent molecules. The laser fluence also plays an important role. Indeed, the amount of ablated nanoparticles may increase with pulse energy as shown by Mafune et al. for example [39]. Moreover, the size distribution and the average size can be enlarged by higher laser energy in the case of platinum target [40]. In opposition, Amans et al. also demonstrated that in the case of oxides in an aqueous solution of complexing molecules, there is only a slight influence of the laser fluence on the size distribution [21]. Finally, different crater morphologies can be observed for different pulse durations.

Solvent composition - Different solvents can be used in PLAL eg. water, ethanol, acetonitrile, dimethyl-formamide, toluene. The ablation of gold target in toluene is a good example of solvent influence since smaller nanoparticles (< 1 nm) embedded in graphitic matrix are obtained [41]. Iron nanoparticles are also affected by solvent composition because it is not a noble metal. In ethanol, for example, both Fe_3O_4 and FeC_3 are obtained [36]. Similarly, numerous oxides have been obtained when ablating pure metal targets [34–37] in water. Moreover, surfactants can be added to the solvent in order to tune the results of the synthesis. We already mentioned the use of MEEAA for oxide nanoparticles but, for metallic ones, sodium dodecyl sulfate (SDS) are also used to reduce the size distribution [39].

A review on this matter can be found in the article written by Amendola et al. [32].

1.2 A growth process requiring fundamental investigations

The very wide variety of synthesis results suggests that PLAL includes very complex growth mechanisms. This particularity may emerge from the ability to mix both laser-matter interaction and solution chemistry thus resulting in a process which combines various time scales. The figure 1.2 summarizes the processes occurring in pulsed laser ablation in liquid along with the corresponding time scales. The laser interacts with the material creating a hot and dense plasma. When the plasma is no longer optically active, an expanding bubble is observed. At the bubble collapse, nanoparticles are released in the liquid environment.

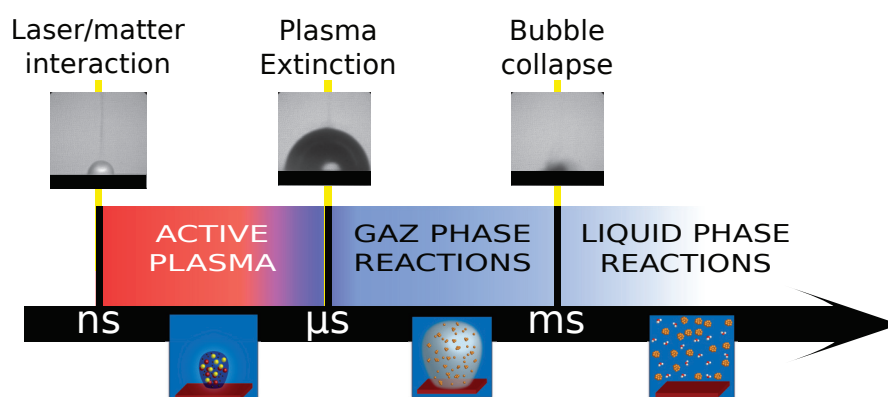


FIGURE 1.2: Diagram reviewing the processes occurring in pulsed laser ablation in liquid.

We will start our description with the very beginning of the process, the laser-matter interaction, and very end, the liquid phase reaction. Then, we will focus on the intermediate time scales and discuss their complexity.

1.2.1 At the origin, a laser-matter interaction

Over short time scales, the laser interacts with the material and ablation, ie. mass removal can occur. In ambient atmosphere, the laser-matter interaction has been frequently studied because it concerns lots of different applications such as laser surgery, pulsed laser deposition and surface nano/microstructuring [9, 42, 43]. In water, the mechanisms should remain essentially the same.

The absorption and relaxation process The laser-matter interaction arises from the coupling between (i) the laser parameters which are the pulse duration τ_L (eg. femtosecond, picosecond, nanosecond), the wavelength λ_L (eg. infrared, ultraviolet) and

the intensity F (eg. $10^9 - 10^{13} \text{ W/cm}^2$) and **(ii)** the target features which are the optical absorption, the mechanical properties and the thermal conductivity. First, the laser photons ought to be absorbed. The absorption is granted by electrons in metals. In insulators and semi-conductors, only multiphotonic absorption can promote electrons in the conduction band thus creating electron-hole pairs. But, there can be defects in the material such as dopants, vacancies, mechanical or thermal constraints. They would thus favour the absorption process by occupying additional energy levels in the band gap. In terms of time scaling, absorption takes place after 10^{-14} s [44]. This value is lower than the pulse duration commonly used except for femtosecond lasers. Therefore, we can consider the absorption as instantaneous. Then, the hot carriers can transfer their energy to the target lattice leading eventually to a solid-liquid phase transition. This energy transfer leads to an equilibrium on a timescale $\tau_E = 10^{-12} - 10^{-11} \text{ s}$ [44]. When τ_E is higher than the pulse duration, τ_L , non-thermal processes can occur. Otherwise, the system is mainly driven by thermal processes.

The thermal processes In thermal processes, the mass removal occurs from equilibrium phase transition and could be probed qualitatively through thermodynamic considerations. There are in general three kinds of thermal processes:

- *Evaporation* refers to the transition from a condensed phase (solid or liquid) to vapour by the emission of particles (ions, atoms, molecules) from the outer surface. However, the efficiency of this process becomes significant only after few tens of nanoseconds. As a consequence, for ablation, no vaporization effects must be taken into account.
- *Normal boiling* consists in the heterogeneous nucleation of a gas bubble after the solid target is turned into a superheated liquid phase by the hot carrier relaxation. The creation of the bubble is allowed by disturbances in the superheated liquid system such as gas or solid impurities, structural defects or the surface of the solid. Then, to induce mass removal, the bubble needs to diffuse along the system. According to Miotello et al., the diffusion time is not short enough to allow quantitative mass removal [45].
- *Phase explosion*, also called *explosive boiling*, relies on the idea that if the solid is turned into a superheated liquid at a temperature sufficiently near the critical boiling temperature, then homogeneous nucleation can occur and lead to the creation of vapour bubbles. Calculating the rate of homogeneous nucleation, it has been shown that this thermal process is the most favourable for mass removal [45].

For more detailed information, Miotello et al. discussed very carefully the relevance of these three mechanisms [45].

The non thermal processes When the thermal processes are too slow, non-thermal processes, eg. photomechanical, are predominant. Bonding electrons can turn into non-bonding electrons and cause disorder in the lattice structure. Two major types of non-thermal mechanisms are then usually considered:

- *Spallation* occurs when entire layers of the material are ejected. The laser-matter interaction causes mechanical stress in the target lattice. This stress can induce the generation of shock waves thus creating fractures inside the target. When the pressure waves are powerful enough, spallation occurs.
- *Fragmentation* is the process in which the solid target decomposes into numerous clusters. To create such fragments, the elastic stored energy is equal to the energy necessary to have it isolated. The elastic energy is then converted into surface energy and a physical detachment occurs.

For a more detailed description, please refer to the study conducted by Perez et al. [46].

The case of nanosecond lasers The balance between the thermal and non thermal mechanisms still constitutes an open problem. It is hard to address in general since it depends strongly on the material and the laser parameters. Yet, Lorazo et al. published two articles in which they used molecular dynamics simulation on the laser ablation on a silicon target [47, 48]. They derived the thermodynamic trajectories of the ablation process for different irradiation times. First, especially in the case of nanosecond lasers, they showed that the solid melts to liquid at the equilibrium melting temperature. Then, depending on the liquid-vapor equilibration time, τ_{LV} , the system can either be dragged into explosive boiling ($\tau_L < \tau_{LV}$) or follow slowly the binodal curve leading to the liquid-vapor phase transition ($\tau_L > \tau_{LV}$). In general, most authors agree that thermal processes mainly drive the laser-matter interaction for nanosecond lasers since the heating of the material is slow enough to let the excitation decay [49, 50]. But again, to discriminate between each path is challenging because of the variety of lasers and targets used. Moreover, the light absorption is an evanescent process because it is driven by Beer-Lambert law. As a consequence, the fluence gradually decays inside the material and it is most likely that all the processes occur at the same time but at different depths. In our working conditions, granted that a plasma is observed after few nanoseconds, we may leave behind the laser-matter interaction and focus on the following processes.

1.2.2 Post-production processes

At the end of the PLAL process, when the nanomaterial is finally in the liquid, it can still suffer from diverse modifications.

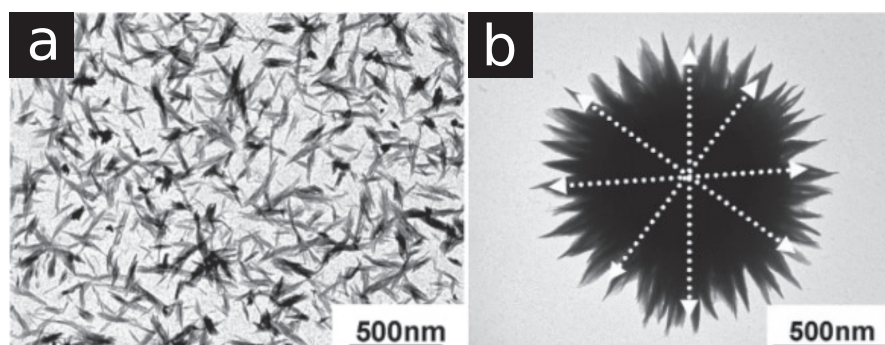


FIGURE 1.3: TEM images of C_3N_4 nanoparticles produced by PLAL after different irradiation times (a) 1 hour and (b) 3 hours. Figures are reprinted from Yang et al. [28].

The concentration of the solution can be raised by increasing the irradiation time. Then the laser can pass through already synthesized nanoparticles, resulting in a re-ablation process which can induce modification of the nanoparticles's morphology. At low fluences, the laser can reorganize nanomaterials. In figure 1.3, the leaflike structure aggregates to flower structures creating a singular network of nanoparticles [28]. For higher fluencies, the laser can also fragment the nanostructures. Besner et al. proved that the size of gold nanoparticles obtained by PLAL can be reduced [51]. In figure 1.4, we can see a shift and a sharpening of the size distribution after 2 hours of laser fragmentation. The absorption properties and the laser fluence are thus two significant parameters.

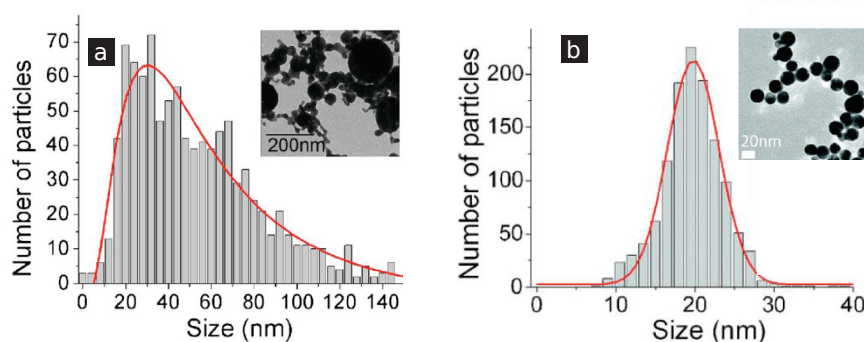


FIGURE 1.4: Size distribution and corresponding TEM images of gold nanoparticles obtained by PLAL (a) and after 2 hours of laser fragmentation by a supercontinuum laser (b). Figures are reprinted from Besner et al. [51].

Among the non-optical processes, as-produced nanoparticles can for example interact with each other. This mechanism causes the aggregation of the particles leading to polycrystal nanostructures. Mafune et al. proposed the use of surfactants that would attach to surfaces of the original nanoparticles thus avoiding interparticle contacts [52]. In figure 1.5, TEM images and the corresponding size distribution of silver nanoparticles synthesized by PLAL are reported for different concentrations of sodium dodecyl sulfate (SDS). The average diameter decreases with the SDS concentration. An other influence of the chemical processes concerns the interaction between the ablated material and the solvent molecules. For example, zinc oxide (ZnO) and zinc hydroxide (Zn(OH)₂) particles were obtained in water by Zeng et al. while pure zinc was used as target [17]. More interestingly, they have been able to favour one phase or another by varying the concentration of SDS.

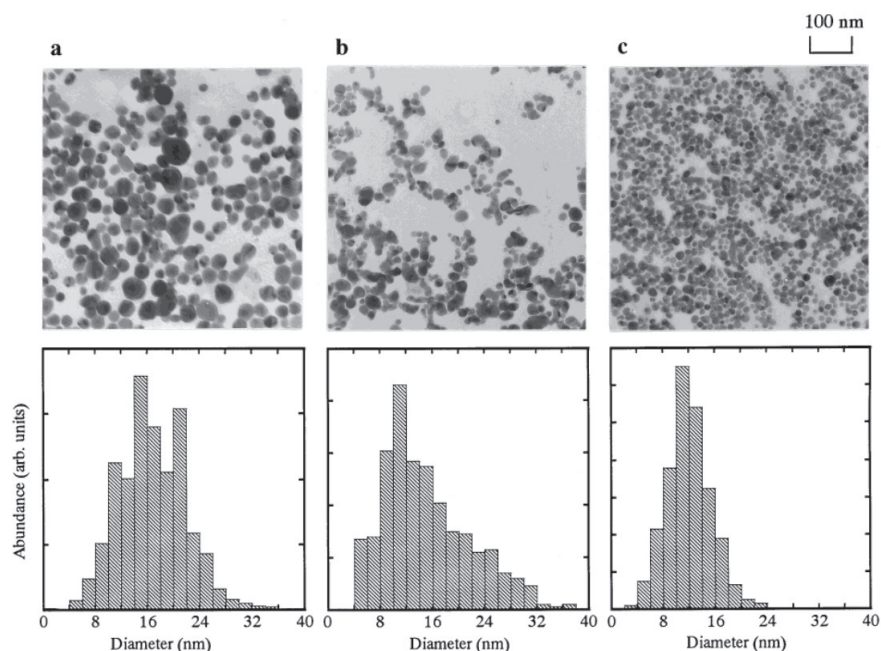


FIGURE 1.5: Size distribution and corresponding TEM images of silver nanoparticles synthesized by PLAL in water at different concentrations of $C_{12}H_{25}OSO_3Na$, a-c are 0.003, 0.01, and 0.05 M, respectively. Figures are reprinted from Mafune et al. [52].

Very recently, Gokce et al. investigated the aggregation processes from 1 s to 2 min [53]. Metal targets were ablated and nanoparticles exhibiting plasmonic properties were thus obtained. By probing the plasmon peak as a function of the time, the ripening process was characterized quantitatively as a two-step growth mechanism for the as-produced nanoparticles.

1.2.3 Intermediate time scales, a puzzling system

As discussed previously, during the very first time scales, PLAL is mostly governed by laser-matter interaction and exhibits approximately the same properties than in ambient atmosphere. Over the very long time scales, post-production processes may rather dictate morphological alteration of the synthesized particles. However, the intermediate time scales which go from nanoseconds to milliseconds are very poorly documented due to the difficulty to address experimentally such short time scales. Yet, several research groups have been trying to investigate the very transient nature of the PLAL mechanisms using various experimental techniques [54–58].

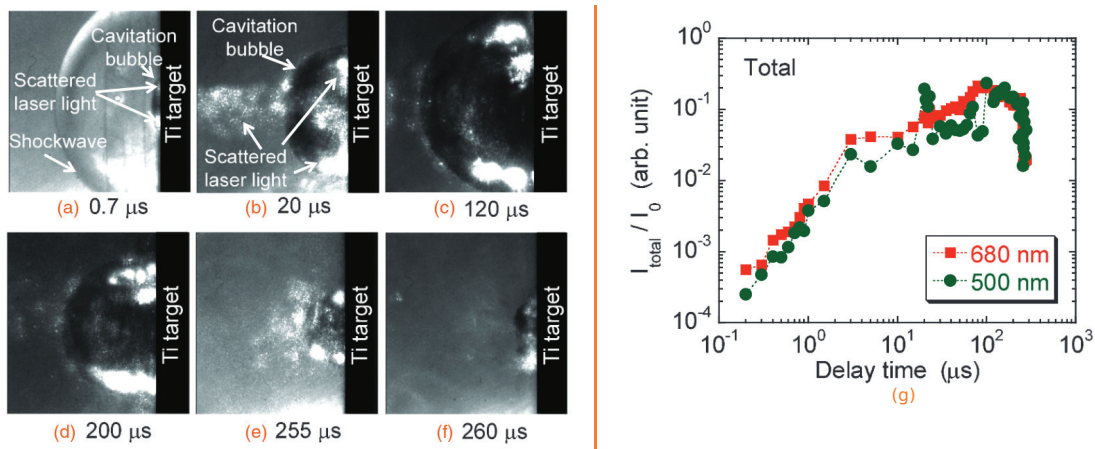


FIGURE 1.6: Superimposed images of laser-light scattering and shadowgraph imaging at various delays after the ablation laser pulse. Temporal evolution of the total scattered intensity (g) at different probe wavelengths. Figures are reprinted from Soliman et al. [59].

For instance, laser-light scattering was used by Soliman et al. [59]. An optical parametric oscillator (OPO) laser was synchronized at a specific time delay after the ablation laser pulse to illuminate above the target. This way, scattered light was observed outside the bubble and was identified as originated from accumulated nanoparticles already present in the chamber [See figure 1.6(b)]. More interestingly, inside the bubble, scattered light was also observed and was associated to the produced nanoparticles. The temporal evolution of the total intensity (I_{tot}) in the measured images was also plotted [See figure 1.6(g)]. I_{tot} increases until few microseconds accounting for a very rapid growth of the nanoparticles in the bubble. However, in this study, only particles bigger than hundreds of nanometers were probed because of sensitivity issues.

To overcome this difficulty, Barcikowski's group published two papers using small angle X-ray scattering (SAXS) to investigate the size distribution of the particles located in the bubble [54, 55]. Fitting the scattering curves at small angle, they characterized the

size distribution inside the bubble and distinguished two characteristic sizes, one around 8-10 nm and an other one of about 45 nm. In their most recent publication, they added a temporal evolution study and did not observe any significant change in the size [See figure 1.7]. Unfortunately, this method does not access particles smaller than a few nanometers.

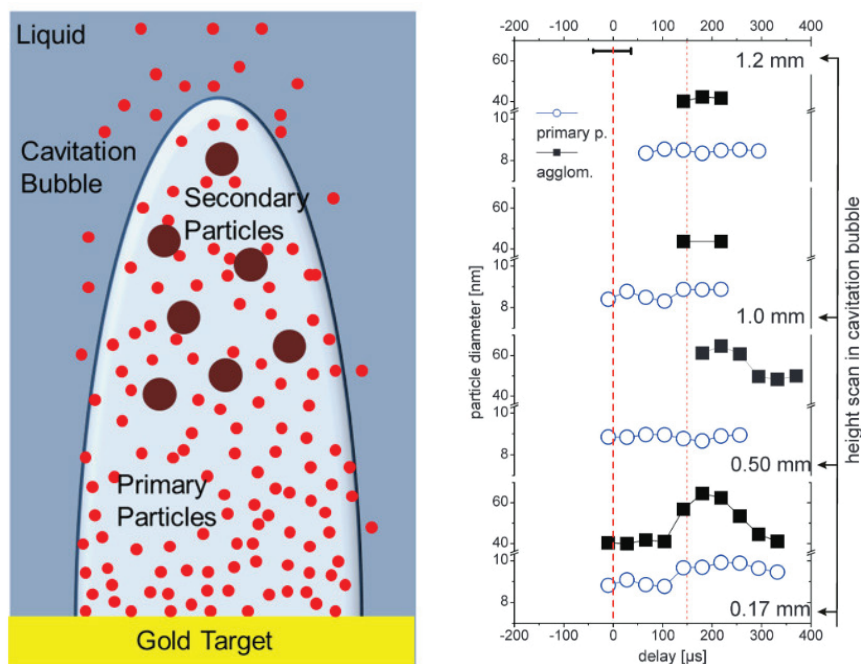


FIGURE 1.7: On the left, a sketch of measured particles in pulsed-laser ablation in liquid. On the right, the temporal evolution of the particle diameter at different heights. Figures are reprinted respectively from Ibrahimkuty et al. and from Wagener et al. [54, 55].

1.3 Conclusion

Laser ablation in liquid is a method to synthesize nanoparticles directly from a bulk target. The method proved its efficiency on various types of materials and its ability to reach numerous applications thanks to very specific features. While laser-matter interactions and liquid-phase processes have already been discussed extensively, we showed that the intermediate time scales still require lots of efforts. We mentioned various works on the size distribution as a function of the time. Yet, the chemical composition of the system is not really addressed in the literature. For noble metal targets, one expects only metal-metal interaction while for usual metal and for oxide targets, the studied system is at least composed of two interacting types of atoms and solvent must influence greatly the system. Especially, no consensus has been established about the proportion of solvent to ablated molecules inside the plasma and the bubble. Also, we rarely find quantitative measurements of the thermodynamic properties during these intermediate time scales. The pressure, the temperature and the density ought to be probed to achieve a better understanding of the growth processes. We will work on this matter during the following chapters by first taking the example of aluminum oxide ablation.

Chapter 2

Synthesis of aluminum oxide nanoparticles

"Perhaps the world progresses not by maturing, but by being in a permanent state of adolescence, of thrilled discovery."

Julian Barnes

Contents

2.1	Techniques for material characterization	18
2.1.1	Transmission electron microscopy as specific characterization	18
2.1.2	Overall characterization	19
2.2	Influence of the laser parameter towards the synthesis results	20
2.2.1	First attempts using a nanosecond ultraviolet laser	20
2.2.2	α -Al ₂ O ₃ obtained from picosecond infrared lasers	21
2.3	Conclusion	25

FOR most of our work, we used aluminum oxide Al₂O₃ as a model material. The choice of such a material was motivated by two major reasons. First of all, Al₂O₃ has a very complex phase diagram. At standard temperature and pressure, the most stable crystallographic phase is the α -Al₂O₃ phase which corresponds to a tetragonal phase. However, McHale et al. demonstrated that γ -Al₂O₃ phase has a lower surface energy and is then, more stable when reducing the size of the particles to nanoscale (<10 nm) [60, 61]. It is interesting to see if PLAL could overcome this difficulty. Using a kilohertz infra-red laser, Sajti et al. already demonstrated the synthesis of α -Al₂O₃ nanoparticles but the radius was around 30 nm [13]. Kumar et al. also worked on aluminum oxide but no crystallographic analysis was performed [62]. Yet in general, the PLAL on aluminum target led to γ -Al₂O₃ [63, 64] or hydroxide [65]. To favor the aluminum oxide stoichiometry, we used an Al₂O₃ target and tried to obtain α -Al₂O₃ nanoparticles.

Also, in terms of applications, α -Al₂O₃, in macroscopic scale, possesses a very interesting physical property which seemed appealing to transfer at the nanoscale. Indeed, when

doped with chromium, aluminum oxide is widely used as a probe for high pressure measurements because the $\alpha\text{-Al}_2\text{O}_3\text{:Cr}^{3+}$ fluorescence emission is highly dependent on the pressure. In diamond anvil cell, $\alpha\text{-Al}_2\text{O}_3\text{:Cr}^{3+}$ is exploited to measure the pressure inside the cell [66]. In different application areas, such as microfluidic or phase transition thermodynamic, it could be relevant to measure the pressure at a nanometric scale. For that purpose, it would be useful to synthesize $\alpha\text{-Al}_2\text{O}_3\text{:Cr}^{3+}$ nanoparticles. One remaining difficulty would be to know if the dopant, here chromium ions, remains in the nanoparticle during the PLAL synthesis. The cases of europium, cerium and erbium have already been investigated in previous articles [20–22] where the dopant indeed stays in the nanoparticle. To our knowledge, no work with aluminum oxide doped with chromium has been reported so far.

In this chapter, I will first review methods employed to characterize the synthesized materials. Then, I will describe results we obtained for $\text{Al}_2\text{O}_3\text{:Cr}^{3+}$ synthesis using separate methods of PLAL. Finally, I will detail how the nanoparticles can be used as pressure sensors.

2.1 Techniques for material characterization

Once the synthesis is performed, material characterization ought to be accomplished. Two approaches can be distinguished depending on the ability to characterize specifically one nanoparticle or to determine overall properties.

2.1.1 Transmission electron microscopy as specific characterization

We used transmission electron microscopy (TEM) to characterize the nanoparticles. In practice, after two hours of sedimentation, a droplet of the synthesized upper part is deposited on a TEM grid made of 300-mesh copper grids covered with a holey carbon film. TEM experiments are carried out on a JEOL 2010F microscope operating at 200 KV. High resolution images are acquired using a Gatan Orius 200 camera. Electronic diffraction patterns are analyzed with the Digital Micrograph software from Gatan. Energy Dispersive X-Ray Spectroscopy (EDS) characterizations are simultaneously performed using an SDD Xmax80 detector from Oxford Instruments. The interreticular distances are measured on the fast Fourier transforms (FFT) of the picture. We use the International Centre for Diffraction Data to identify the synthesis results.

2.1.2 Overall characterization

While very efficient to characterize nanoparticles one at a time, TEM may suffer from inhomogeneity in the sample characteristics and must be complemented by overall characterization techniques.

Dynamic light scattering In dynamic light scattering (DLS), a laser illuminates the liquid sample in which nanoparticles are moving through Brownian motion. The scattered light fluctuates in time with a frequency driven by the nanoparticles mobility. Since the velocity depends on the particle size in Brownian motion, collecting the scattered light one can reach the size distribution. For a more detailed description of DLS, please refer to Pecora's article [67].

For PLAL, DLS is scarcely used because the technique usually lacks the accuracy for poly-dispersed samples and for non spheroidal particles. Indeed, big particles scatter more light than smaller ones. Consequently, the smallest particles can hardly be observed in DLS leading to an overestimation of the size distribution as demonstrated by Petersen et al. [27]. Moreover, when aggregation occurs, DLS can only probe the hydrodynamic radius thus overestimating the absolute size of the produced nanoparticles.

X-ray crystallography The sample is irradiated with X-ray beams that are scattered by the crystal lattice following the Bragg's law:

$$2d \sin \theta = \lambda \quad (2.1)$$

where d is the interreticular distance, θ is the scattering angle and λ is the X-ray wavelength. Therefore, measuring the amount of scattered light as a function of the scattering angle enables one to determine crystal structures by comparing peak positions to databases such as International Centre for Diffraction Data (ICDD).

In our case, liquid samples are dried using lyophilization techniques to obtain a powder which can then be characterized. X-ray powder diffraction patterns were then recorded at room temperature on a Bruker D8 Advance diffractometer equipped with a sealed Cu X-ray tube and a linear LynxEye detector. Yet, for an accurate measurement, the quantity of powder must be important and it is not always possible with PLAL especially with a low repetition rate lasers.

Photo-luminescence spectroscopy When a material is excited by sufficiently energetic photons, it may absorb the light and re-emit it with a different wavelength. This is called

the photo-luminescence property. It can be exploited to characterize material since each material exhibits specific absorption and emission features. The luminescence may originate from the intrinsic properties of the crystal but can also arise from rare earths when the crystal is doped. In this second case, the energy levels of the doping material are located right in the middle of the intrinsic band gap and allows luminescence de-excitation.

In practice, it is usually complicated to distinguish the nanoparticle emission from a microparticle's emission since the bigger the particle is the more it absorbs and emits light. In PLAL, non-thermal processes may lead to microparticle synthesis and luminescence characterization is then no longer accurate for the characterization of the nanoparticles.

In summary, none of the characterization techniques can be used alone. An accurate characterization consists of the combination of all these techniques.

2.2 Influence of the laser parameter towards the synthesis results

2.2.1 First attempts using a nanosecond ultraviolet laser

Figure 2.1 is a scheme of the experimental setup that was employed for this work. We used the third harmonic of a Nd:YAG laser ($\lambda = 355 \text{ nm}$, $\tau = 5 \text{ ns}$, $f = 10 \text{ Hz}$) The laser passes through four dichroic mirrors to eliminate any first and second harmonics. The beam is then expanded to avoid ablation on the liquid surface. The diameter of the entrance beam is equal to 20 mm and the ablation lens is a 150 mm focal length. Right after the ablation lens, the laser energy is equal to $40 \pm 7 \text{ mJ}$. The solid target is immersed into water and moved via stepping motors to prevent from re-ablating on a same spot.

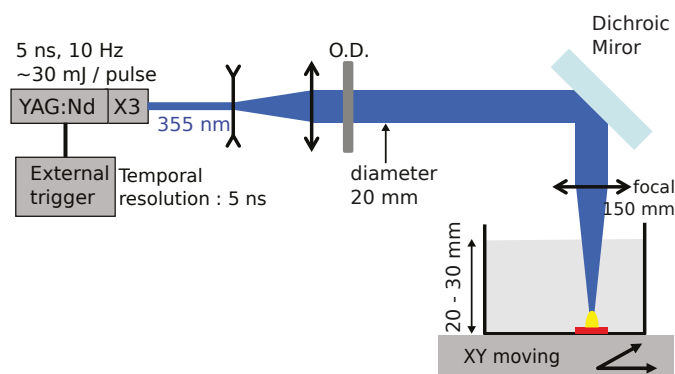


FIGURE 2.1: Experimental setup for low-repetition rate synthesis.

The target was a α - Al_2O_3 target synthesized by a Czochralski method. The crater depth is measured using Alpha-Step D100 profiler from Tencor. The crater depth measured after 5 pulses is $1.5 \mu\text{m} \pm 500 \text{ nm}$. The crater diameter is measured with an optical microscope. The crater diameter is $500 \mu\text{m} \pm 100 \mu\text{m}$.

After 20 min of synthesis in a 50 mL beaker, we performed the TEM measurement as described previously [See figure 2.2]. Pictures (a) and (b) correspond to a particle of 5.5 nm diameter, diffracting in the zone axis [001]: $d_{440} = 0.143 \text{ nm}$, $d_{040} = d_{400} = 0.202 \text{ nm}$. By comparing with interreticular distances and angles reported in the ICDD file 04-007-2479, the particles are identified as γ - Al_2O_3 .

This result is consistent with the theoretical work of McHale et al. [60].

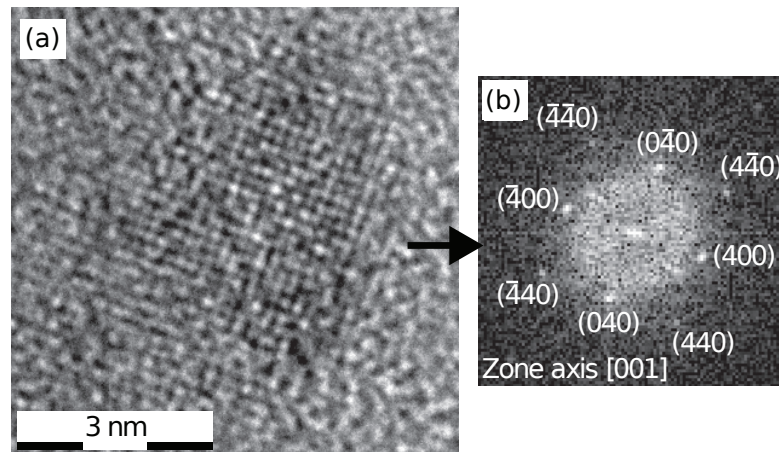


FIGURE 2.2: TEM images of γ - Al_2O_3 nanoparticles (a) and a corresponding FFT (b) obtained using our experimental setup.

2.2.2 α - Al_2O_3 obtained from picosecond infrared lasers

Later on, we performed PLAL synthesis at the Stephan Barcikowski's group in the University of Duisburg-Essen. The $\text{Al}_2\text{O}_3:\text{Cr}^{3+}$ target was elaborated by Kheirreddine Lebbou [68, 69]. The laser used was a diode pumped picosecond Nd:YAG laser ($\lambda = 1064, \text{ nm}$, $\tau = 10 \text{ ps}$, $f = 500 \text{ kHz}$). The average energy per pulse was $2 \times 10^{-5} \text{ J/pulse}$ after the ablation lens. Two synthesis were done (i) during 2 min in a 40 mL of deionized water, (ii) during 10 min in a 40 mL of deionized water containing $10^{-2} \text{ mol.L}^{-1}$ of 2-[2-(2-methoxyethoxy) ethoxy] acetic acid (MEEAA).

For the first synthesis (i), we performed the TEM measurement [See figure 2.3]. From the FFT, we measured the interreticular distances $d_{1\bar{1}2} = 0.348 \text{ nm}$, $d_{110} = 0.242 \text{ nm}$, $d_{2\bar{1}3} = d_{1\bar{2}3} = 0.210 \text{ nm}$, and $d_{2\bar{2}4} = 0.176 \text{ nm}$. The interreticular distances and the angles match those reported in the ICDD file 00-046-1212 for α - Al_2O_3 . γ - Al_2O_3 were also

observed scarcely. Concerning the size distribution, it is difficult to conclude because most particles were aggregated.

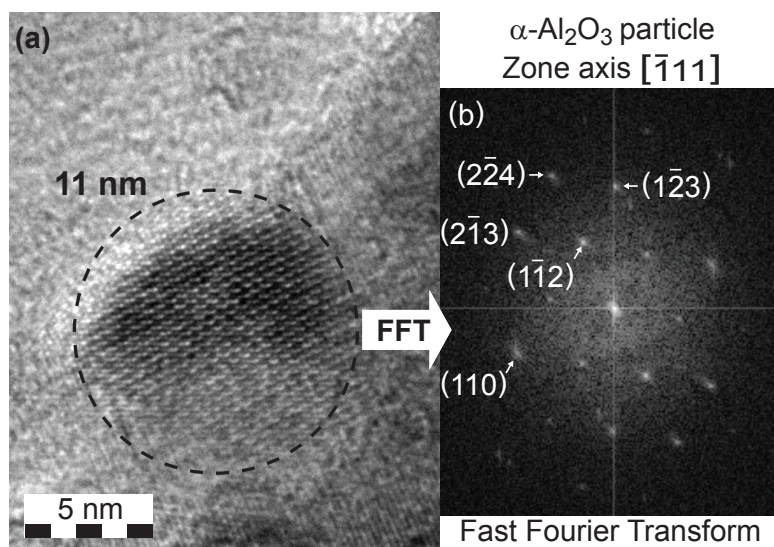


FIGURE 2.3: TEM images of α - Al_2O_3 nanoparticles (a) with a corresponding fast Fourier transform (b) using Barcikowski's experiment.

For the second synthesis (ii) where complexing agents were added, the particles are much smaller and do not seem to aggregate [See figure 2.4]. The size distribution was determined and the mean size is equal to 2.3 ± 0.97 nm. At the moment, no crystallographic characterizations could have been done because of the very small size of the nanoparticles.

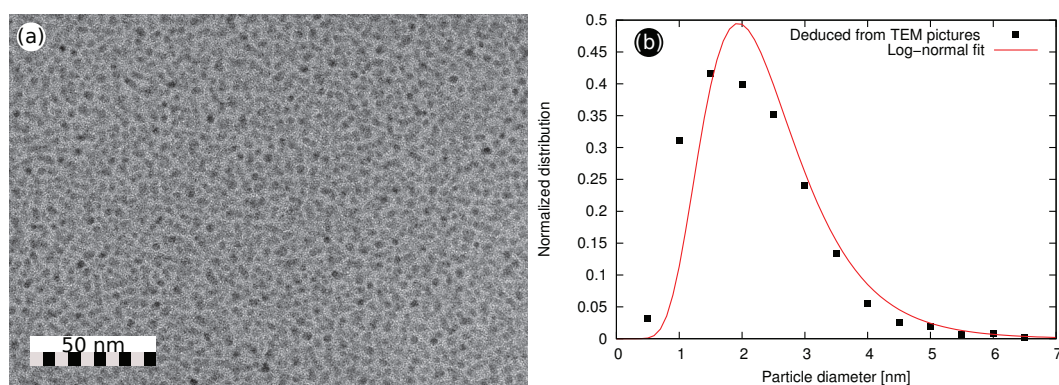


FIGURE 2.4: Results obtained for α - Al_2O_3 synthesized with complexing agents (a) Typical TEM pictures. (b) Corresponding size distribution centered around 2.3 ± 0.97 nm.

Moreover, luminescence emission spectroscopy was also used to check if the synthesized nanoparticles exhibit luminescence properties similar to those of bulk. The excitation was performed with a 455 nm diode. In figure 2.5, the chromium emission around 694 nm

can be observed. For nanomaterials, the luminescence is usually broader due to the arising of surface effects and structural inhomogeneities [20]. In our case, for both synthesized samples, the inhomogeneous broadening is indeed recognized thus confirming the presence of $\alpha\text{-Al}_2\text{O}_3\text{:Cr}^{3+}$ nanoparticles as expected following the TEM characterization.

The Laplace pressure for nanoparticles In addition, at these length scales, surface effects are usually taken into account via a supplementary term in the pressure following: $P_s = \frac{2\sigma}{R}$ [70] where σ is the surface tension and R is the nanoparticle radius. For instance, a shift in the transition pressure at nanoscale is attributed to this overpressure by Wang et al. [70]. Yet, in our synthesized nanoparticles, this additional pressure should induce a shift in the luminescence of a few nanometers. Since no shift of the luminescence peaks is observed, the enhancement of surface energies observed at nanoscale cannot be monitored by an overpressure and that so-called Laplace pressure.

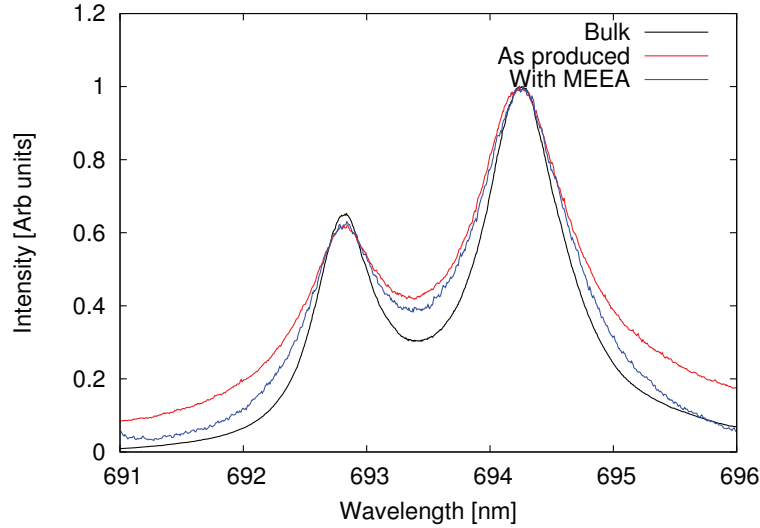


FIGURE 2.5: $\alpha\text{-Al}_2\text{O}_3\text{:Cr}^{3+}$ luminescence emission spectroscopy measurement for different samples.

Applications for pressure sensing The synthesized nanoparticles without complexing agents were characterized under pressure to assess their viability as pressure nanoprobes. High hydrostatic pressures were applied using a diamond anvil cell (DAC). PLAL nanoparticles were placed along with YAG:Sm microbeads in the chamber filled with 4:1 methanol/ethanol mixture as pressure transmitting fluid thus ensuring quasi-hydrostaticity up to 18 GPa. The YAG:Sm microbeads were previously calibrated in pressure and serves now as our pressure probe. Then, the shift of the $\alpha\text{-Al}_2\text{O}_3\text{:Cr}^{3+}$ luminescence emission was monitored as a function of the pressure for particles without complexing agents [See figure 2.6].

The black dots correspond to the peak position of the $\alpha\text{-Al}_2\text{O}_3:\text{Cr}^{3+}$ nanoparticles synthesized at Barcikowsky's experiment and the red line corresponds to the same measurement done with bulk $\alpha\text{-Al}_2\text{O}_3:\text{Cr}^{3+}$. The agreement between the bulk and nanoparticle behavior is promising for future applications as pressure sensor.

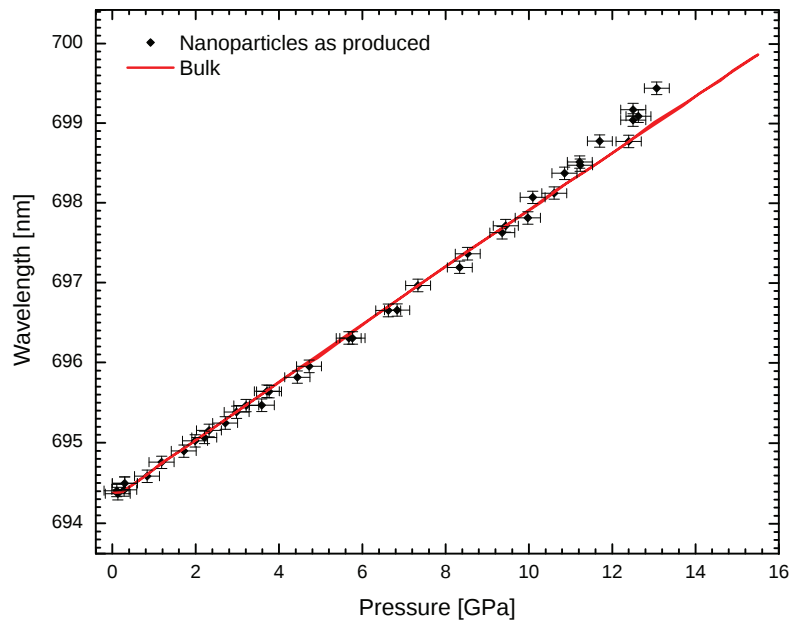


FIGURE 2.6: $\alpha\text{-Al}_2\text{O}_3:\text{Cr}^{3+}$ luminescence position as a function of the pressure calibrated using YAG:Sm microbeads.

2.3 Conclusion

In summary, the nanosecond UV laser generated $\gamma\text{-Al}_2\text{O}_3:\text{Cr}^{3+}$ nanoparticles. This result confirms the McHale's predictions that $\gamma\text{-Al}_2\text{O}_3$ is the most stable structure at nanoscale due to surface effects. Fortunately, we have been able to synthesize $\alpha\text{-Al}_2\text{O}_3:\text{Cr}^{3+}$ nanoparticles using a picosecond infra-red laser. Although, the as-produced materials suffer from aggregation, an addition of complexing agents allows one to sharpen the size distribution and increase the colloidal stability. A broadening in the luminescence peak was observed for both samples with and without complexing agents. This broadening is attributed to structural inhomogeneities at nanoscale. Yet, no shift was noticed thus proving that the Laplace pressure cannot be manipulated in the context of solid nanoparticles. By probing the shift of the luminescence as a function of the pressure, we also demonstrated promising applications of these nanomaterials to reach microfluidic applications.

However, this work also showed the multiplicity of the mechanisms underlying PLAL. Especially, in the case of aluminum oxide, the chemical interaction between aluminum and oxygen atoms ought to be considered while in noble metals it could have been neglected. Indeed, the aluminum and oxygen atoms should eventually grow into clusters, Al_xO_y which would thereafter lead to the final nanoparticles. But, these intermediate reactions are not identified. Especially, no quantitative work has been done to follow the chemical composition during the growth processes. Moreover, the temporal evolution of the thermodynamics parameters, i.e. temperature, density and pressure, have only been scarcely quantified. In the next chapters, we will devote our efforts to investigate how the ablated atoms can recombine to form clusters and nanoparticles and upon which thermodynamics conditions it happens.

Chapter 3

Underwater plasma spectroscopy, implementation and fundamental consequences

*"Blind belief in authority is the
greatest enemy of truth."*

Albert Einstein

Contents

3.1 Plasma spectroscopy to probe the first time scales	28
3.1.1 The plasma, a source of light	28
3.1.2 Thermodynamic characterization of the plasma	29
3.1.3 Experimental setup	30
3.2 Investigation on the underwater aluminum oxide plasma	31
3.2.1 Challenges of plasma spectroscopy underwater	31
3.2.2 Electron density	32
3.2.3 Rotational temperature	34
3.2.4 Temporal evolution of the chemical composition	36
3.3 Challenges for equilibration in molecular plasma	40
3.3.1 Electronic equilibration, the McWhirter criteria	41
3.3.2 Rotational equilibration	46
3.3.3 Perspectives on the role of chemical reactions	50
3.4 Conclusion	56

UNDERWATER, the ablated material is in a plasma state and is optically active from a few nanoseconds until a few microseconds. Optical emission spectroscopy (OES) may be employed to probe the main features of laser-induced plasmas (LIPs). This information is of particular interest for the understanding of the processes occurring in laser-assisted material fabrication but also for analytical chemistry purposes since chemical composition of targets can be characterized by examining the LIP. The technique is generally called laser-induced breakdown spectroscopy (LIBS) and can be applied in numerous fields such as biology [71], space exploration [72, 73] or forensic science [74].

Here, one profits from the rapidity and the remote sensing features of the method. Underwater, the liquid confines the plasma and changes drastically its properties. The first section will describe how the plasma properties can be probed using spectroscopy. Then, the results we obtained underwater will be discussed in more detail. In the last section, I will introduce our investigations about the equilibration of a molecular plasma.

3.1 Plasma spectroscopy to probe the first time scales

3.1.1 The plasma, a source of light

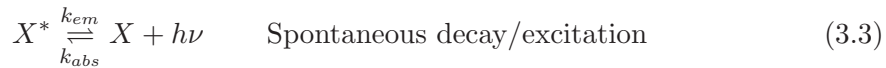
As a starting point, the plasma is composed of electrons, ions, atoms and molecules. Under ideal conditions, we will consider an equilibrated plasma and the Boltzmann equation to probe the population number density N_p^X of an element X at a quantum state p:

$$N_p^X = \frac{g_p N_{tot}^X}{Z_X} \exp\left(-\frac{E_p}{kT_e}\right) \quad (3.1)$$

where Z_X is the partition function of X, g_p and E_p are respectively the degree of degeneracy of p and the energy of p calculated from the ground state, T_e is the electronic temperature, k is the Boltzmann constant and N_{tot}^X is the total density population of the element X. Z_X is expressed in a microcanonical ensemble:

$$Z_X = \sum_p g_p \exp\left(-\frac{E_p}{kT_e}\right) \quad (3.2)$$

Absorption from the Bremsstrahlung inverse ensures electron gas excitation and temperature elevation at the very beginning of the plasma creation. Thereafter, de-excitation may result from spontaneous light emission:



where X^* is the excited state of X and k_{em} , k_{abs} are the respective reaction rates. The emitted light intensity corresponds to a transition between two electronic levels (eg. $p \rightarrow q$) and is given by:

$$I_{qp}^X = A_{pq} N_p^X \quad (3.4)$$

where A_{pq} is the transition probability also called Einstein coefficient of spontaneous emission. For most atoms and ions, the electronic energy diagrams are identified and listed in databases such as the "NIST Atomic Spectra Database Lines" or the "Atomic spectral line database from CD-ROM 23 of R. L. Kurucz" [75, 76]. Therefore, a spectral

analysis of the emitted light enables one to identify the plasma components. Furthermore, as stated in the equation 3.4, the emitted light is proportional to the density population of the excited states which is proportional to the total density population. As a consequence, targets of different chemical composition can be quantified using calibrated samples assuming reproducible experimental conditions and stability of the temperature [77]. OES is then used as an analytical tool to investigate the target chemical composition.

Moreover, the time evolution of the plasma composition can be obtained by comparing lines from each considered element as a function of time. Such a measurement informs about the chemical reactions occurring inside the plasma and increases the understanding of pulsed laser deposition techniques [78, 79].

3.1.2 Thermodynamic characterization of the plasma

Along with the chemical composition, thermodynamic properties of the system can be probed using plasma spectroscopy. For a more general description, please refer to the review written by Aragon et al. [80].

For the plasma temperature, the Boltzmann plot technique is generally used. Intensities of lines from a same element are measured for different excited state energies. Then, the exponential dependence on the energy enables one to determine T_e [See equation 3.1]. In practice, the line selection is critical since lines can suffer from self-absorption and overlapping. To increase the accuracy of the method, lines from energies spread among a wide range of values must be employed. Atoms and ions from different elements can also be used together to overcome this difficulty. The method is called the multi-element Saha-Boltzmann plot technique and only works when the electron density is also measured and the plasma temperature is uniform [81].

The electron density is usually obtained from the Stark effect stating that an electric field can modify energy levels of atoms and ions [82]. The plasma free electrons can be responsible for such an electronic field and induce a shift $\Delta\lambda$ and a broadening σ of the spectral lines. Assuming that the Stark effect is the dominant mechanism responsible for such a modification in comparison with Doppler and pressure effects, the relationship between the electron density N_e and the spectrum characteristics are usually considered linear for non Hydrogen-like atoms:

$$\Delta\lambda = d N_e \quad (3.5)$$

$$\sigma = 2\omega N_e \quad (3.6)$$

where d is the electron impact shift and ω is electron impact width. These parameters are listed for typical plasma temperatures in the book written by Griem [83].

The thermodynamic properties would enable one to design a theoretical model of the plasma evolution. In calibration-free techniques, for example, the target composition is measured from the relative intensities between several lines but the method requires the determination of plasma temperature [84, 85].

3.1.3 Experimental setup

For the ablation part, we used the experimental setup described previously in section 2.2.1. The plasma emission was collected through a $2f/2f$ light collection set-up ($f = 75$ mm) and imaged on the entrance of a circular to rectangular fibers bundle (LOT Oriol) with a N.A. of 0.22. The observed length was equal to the whole optical fiber diameter which is $800 \mu\text{m}$. A monochromator was then coupled to an intensified CCD (Andor Technology) to characterize spectrally the emitted light. The laser and the iCCD were both controlled by a pulse generator (Stanford Research Systems). The use of an iCCD coupled with a pulse generator allows one to reach a temporal resolution of few nanoseconds. However, the time integration needed to obtain proper spectra is often more than hundreds of nanoseconds. Two different monochromators were used. The first one was a Ramanor U1000, from Jobin Yvon, with a 1 m focal and a 1800 lines/mm grating with which, we collected the light in windows 7 nm wide. The spectra could be measured from 325 nm to 870 nm. The second monochromator is a Shamrock 303, from Andor Technology, with two different gratings (1200 lines/mm and 300 lines/mm). For every measurement, the spectral resolution and calibration are obtained from calibration lamps. The spectral response is also corrected using blackbody sources. Figure 3.1 summarizes the main features of the experimental setup.

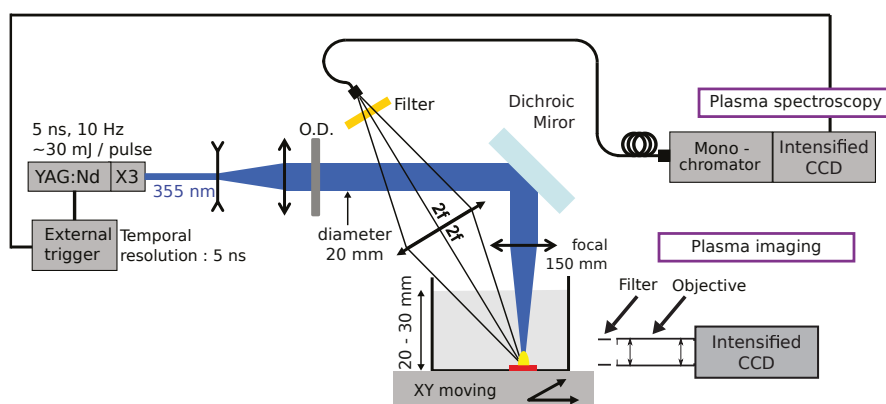


FIGURE 3.1: Experimental setup for the plasma spectroscopy and plasma imaging underwater.

For the plasma imaging, we used the same intensified CCD. The plasma light was collected through a refractive telescope composed of two lenses, with a four times magnification. Narrow band filters were placed in front of the optical system to spectrally select the emitted light. The filters used were centred at 390 ± 5 nm and 488 ± 5 nm for the aluminum lines and the aluminum oxide lines, respectively. Each image is the accumulation of 50 acquisitions.

3.2 Investigation on the underwater aluminum oxide plasma

In the previous section, we described the use of plasma spectroscopy in ambient atmosphere. We showed how the technique can be used to measure the target composition, the temperature and the electron density in the plasma. In this section, we will show how this technique can also be used to characterize the underwater plasma. We will begin with a review of the difficulties raised by working underwater. These lead to the necessity of considering molecules and atoms instead of ions and atoms. Then, we will show the results we obtained from the underwater plasma spectroscopy of an aluminum oxide target. Especially, we probed the electron density, the molecular temperature and the chemical composition of the plasma.

3.2.1 Challenges of plasma spectroscopy underwater

In the case of plasma spectroscopy underwater, the time scale and the thermodynamic conditions are very different from those in air. Therefore, a completely different approach is required. The work published by Kumar et al. describes most of the differences [86–88]. In general, the surrounding liquid enables a stronger confinement of the plasma. This property has three main consequences. Firstly, the plasma is smaller [See figure 3.2]. From plasma imaging, the plasma diameter is usually three times smaller than in air.

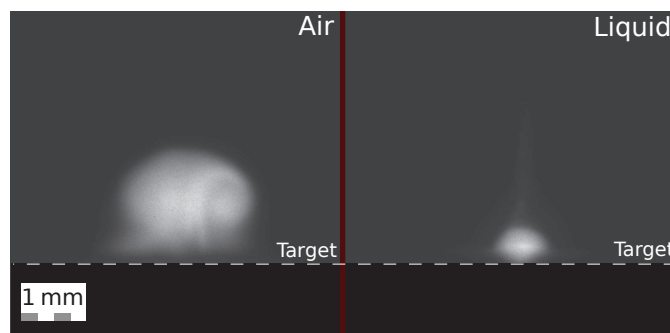


FIGURE 3.2: Plasma imaging after the laser ablation of an alumina crystal measured at $2 \mu\text{s}$ in air and water.

Figure 3.3 shows the aluminum atom spectra in air and in liquid using the same experimental conditions. In water, recorded spectra exhibit a lower signal to noise ratio. Secondly, in air, the plasma lasts longer. We showed previously that up to hundreds of microseconds, the plasma can still be characterized [89]. In liquid, to our knowledge, no plasma emission has been measured after a few microseconds because of the rapid quenching of the electron gas. Thirdly, liquids have better thermal dissipation capacities than air and vacuum. Thus, the temperature of the plasma is cooler in the liquid. As a consequence, ions and lines from highest excited energy levels such as those from hydrogen or oxygen and from low concentration species eg. dopant and small residues cannot be observed. To overcome this difficulty, diatomic molecules must be studied since they emerge more easily due to lower temperature.

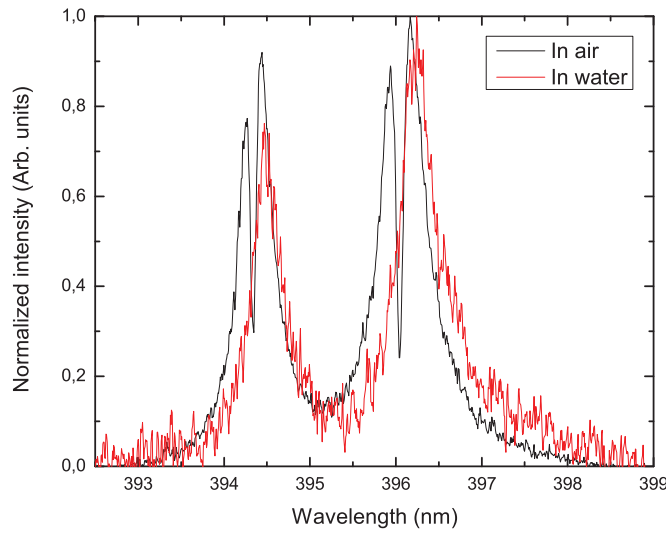


FIGURE 3.3: Plasma spectroscopy after the laser ablation of an alumina crystal measured at 500 ns in air and water.

3.2.2 Electron density

Historically, the H- α line located at 656.279 nm is usually employed to reach the electron density especially in shock-heated plasmas [90]. This line is considered as optically thin which means that it does not suffer from self-absorption process. For laser-induced plasma, Sherbini already proved the reliability of the method [91]. However, the electronic energy of the excited state is equal to 12.1 eV. The hydrogen electron can barely reach such a high value of energy underwater. As a consequence, it cannot be used for electron density determination. We chose to work with the aluminum lines located at 394.4 nm and at 396.2 nm and respectively coming from the (${}^2P_{1/2}^0 - {}^2S_{1/2}$) and the (${}^2P_{3/2}^0 - {}^2S_{1/2}$) transitions. In figure 3.4, these lines are plotted for different time delays. A shift towards lower wavelengths and a sharpening of the lines are observed when

increasing the time delay. This behaviour is a signature of the Stark effect since the electron density drops through electron recombinations. Moreover, these spectra do not exhibit any self-reversal in water unlike in air [See figure 3.3].

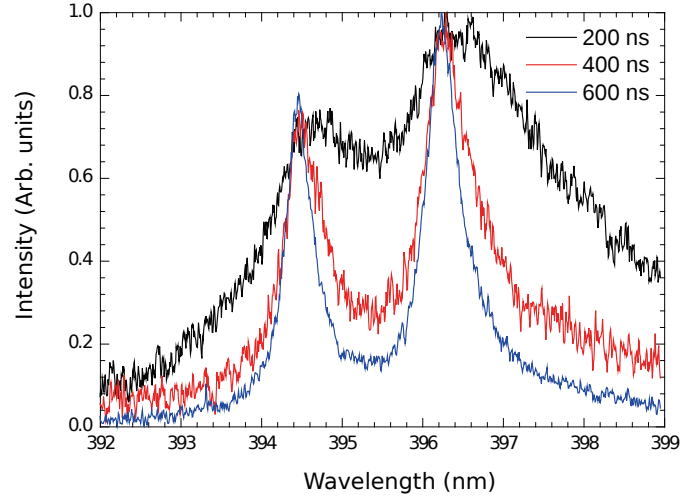


FIGURE 3.4: Typical spectrum of aluminum atoms recorded at different time delays at high resolution (FWHM=0.053 nm) for an Al_2O_3 target underwater. The emission comes from the electronic transitions (${}^2\text{P}_{1/2}^0$ - ${}^2\text{S}_{1/2}$, 394.4 nm) and the (${}^2\text{P}_{3/2}^0$ - ${}^2\text{S}_{1/2}$, 396.2 nm).

The positions and the widths are extracted from a Voigt fit. Equations 3.6 are used to obtain the electron density using $d = 1.64 \times 10^{-19} \text{ nm cm}^{-3}$ and $\omega = 1.37 \times 10^{-19} \text{ nm cm}^{-3}$ [83]. We obtain the figure 3.4. The errors bars are deduced from uncertainties in the fit and mostly from the constant parameters.

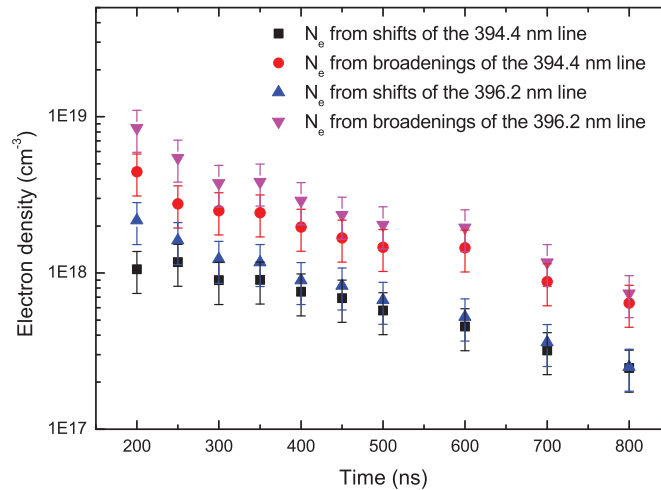


FIGURE 3.5: Temporal evolution of the electron density for an Al_2O_3 target underwater measured via Stark shifts and broadenings of the aluminum lines.

There are differences in the results when changing the method. First, the broadenings of the 394.4 nm and the 396.2 nm lines exhibit different values. This can be attributed

to self-absorption effects which usually broaden lines. For the longest delays, the two values converge due to the drop in density and a fortiori the drop in self-absorption. Moreover, self-absorption effects are proportional to the quantity of emitted light. The 396.2 nm emission must be twice as high as the 394.4 nm emission due to spin degeneracy considerations. This can explain why the electron density measured via the 396.2 nm line is higher than the other. For these reasons, we value more the results obtained with the Stark shift. Extrapolation of the shift of the ${}^2P_{1/2}^0 - {}^2S_{1/2}$ emission leads to a drop below 10^{16} cm^{-3} after $1.6 \mu\text{s}$. As a comparison, in air, we measured electron densities one order of magnitude smaller [See figure 3.11]. This difference is explained by the plasma confinement observed in liquid.

3.2.3 Rotational temperature

As mentioned previously, a singularity of plasma spectroscopy underwater is that ions and traces cannot be observed. As a consequence, for an alumina target, one can only rely on the aluminum monoxide lines to reach the plasma temperature.

In diatomic molecules, considering electronic, vibrational and rotational quantum states defined by the quantum numbers (n, v, J) [See figure 3.6], the energy of an observed transition is given by $\Delta E = E(n', v', J') - E(n, v, J)$ with:

$$E(n, v, J) = E_n + E_{vib}(n, v) + E_{rot}(n, v, J). \quad (3.7)$$

The vibrational contribution can be expressed as an anharmonic oscillator:

$$E_{vib}(n, v) = \omega_n (v + 1/2) - \omega_n x_n (v + 1/2)^2 + \omega_n y_n (v + 1/2)^3 \quad (3.8)$$

where $\omega_n(v)$, $\omega_n(v)x_n$, $\omega_n(v)y_n$ are the vibrational constants at a given vibrational level v and electronic level n . For AlO, the constant values are listed by Saksena et al. [92]. The rotational energy is given by:

$$E_{rot}(n, J) = B_n J(J + 1) - D_n J^2(J + 1)^2 \quad (3.9)$$

where $B_n(v)$ and $D_n(v)$ are the rotational constant at a given vibrational level v and electronic level n . For AlO, the constant values are also listed by Saksena et al. [92].

In addition, the measured intensity is proportional to $A_{v',v} S_{J',J}$ where $A_{v',v}$ is the Einstein coefficient and $S_{J',J}$ is the Hönl-London coefficient which takes into account kinetic momentum degeneracies of the rotational levels. For AlO, the constant values are listed respectively by Hebert et al. [93] and by Kovacs [94]. The measured intensity is also proportional to the population of the excited state $N(n', v', J')$. The latter depends on

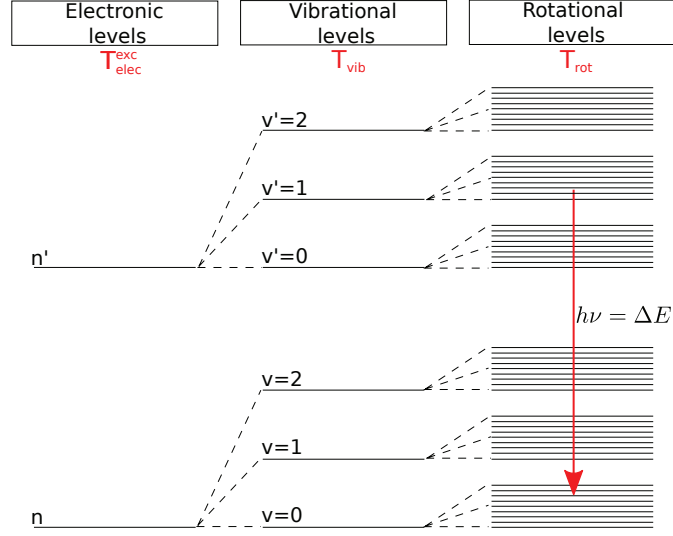


FIGURE 3.6: Diagram for the molecular energy levels.

three different temperatures, T_e , T_{vib} , and T_{rot} through the partition functions. Assuming a complete decoupling between electronic, vibrational and rotational motions, one can write:

$$N(n', v', J') = \frac{z_{elec}(n', T_e) z_{vib}(n', v', T_{vib}) z_{rot}(n', v', J', T_{rot})}{Z_X} \times N_{tot}^X \quad (3.10)$$

where k is the Boltzmann constant, N_{tot}^X corresponds to population summed over all the energy levels and Z_X is the total partition function which here, is not necessarily expressed because we compare lines of the same molecule. The individual partition functions are given by:

$$z_{elec}(n', T_e) = g_e \exp\left(-\frac{E_{n'}}{kT_e}\right) \quad (3.11)$$

$$z_{vib}(n', v', T_{vib}) = \exp\left(-\frac{E_{vib}(n', v')}{kT_{vib}}\right) \quad (3.12)$$

$$z_{rot}(n', J', T_{rot}) = g_{J'} \exp\left(-\frac{E_{rot}(n', v', J')}{kT_{rot}}\right) \quad (3.13)$$

Finally, the peaks are convolved with Gaussian profiles to take into account the experimental broadening (FWHM=0.061 nm). We developed a simulation program which can reproduce spectra as a function of the temperature and derive the best fitting temperature.

A typical spectrum is shown in figure 3.7. For the rotational temperature calculations, the AIO spectra were measured around 487 nm, which corresponds to the $\Delta v = 0$ vibrational sequence. The temperature value was obtained using a chi-square minimization

algorithm. The $(v', v) = (0, 0)$ bands [484.26–486.60 nm] were chosen because the intensity distribution does not depend on the vibrational temperature. Before any chi-square calculation, the experimental and the tested curve were normalized at 484.56 nm to avoid self-absorption effects in the band heads $(v', v) = (0, 0)$ and $(v', v) = (1, 1)$ located at 484.26 nm and 486.67 nm, respectively. We assumed an error of 500 K due to the experimental reproducibility and the fitting uncertainties. The temperature does not seem to vary from 2.0 μs to 2.5 μs . These values are consistent with measurements from C_2 molecules under similar conditions [95].

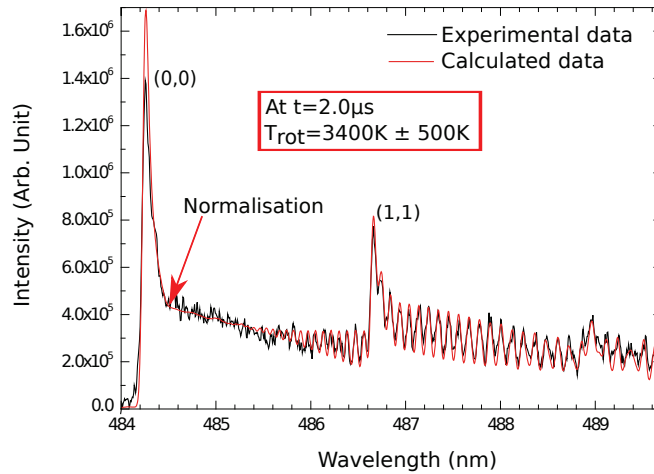


FIGURE 3.7: Typical spectrum of aluminum monoxide recorded at 2 μs with a gate width of 100 ns at high resolution (FWHM=0.061 nm) for an Al_2O_3 target underwater. The emission comes from the rovibrational transition between the $\text{B}^2\Sigma^+$ and the $\text{X}^2\Sigma^+$ states.

3.2.4 Temporal evolution of the chemical composition

From plasma spectroscopy, one can also probe the chemical reactions comparing measured intensities [See figure 3.8]. In our case, we wanted to investigate the oxidation of aluminum atoms. Therefore, we measured simultaneously the emission from aluminum atoms and aluminum monoxide molecules. The first one comes from the $(^2\text{P}_{1/2}^0 - ^2\text{S}_{1/2})$ and the $(^2\text{P}_{3/2}^0 - ^2\text{S}_{1/2})$ transitions respectively located at 394.4 nm and at 396.2 nm. For aluminum monoxide molecules, we probed the rovibrational transitions between the $\text{B}^2\Sigma^+$ and the $\text{X}^2\Sigma^+$ states.

The figure 3.9 was obtained by calculating the ratio between the two emission intensities. The increase of the ratio agrees with the oxidation of aluminum atoms, which turn into aluminum monoxide through chemical reactions.

Although a ratio in intensity was measured, the most appropriate quantity is the ratio in density. To go from one to another, the proportional coefficient $f(T)$ must be calculated

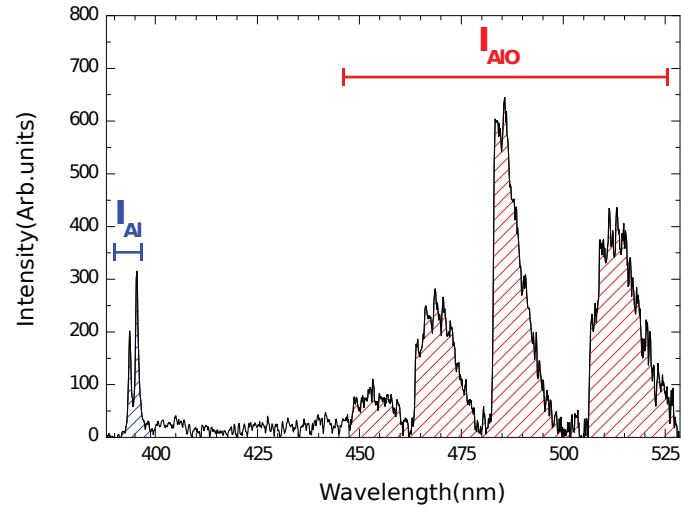


FIGURE 3.8: Typical spectrum recorded at 800 ns at low resolution (FWHM=0.72 nm) for an Al_2O_3 target underwater.

considering that:

$$\frac{N_{tot}^{AlO}}{N_{tot}^{Al}} = f(T) \frac{I_{AlO}}{I_{Al}} \quad (3.14)$$

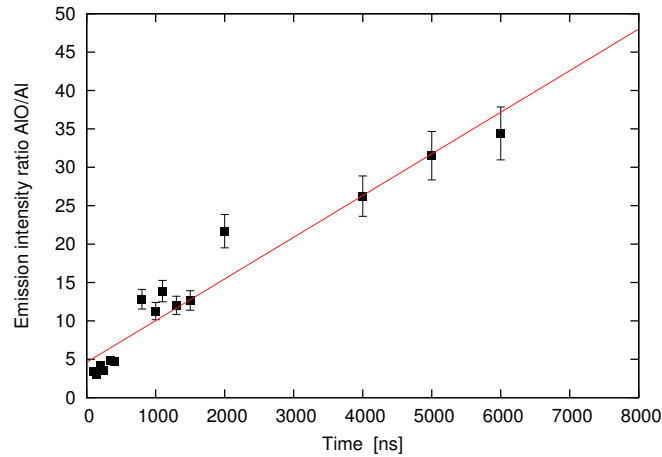


FIGURE 3.9: Temporal evolution of the intensity ratio between aluminum and aluminum monoxide lines.

The case of aluminum (${}^2\text{P}_{1/2}^0$ - ${}^2\text{S}_{1/2}$) and (${}^2\text{P}_{3/2}^0$ - ${}^2\text{S}_{1/2}$) transitions The two first electronic states of aluminum are located at $E_{1a} = 0$ eV and $E_{1b} = 0.014$ eV while the next ones are located at $E_2 = 3.1$ eV [See table 3.1]. This large difference in energy allows one to approximate the aluminum partition function Z_{Al} when the temperature is much

lower than 3.1 eV ($\simeq 3.6 \times 10^4$ K). Following the equation 3.2, one obtains:

$$Z_{Al} = \sum_p g_p \exp\left(-\frac{E_p}{kT}\right) \simeq g_{1a} + g_{1b} = 6 \quad (3.15)$$

where the corresponding constants are summarized in table 3.1. Finally, the measured intensity corresponding to the sum of both (${}^2P_{1/2}^0$ - ${}^2S_{1/2}$) and (${}^2P_{3/2}^0$ - ${}^2S_{1/2}$) transitions is given by:

$$I_{Al} \propto N_{tot}^{Al} \left(A_{2,1a}^{Al} + A_{2,1b}^{Al} \right) \frac{g_2}{g_{1a} + g_{1b}} \exp\left(-\frac{E_2}{kT}\right) \quad (3.16)$$

Generic name	Term	E_i (eV)	g_i
1a	${}^2P_{1/2}^0$	0.000	2
1b	${}^2P_{3/2}^0$	0.014	4
2	${}^2S_{1/2}$	3.143	2

TABLE 3.1: Atomic aluminium energy levels data where the generic name stands for the index used in this manuscript [76].

The case of aluminum monoxide $B^2\Sigma^+-X^2\Sigma^+$ rovibrational transitions We need to evaluate the aluminum monoxide total partition function. For AlO, electronic levels are named following the notations of table 3.2. Only the two first electronic energy levels can contribute to the partition function since $E_3 = 2.565$ eV is much bigger than kT_e :

$$Z_{AlO} = \sum_p g_p Z(p) \quad (3.17)$$

$$\simeq Z(1) + Z(2) \quad (3.18)$$

$$= z_{vib}(1)z_{rot}(1) \exp\left(-\frac{E_1}{kT_e}\right) + z_{vib}(2)z_{rot}(2) \exp\left(-\frac{E_2}{kT_e}\right) \quad (3.19)$$

As measured by Sakka et al. [96], we will assume $T_{vib} = 6000$ K. The vibrational anharmonicity can then be neglected and using the equation 3.12, we have:

$$z_{vib}(n, T_{vib}) = \sum_v z_{vib}(n, v, T_{vib}) \quad (3.20)$$

$$= \sum_v \exp\left(-\frac{\omega_e(v+1/2)}{kT_{vib}}\right) \quad (3.21)$$

$$\simeq \frac{1}{2 \sinh\left(\frac{\omega_e}{kT_{vib}}\right)} \quad (3.22)$$

For the rotational partition function, we use the equation 3.13 and assumed that the rotation is a rigid rotator:

$$z_{rot}(n, T_{rot}) = \sum_J z_{rot}(n, J, T_{rot}) \quad (3.23)$$

$$= \sum_J (2J + 1) \exp\left(-\frac{B_n J(J + 1)}{kT_{rot}}\right) \quad (3.24)$$

In the case of laser induced plasma, one can consider that $kT_{rot} \gg B_n J(J + 1)$ and substitute the sum for an integral:

$$z_{rot}(n, T_{rot}) \simeq \frac{kT_{rot}}{B_n} \quad (3.25)$$

Then, the measured intensity is related to the total density through:

$$I_{AlO} = N_{tot}^{AlO} \frac{2}{Z_{AlO}} \sum_{v',v,J',J} A_{v',v} S_{J',J} z_{vib}(3, v') z_{rot}(3, J') g_3 \exp\left(-\frac{E_3}{kT_e}\right) dV \quad (3.26)$$

The sum accounts for the integration over the whole AlO spectrum and can be reduced since for any value of v' , $A_{v',v}$ could be approximated using $\langle A \rangle \equiv \sum_v A_{v',v} \simeq 8.61 \times 10^6 \text{ s}^{-1}$ and $\sum_J S_{J',J} = 1$ for any value of J' . Using the same approximation as for the individual partition functions, one obtains:

$$\sum_{v'} z_{vib}(3, v') \simeq \frac{1}{2 \sinh\left(\frac{\omega_3}{kT_{vib}}\right)} \quad \text{and} \quad \sum_{J'} z_{rot}(3, J') = \frac{kT_{rot}}{B_3} \quad (3.27)$$

Finally, the measured intensity is given by:

$$I_{AlO} \propto A \times N_{tot}^{AlO} \times \frac{2}{Z_{AlO}} \times \frac{1}{2 \sinh\left(\frac{\omega_3}{kT_{vib}}\right)} \times \frac{kT_{rot}}{B_3} \times \exp\left(-\frac{E_3}{kT_e}\right) \quad (3.28)$$

Generic name	Term	E_i (eV)	ω_i (cm ⁻¹)	B_i (cm ⁻¹)
1	X ² Σ ⁺	0.000	979.524	0.64165
2	A ² Π _i	0.670	729.762	0.53717
3	B ² Σ ⁺	2.565	870.369	0.60897

TABLE 3.2: Molecular aluminum monoxide energy levels data where the generic name stands for the index used in this manuscript [76].

Calculation of the f factor From the equations 3.16 and 3.28, we can calculate the f factor which follows the equation 3.14:

$$f = \frac{(A_{2,1a}^{Al} + A_{2,1b}^{Al})}{A} \times \frac{g_2}{2} \frac{Z_{AlO}}{Z_{Al}} \times 2 \sinh\left(\frac{\omega_3}{kT_{vib}}\right) \times \frac{B_3}{kT_{rot}} \times \exp\left(-\frac{E_2^{Al} - E_3^{AlO}}{kT_e}\right) \quad (3.29)$$

Let us acknowledge that f does not depend on the rotational temperature since Z_{AlO} also exhibits a linear dependence on T_{rot} . Therefore, the term $\frac{1}{T_{rot}}$ compensates with Z_{AlO} .

In figure 3.10, the value of f is plotted as a function of the electronic temperature and the vibrational temperature. Two main features are observed: **(i)** From 2000 K to 10000 K, the vibrational temperature does not effectively affect the value of f , the electronic temperature is more likely to modify the value of f . **(ii)** During the measurement time scale i.e. 100 ns - 6 μ s, the electronic temperature must decrease but in any cases, with typical values of temperature i.e. T_{elec} from 4000 K to 8000 K, the value of f goes from 0.897147 to 0.298032. Therefore, considering the equation 3.14, the figure 3.9 is an underestimation of the ratio in density $\frac{N_{AlO}}{N_{Al}}$. Using plasma spectroscopy, we probed chemical reactions by observing a strong oxidation of aluminum atoms to aluminum monoxide molecules.

3.3 Challenges for equilibration in molecular plasma

The previous section was dedicated to our results on plasma spectroscopy underwater. One of the interesting features of this work concerns the use of molecules. Indeed, while in ambient atmosphere, one can rely on ions and atoms to probe the thermodynamic conditions, in our case, ions are not detected and we must manipulate atoms and molecules. This peculiarity raises the question of equilibrium in the context of molecules. In our system, two natures of temperature can be distinguished. First, electrons are distributed on the electronic energy levels. Their population number density is probed by a temperature which can be named the *excitation temperature*. In atoms and ions, there is only one excitation temperature corresponding to the distribution along the electronic levels which will be called T_{elec}^{exc} . In molecules, the existence of two additional degrees of freedom, vibration and rotation, leads to the need of two other temperatures, T_{vib} and T_{rot} . In the meantime, these elements can move and induce a kinetic energy that is associated to a temperature. For each species one can identify one *kinetic temperature* i.e. T_{elec}^{kin} , T_{atom}^{kin} , T_{ion}^{kin} and T_{mol}^{kin} . Equilibrium in the sense of the plasma temperature designates the possibility to equalize these different temperatures. In this section, we will briefly describe the electronic equilibrium as it is usually considered in LIBS measurements.

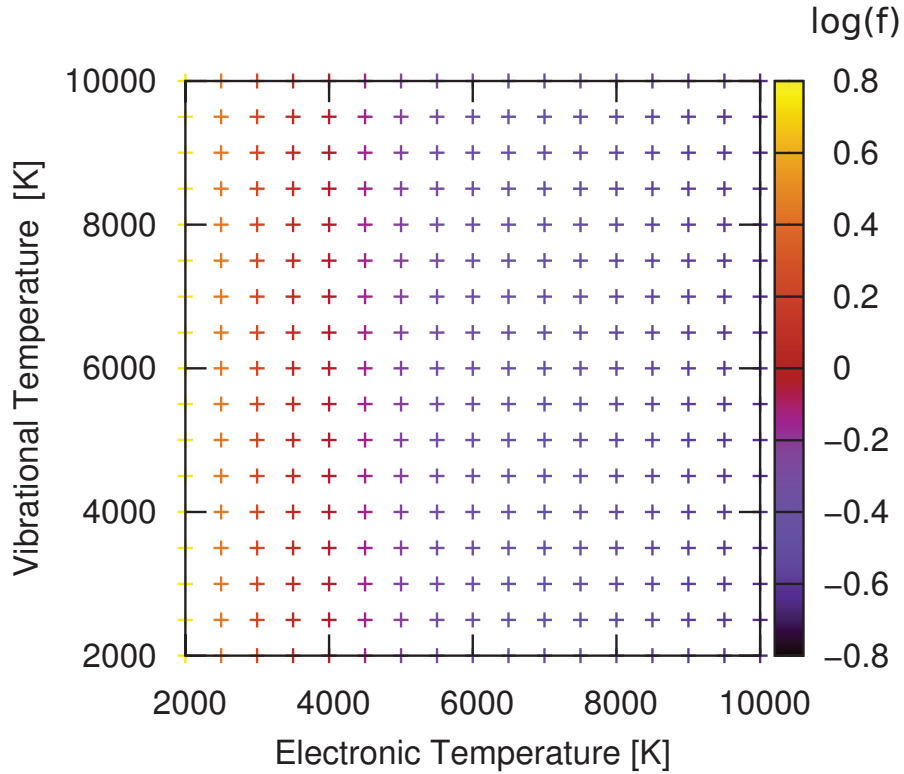


FIGURE 3.10: Proportionality factor between the ratio in intensity and the ratio in density, f , as a function of the electronic temperature and the vibrational temperature from 2000 K to 10000 K.

Then we will investigate two peculiar equilibration problems that are raised in molecular systems: **(i)** the equilibrium between electronic temperatures and the rotational temperatures, **(ii)** the equilibrium deviation due to chemical reactions.

Excitation temperature	Kinetic temperature
T_{elec}^{exc}	T_{elec}^{kin}
T_{vib}	T_{ions}^{kin}
T_{rot}	T_{atoms}^{kin}
	T_{mol}^{kin}

TABLE 3.3: Table recapitulating the different temperatures in a molecular plasma.

3.3.1 Electronic equilibration, the McWhirter criteria

In usual plasma spectroscopy techniques, the work is achieved in ambient pressure or vacuum and the studies focus on the short time scales ($< 10 \mu s$) where only atomic and ionic emissions are observed. As a consequence, most of the work on plasma equilibration has been done to address the equilibration between the electronic excitation

temperatures i.e. $T_{elec}^{exc}(ions) = T_{elec}^{exc}(atoms)$. To obtain such an equality, the plasma must be so dense in electrons that there are enough collisions between electrons and ions/atoms to overcome energy transfers from light emission, $k_+ + k_- \gg k_{em}$. As a consequence, the excitation temperatures correspond to the kinetic temperature of the electrons, T_{elec}^{kin} :

$$T_{elec}^{exc}(ions) = T_{elec}^{exc}(atoms) = T_{elec}^{kin} \equiv T_e \quad (3.30)$$

When this equality is verified, the system can be considered in a *Local Thermodynamic Equilibrium* (LTE) and T_{elec}^{exc} is abbreviated as T_e . Numerically, the first condition to assess the LTE is the McWhirter criterion:

$$N_e \geq 1.6 \times 10^{12} T_e^{1/2} (\Delta E)^3 \quad (3.31)$$

where T_e is the excitation temperature of the electronic levels (Kelvin) and ΔE (eV) is the largest energy gap in the system. In addition, conditions on temporal and spatial variation ought to be considered. In other words, the plasma evolution must not be too rapid or too inhomogeneous which is checked by comparing the temporal and spatial evolution to the time required to establish the equilibrium, τ_C , and the diffusion length, x_C , respectively :

$$\frac{T(t + \tau_C) - T(t)}{T(t)} \ll 1 \quad (3.32)$$

$$\frac{T(x + x_C) - T(x)}{T(x)} \ll 1 \quad (3.33)$$

The reader can find a more detailed description in numerous papers [97–101].

The following paragraph will detail a short study of electronic equilibration in air where we will actually apply the McWhirter criterion.

The example of Al_2O_3 : Ti/Fe in air

We worked on the ablation of an aluminum oxide Al_2O_3 target doped with titanium (Ti) and iron (Fe) under **ambient air**. To examine the McWhirter criterion, the electron density was deduced from the H- α line. The electronic excitation temperatures of the atoms and ions were obtained using the Fe I lines (~ 375 nm) and the Ti II lines (~ 350 nm) respectively.

The hydrogen residues composing the ambient atmosphere were used to measure the electron density. The H- α line around 656.6 nm was collected from 0.10 μs to 3.0 μs (See inset figure 3.11). For extended times, it was no longer resolved because the hydrogen electronic levels were not excited any more since the temperature could have been too

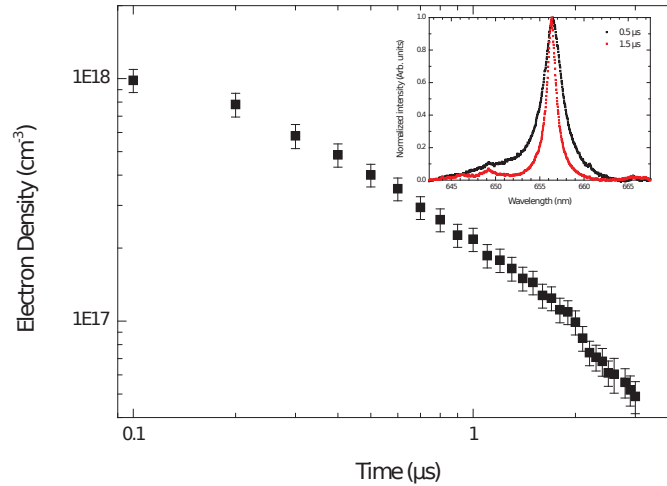


FIGURE 3.11: Temporal evolution of the electron density in log/log scale measured in ambient air. The inset graph is the time evolution of the H-alpha line measured with 0.19 nm resolution. The red curve is the measured curve at 1.5 μs with a typical Voigt profile.

low. When the H- α line was measured, the Stark effect was observed. The electron density (N_e) was deduced from the measured full width at half maximum (FWHM). We used the expression reported by Gigosos et al. [102]. We took into account the temperature through the weak dependence of the reduced Stark profiles for the Balmer series reported in the Table AIII.a of Griem's book [83]. We subtracted the background using the continuum emission and each spectrum was fitted by a Voigt profile with the Gaussian width taken as the experimental width. The self-absorption effect was neglected. The error bars were calculated considering fit errors and uncertainties in the numerical constants used. In figure 3.11, we observe a decrease of the electron density from $1 \times 10^{18} \text{ cm}^{-3}$ to $5 \times 10^{16} \text{ cm}^{-3}$ during the first 3 μs .

The electronic excitation temperature of the ions was measured through the Ti II lines around 350 nm with a resolution equal to 0.032 nm. Figure 3.12(a) shows typical spectra measured from 347 nm to 354 nm at different detection delays after the laser pulse. Five lines were selected in order to avoid any self-absorption effect or any overlapping with undesired lines. The electronic energy levels go from 3.69 eV to 5.57 eV. In figure 3.13(a), we show two typical Boltzmann plots and the corresponding temperatures obtained at 5 μs and 10 μs .

For the atomic excitation temperature, the Fe I spectra were measured around 375 nm with a resolution equal to 0.032 nm. Figure 3.12(b) shows typical spectra measured from 370.5 nm to 377 nm at different detection delays after the laser pulse. We chose eight lines which showed no overlapping with others nor exhibited a self-absorption effect. In this case, the excited electronic level energies range is from 3.33 eV to 4.30 eV. Two

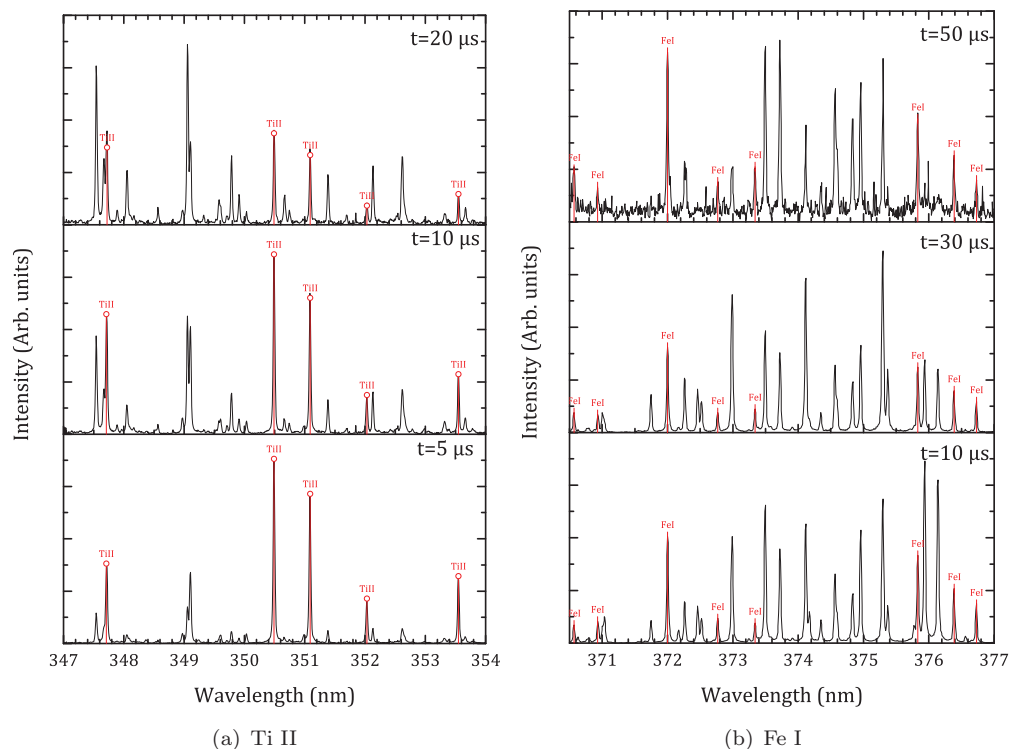


FIGURE 3.12: Typical normalized spectra measured at different time delays with a 0.032 nm resolution measured in ambient air. The red markers represent the lines used for the temperature calculation.

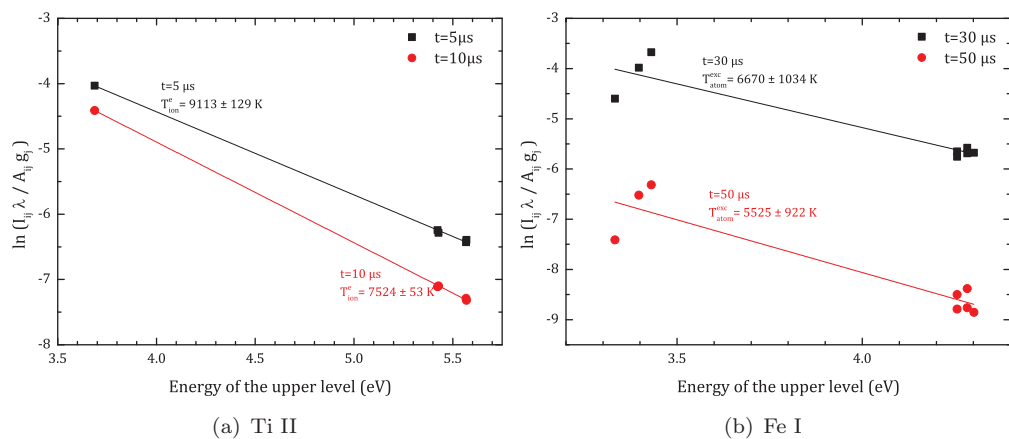


FIGURE 3.13: Typical Boltzmann plots using the lines referenced in Table 3.4 for different time delays.

typical Boltzmann plots are shown in figure 3.13(b) where the obtained temperatures are equal to 6670 ± 1034 K at $30 \mu\text{s}$ and 5525 ± 922 K at $50 \mu\text{s}$.

For both measurements, the Boltzmann plots do not exhibit an absolute linear behavior thus leading to a very high value of the measured incertitude.

We finally obtained the temporal evolution of the different temperatures from $0.1 \mu\text{s}$ to

Element	λ (nm)	A_{ki} ($10^{-6} \cdot s^{-1}$)	E_{up} (eV)	g_{up}
Ti II	347.718	7.59	3.69	8
Ti II	350.489	135	5.43	10
Ti II	351.084	133	5.42	8
Ti II	352.025	93.1	5.57	4
Ti II	353.540	96.1	5.57	6
Fe I	370.557	3.21	3.40	7
Fe I	370.925	15.6	4.26	7
Fe I	371.993	16.2	3.33	11
Fe I	372.762	22.4	4.28	5
Fe I	373.332	6.48	3.43	3
Fe I	375.823	63.4	4.26	7
Fe I	376.379	54.4	4.28	5
Fe I	376.719	63.9	4.30	3

TABLE 3.4: Spectroscopic data of the lines used for temperature calculation extracted from NIST [76].

40 μs [See figure 3.16]. For each parameter, the calculation was stopped when one of the considered peaks was no longer resolved. The excitation temperatures of the TiII ions and the FeI atoms decrease and meet after approximately 10 μs . This result is a signature of LTE and is confirmed by the measure of N_e . Indeed, considering our excitation temperatures, the critical value of N_e given by the McWhirter criterion is equal to $1.5 \times 10^{14} \text{ cm}^{-3}$ while in our measurement, N_e reaches a much higher value $5 \times 10^{16} \text{ cm}^{-3}$ after 2 μs [See figure 3.11].

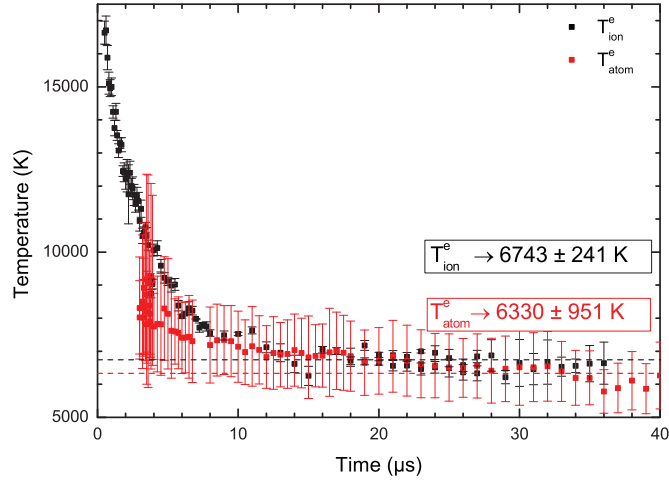


FIGURE 3.14: Temporal evolution of the excitation temperatures of the atoms (Fe I) and the ions (Ti II) measured in ambient air. The dotted lines stand for the mean values calculated from 10 μs .

3.3.2 Rotational equilibration

In order to address molecular plasma, the electronic excitation temperatures were compared with the rotational excitation temperature. We extended our work done in air and described in the 3.3.1 section. The AlO rovibrational spectra (~ 487 nm) were measured and the rotational temperature was derived using the method described previously. Based on these results, we present the complete time evolution of these different temperatures over a long time scale [0.1 – 90 μ s] and discuss the issue of their convergence.

In figure 3.15, we plot three typical curves measured at three different detection delays with a resolution equal to 0.032 nm and the corresponding simulated curve. The temperature derivation follows the method described previously [See section 3.2.3]. Although the electronic excitation temperatures match, the rotational temperature exhibits a different asymptotic value, $T_{rot} \rightarrow 3515 \pm 470$ K [See figure 3.16].

In the following paragraphs, we will try to clarify this peculiar phenomenon. First, we will describe the spatial distribution and show that AlO and Al are located at the same position when the rotational temperature is measured. Then, following considerations on orders of magnitude, we will determine the influence of different kinds of collisions for the rotational energy transfer. This will allow us to conclude that collisions between heavy species and aluminum monoxide must be responsible for the rotational temperature.

The spatial distribution In figure 3.17, the spatial distributions of the aluminum and the aluminum monoxide species are represented for different time delays. From 4 μ s to 28.8 μ s, the species are not disposed in the same region. Aluminum monoxides are created at the plasma periphery and close to the target surface. Lower temperatures are expected in these regions since temperature gradients can emerge in the plasma. For longer delays, the two species seem to merge into a homogeneous phase. Therefore, considering that the rotational temperature is not measured below 30 μ s, the difference between the temperatures cannot completely be interpreted as a temperature gradient. During most of the temperature comparison (See figure 3.16), all the species are located at the same place. In addition, with the experimental setup, the observation area is few hundreds of micrometer in size. Therefore, we only observed a small area of the plasma where gradients should not be very significant.

Orders of magnitude This finding suggests a deviation from a local thermodynamic equilibrium including the excitation temperature and rotational temperatures. In order to justify this peculiar result, we will establish that the rotational temperature is

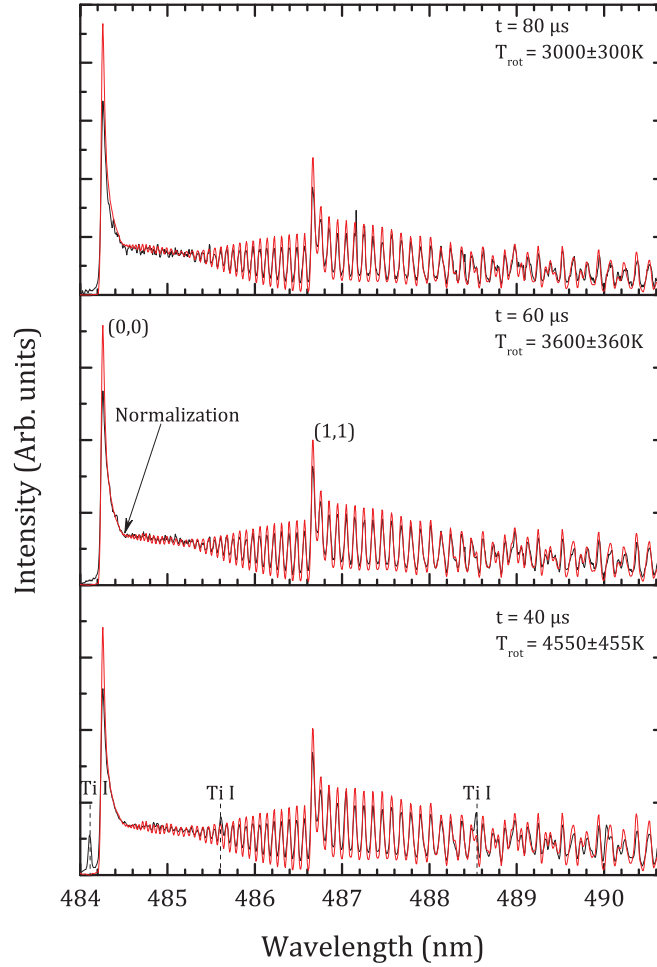


FIGURE 3.15: AlO spectra for different time delays with corresponding fitting curve. The black curve is the experimental one and the red curve is the simulated one. Two Ti I lines are also observed at 40 μ s.

predominantly driven by the collisions between the heavy species. For numerical applications, we assume that the kinetic temperature T^{Kin} of the electrons and heavy species have similar orders of magnitude. We set it to 5000 K. The collisional cross-section, σ , for electron/heavy and heavy/heavy [103] collisions are similar in terms of their orders of magnitude (10^{-15} cm²) for neutral heavy species. Finally, we assume that the heavy species density N_H is greater than or equal to the electron density N_e .

Rotational energy transfer First, we consider the rotational energy transfer due to a collision. This process is a momentum transfer. The transferred mechanical energy between an electron and a heavy species is similar to $E_{e/H} = \frac{m_e}{m_H} k_B T^{Kin}$, while between two heavy species, it is $E_{H/H} = k_B T^{Kin}$. But, the mass of the heavy species, m_H , is approximately 10000 times bigger than the mass of an electron, m_e (43000 for AlO, 16000 for O and 27000 for Al). As a consequence, the energy transfer due to an electron/AlO

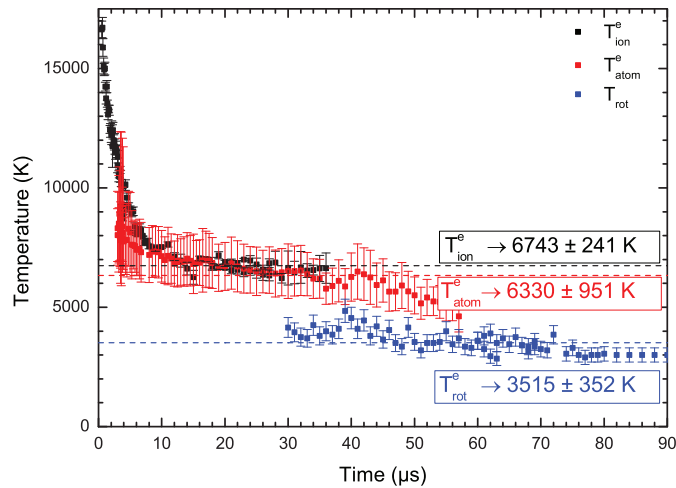


FIGURE 3.16: Temporal evolution of the excitation temperatures of the atoms (Fe I) and the ions (Ti II) and the rotational temperature (AlO). The dotted lines stand for the mean values calculated from $10 \mu s$.

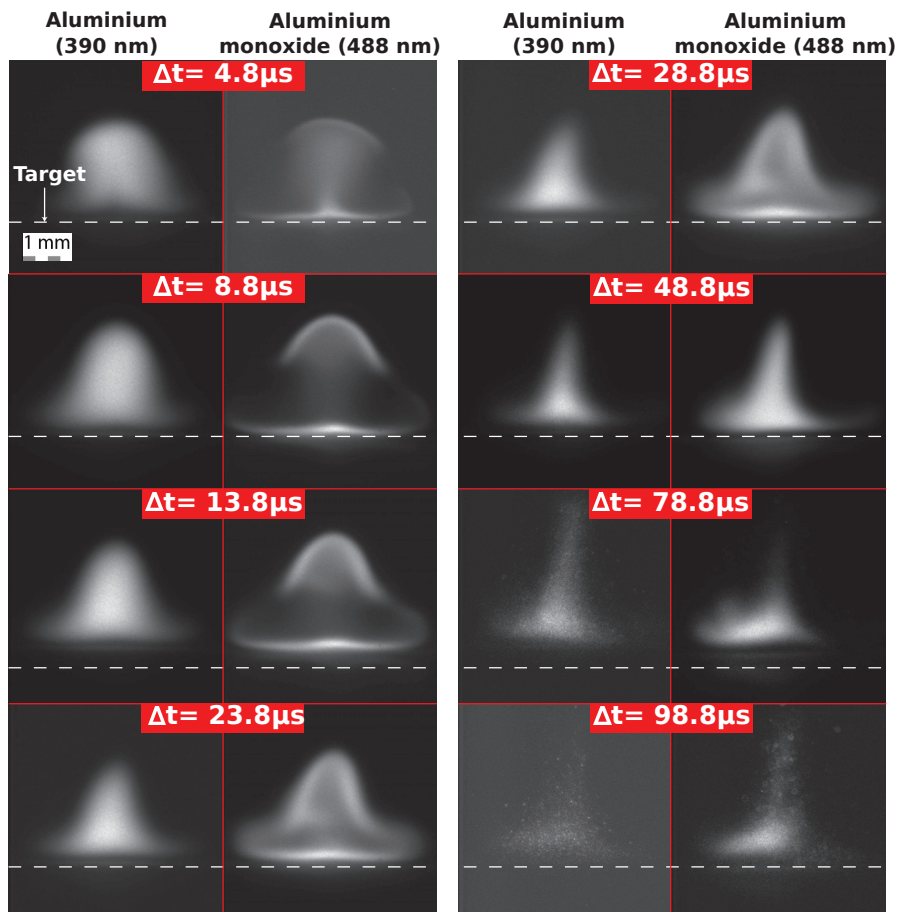


FIGURE 3.17: Temporal evolution of the excitation temperatures of the atoms (Fe I) and the ions (Ti II) and the rotational temperature (AlO). The dotted lines stand for the mean values calculated from $10 \mu s$.

collision contributes 43000 times less than a heavy/AlO collision. Moreover, in a given vibrational state v , the rotational energy is distributed as $B_v K(K+1)$ where K is the rotational quantum number. Evolution from the K to the $K+1$ level requires a collision energy transfer of $2(K+1)B_v$. In terms of orders of magnitude, the energy available after an electron/heavy collision ($E_{e/H} \sim 1 \times 10^{-5}$ eV) is smaller than the rotational constants $B_v \sim 7 \times 10^{-5}$ eV for AlO while the energy available after an heavy/heavy collision ($E_{H/H} \sim 4 \times 10^{-1}$ eV) is four orders of magnitude higher. When K is too high, electrons can no longer provide enough energy, and only heavy/heavy collisions excite the rotational levels used in our fit for T_{rot} .

Time scale of the mechanisms Now we estimate the collision rates and the characteristic times of the process. The rates are generally given by $f = N \times \sigma \times \bar{u}$ where \bar{u} is the average velocity, $\bar{u} = \sqrt{\frac{8k_B T^{Kin}}{\pi\mu}}$ with μ the reduced mass of the two considered species. Therefore, the ratio between the collision rates for electron/heavy, $f_{e/H}$, and for heavy/heavy, $f_{H/H}$, is bounded above by:

$$\frac{f_{e/H}}{f_{H/H}} \leq \sqrt{\frac{m_H}{m_e}} \sim 100 \quad (3.34)$$

There are approximately hundreds of times more collisions between electrons and heavy species than between heavy species alone. Assuming densities of at least 10^{16} atoms/cm⁻³, the mean time between two collisions between heavy species, at most 500 ns, is a couple of orders of magnitude smaller than the time scale of the experiment and the time evolution of T_{rot} . Therefore, we can assume that the rotational levels of the AlO ground state are thermalized, so there is a translational–rotational equilibrium. Then, $\tau_{e/H} \equiv 1/f_{e/H} \sim 3$ ns is short enough to excite the $B^2\Sigma^+$ level of AlO in comparison to its emission lifetime of 116 ns. According to Bruggeman et al. [104], “the electron excitation will basically map the ground state rotational distribution onto the excited state rotational distribution.”

Two collisional processes, two temperatures As a consequence, having more collisions between electrons and heavy species is not critical since only the rotational levels of the ground state require a rotational thermalisation. Also, it is less favourable for the electron gas to drag a diatomic molecule into rotation, especially for the highest rotational levels, since these quantum levels need to be excited via collisions with the heavy species such as ions, atoms or molecules. The low K levels only contribute to the band head, which are not considered in our fit procedure. Therefore, since we only used the high value of K for our calculation, the obtained rotational temperature can be seen as a signature of the kinetic temperature of the heavy species T_{heavy}^{Kin} . Furthermore,

in laser plasmas, the kinetic temperature of the electrons is assumed to be higher than the kinetic temperature of the heavy species. Two different physical processes drive the establishment of the equilibrium for the excitation temperature and the rotational temperature. As a result, the temperatures do not converge to each other.

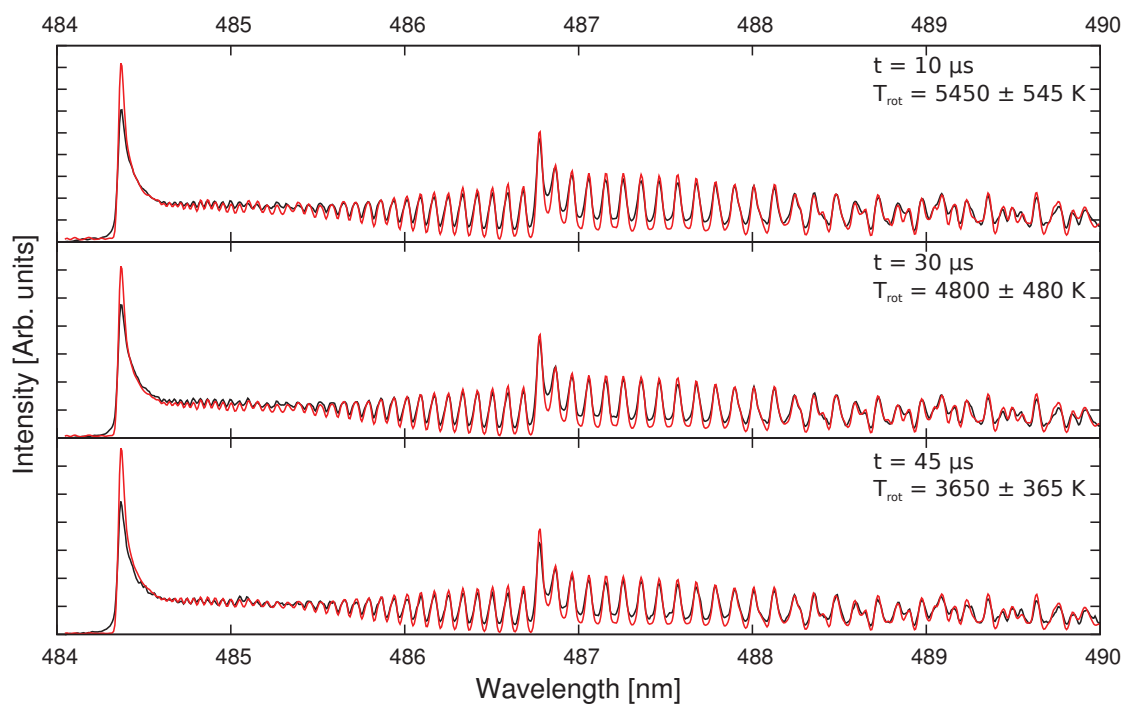
3.3.3 Perspectives on the role of chemical reactions

In the previous section, we demonstrated that electronic temperatures do not necessarily match the rotational temperature. This was explained by the difference in the excitation processes i.e. electronic energy levels can be excited by electron collisions while rotational energy levels need collision between heavy species. Here, I will present two preliminary results obtained for the temperature equilibration. We, first, compared the rotational temperature with the vibrational temperature. Then, we also examined the difference between rotational temperature of two different diatomic species.

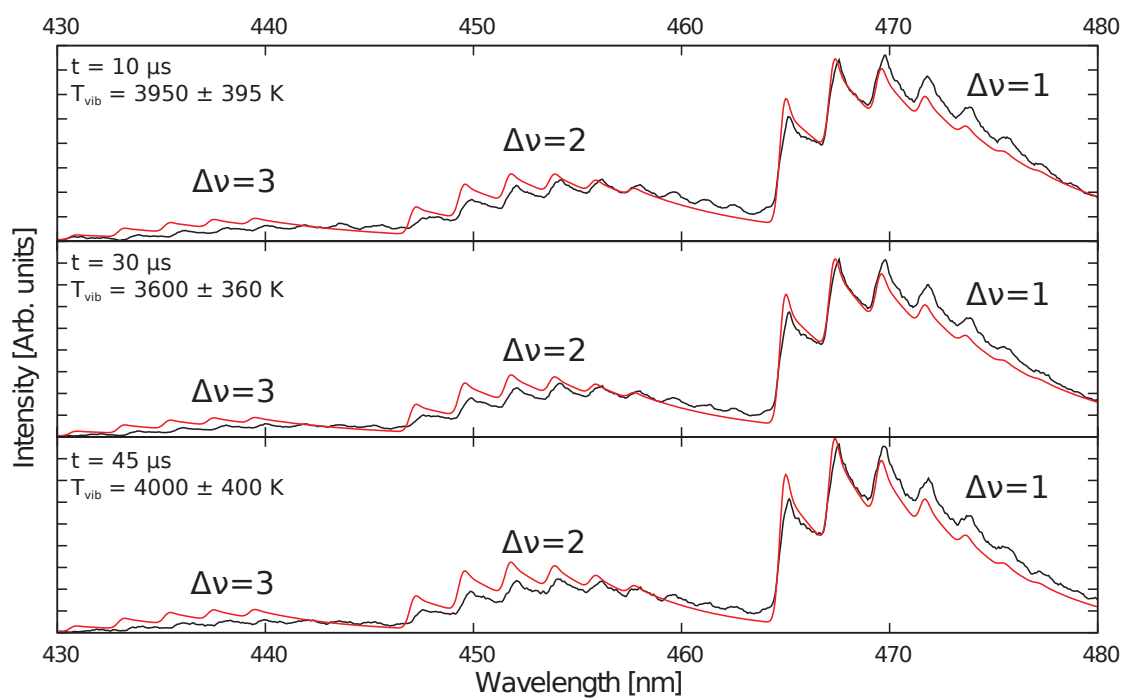
The rotational and vibrational equilibration Rotational and vibrational temperatures are compared for aluminum monoxide. We worked on the ablation of an aluminum oxide Al_2O_3 target. Using two different monochromators, we monitored rotational lines of aluminum monoxide ($\Delta v = 0$) and vibrational lines ($\Delta v = [1, 2, 3]$) [See figure 3.18]. The rotational temperature is deduced from $\Delta v = 0$ using the method previously described in the section 3.2.3. For the vibrational temperature, $\Delta v = [1, 2, 3]$ lines are used to avoid self-absorption of the $\Delta v = 0$ lines. Calculated and experimental spectra are normalized by overall integration. In figure 3.19, the temporal evolution of both temperatures are plotted.

From here, there are two singular observations: **(i)** The two temperatures are not similar, **(ii)** the vibrational temperature does not vary with time.

As initial explanation of **(i)**, the formation of aluminum monoxide does not naturally balance the rotational and the vibrational energy. Indeed, the chemical reactions induce a release in energy which can be distributed among the degrees of freedom i.e. translation, vibration and rotation. Then, the balance between these degrees of freedom is not necessarily uniform thus explaining the observed difference. In order to probe the released energy partitioning, we used Born-Oppenheimer molecular dynamics (BOMD) calculation. The technique employs forces computed from quantum density functional theory [See section 4.2] to deduce the dynamical behavior of the system. Preliminary calculations for the creation of AlO were run at 0 K i.e. no initial kinetic energy which means that the resulting kinetic energy is granted by the decrease of the potential energy. At first, the aluminum atom joins the dioxygen to form AlO_2 . Potential energy surface



(a) Rotational lines.



(b) Vibrational lines.

FIGURE 3.18: AlO rovibrational spectra for different time delays with corresponding fitting curve. The black curve is the experimental one and the red curve is the simulated one.

calculated already identified this molecule as a transition state located in a potential energy well [105]. The molecule vibrates and one oxygen atom is finally detached. AlO

is thus formed and vibration and rotation of AlO is observed. Following these calculations, we still need to deduce the rotational and vibrational energies of the produced AlO. Additional work must also be done to obtain similar computational results at higher temperatures, 4000 K for instance.

In addition, self-absorption is more likely to occur when considering vibrational spectra. This would alter the temperature fitting. Supplementary work on correcting the self-absorption must therefore be done to conclude on this matter (See for examples Rezaei et al. [106] and Hermann et al. [107]).

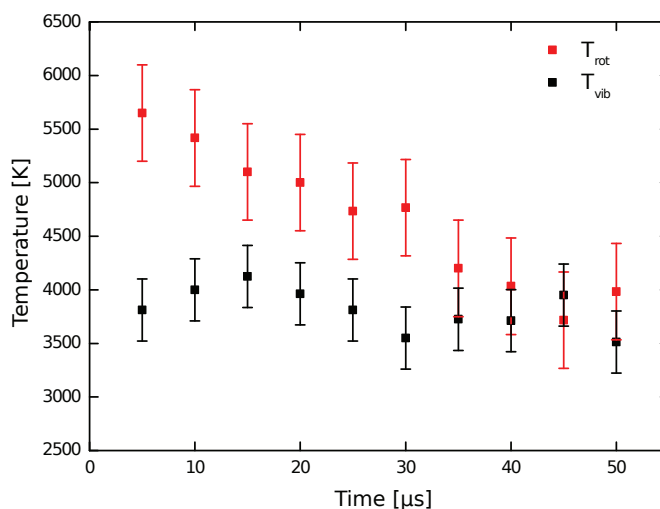


FIGURE 3.19: Temporal evolution of the rotational and vibrational temperatures measured from AlO.

Two temperatures for two molecules Here, we will discuss an other kind of non equilibrium which can occur when comparing rotational temperatures from different diatomic molecules.

We worked on the ablation of a target made of Al_2O_3 (75% Aluminum atomic percentage) and TiO (25% Titanium atomic percentage). This way, the rotational spectrum of AlO and TiO could be measured as a function of the temperature using the same target and under same experimental conditions. In addition, similarly to the work done with rotational temperature of aluminum monoxide AlO [See section 3.2.3], a C++ code was developed to simulate the rotational temperature from titanium monoxide TiO following works of Woods et al. [108] and Hermann et al. [109]. The electronic and vibrational constants are taken from in Phillips et al's work [110] and the rotational constants are found in Ram et al's article [111]. The measurement are done from 705 nm to 711 nm

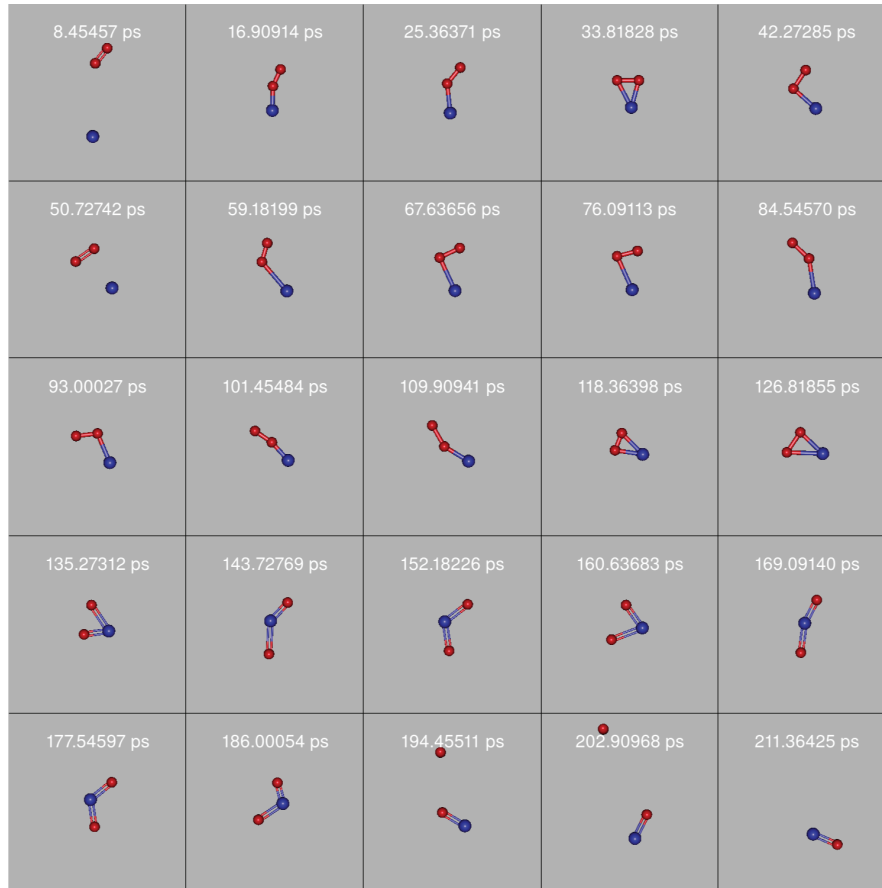


FIGURE 3.20: Dynamical evolution of the sytem made of O_2 and Al obtained via BOMD calculation. The red spheres stand for oxygen atoms and the blue spheres stand for aluminum atoms.

since at these wavelengths, the contribution from $(v'', v') = (0, 0)$ is the most preponderant in comparison to $\Delta v = 1$. Consequently, the vibrational temperature should not play a decisive role.

In figure 3.22, typical experimental curves are plotted along with their corresponding fitting curves. The rotational lines were resolved enough from 25 μs to 60 μs for both AlO and TiO. The temporal evolution of the two rotational temperatures is given in figure 3.21. From 25 μs to 40 μs , we can observe a difference between the two temperatures. Then, they converge towards the same value around 4000 K.

From here, two explanations can be discussed. First, AlO and TiO can be spatially located at different areas of the plasma because aluminum and titanium atoms do not have the same atomic weight. The difference in temperature would then be explained by a temperature gradient. Yet, as explained in section 3.3.2, the observation area should not be large enough to observe such a gradient. As a second explanation, the chemical reactions forming TiO and AlO are both exothermic but they can release a different

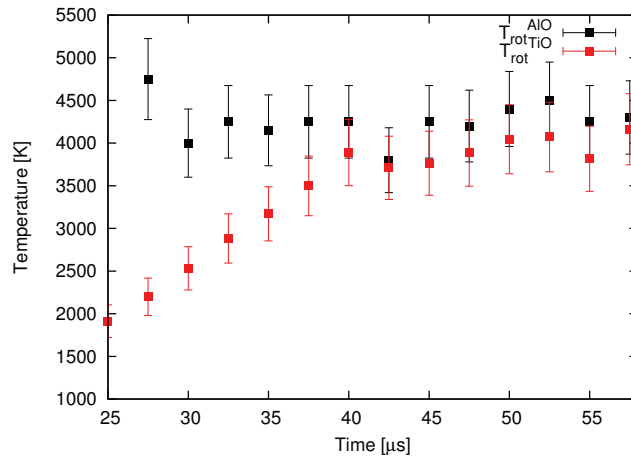
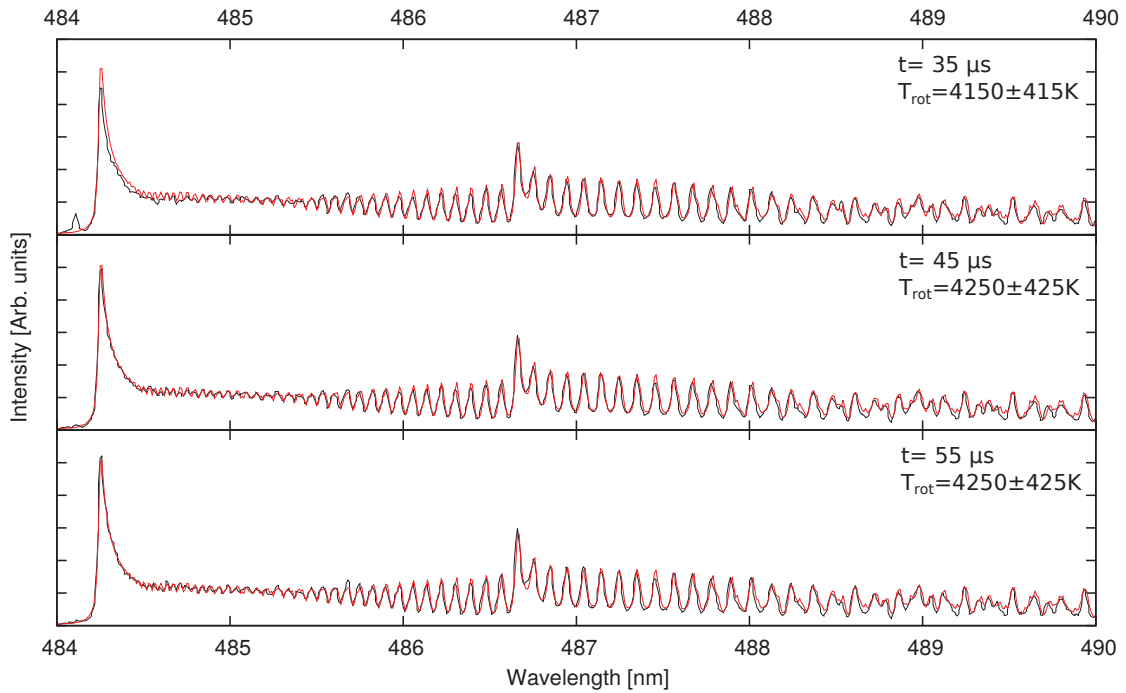
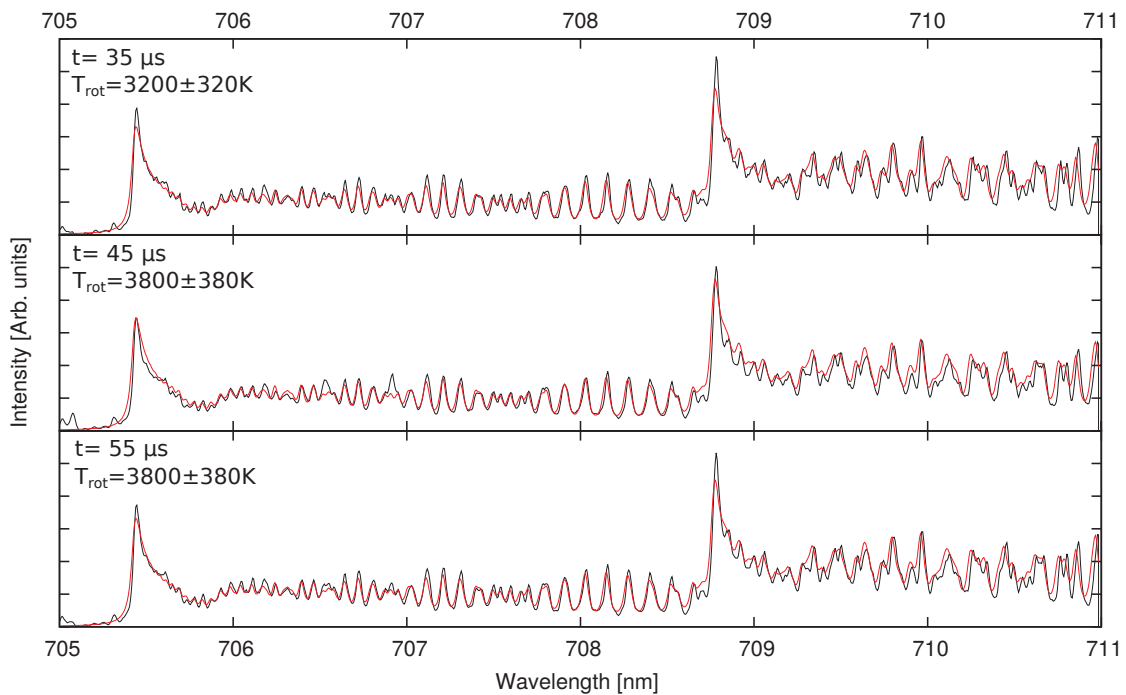


FIGURE 3.21: Temporal evolution of the rotational temperatures measured from AlO and TiO rotational spectra.

amount of energy which would then lead to different rotational temperatures. As in the previous section, BOMD calculations on the chemical dynamics may give insights on this matter.



(a) Aluminum monoxide (AlO)



(b) Titanium monoxide (TiO)

FIGURE 3.22: Spectra for different time delays with corresponding fitting curve (FWHM=0.032 nm). The black curve is the experimental one and the red curve is the simulated one.

3.4 Conclusion

Plasma spectroscopy allows one to probe the electron density, the temperature and the relative chemical composition. In water, experimental difficulties may appear due to the liquid confinement. Consequently, ions and atoms cannot be used in water, atoms and diatomic molecules are used instead. We have been able to measure the electron density for the ablation of alumina in water and showed that it was ten times higher than in air. Also, rotational temperatures have been obtained using aluminum monoxide lines. $2.0 \mu\text{s}$ after the laser pulse, it is equal to $3400 \pm 500 \text{ K}$. The chemical composition was then probed by monitoring the ratio between aluminum monoxide and aluminum emissions. This ratio was corrected to reach a ratio in number of particles using appropriate partition functions. From this, it appeared that the plasma is increasingly composed of aluminum monoxide.

In addition, these results raised our attention towards equilibration processes. First, McWhirter criteria compare electron collisions with other energy transfer processes and determine a condition in the electron density to reach equilibrium between electronic temperatures of different species. However, it does not inform on other types of equilibration. For instance, we have been able to prove that although McWhirter criteria are fulfilled and electronic temperatures of ions and atoms are equal, the rotational temperature is not necessarily the same. To explain this observation, we considered an other excitation process which is the collisions between heavy species. Then, we demonstrated that this second collisional process is responsible for the rotational levels excitation which explains why two different temperatures are observed. Finally, we performed two additional studies. We discussed the equilibration between vibrational and rotational distributions and showed that they do not naturally match. Also, when comparing rotational temperatures from different diatomic species, a difference can be observed. These two striking results may be analyzed under the light of chemical reactions.

Chapter 4

A microscopic approach to the nucleation of nanoparticles

"Everything should be made as simple as possible, but not simpler."

Albert Einstein

Contents

4.1	Classical nucleation theory and its limitations	58
4.1.1	Nucleation core	58
4.1.2	Beyond classical nucleation theory	60
4.2	Computational chemistry to investigate the intermediate clusters	62
4.2.1	Computational methods	63
4.2.2	The case of aluminum oxide clusters	66
4.3	A thermochemistry model for the gas composition and its experimental justifications	70
4.3.1	Theoretical model	70
4.3.2	Application for the ablation in air	73
4.4	An extension towards lower temperature	75
4.5	Conclusion	77

PLASMA spectroscopy is a powerful technique to characterize the early time scales after the laser ablation. We have been able to implement this method to probe the chemical composition and the temperature in the first microseconds after underwater laser ablation. We showed that aluminum atoms turn rapidly into aluminum monoxide. Subsequently, chemical reactions should form bigger molecules until reaching a particular one, Al_xO_y . Then, aggregation occurs and these Al_xO_y should bind one to the other and finally form the alumina nanoparticles. In that case, this seed is called the *critical nucleus*, or *nucleation core*, since it drives the mechanisms from chemically induced transformations to growth by simple diffusion. However, the steps leading to the appearance of the nucleation core cannot be explored experimentally since the plasma is no longer optically active. To overcome this difficulty, we developed a molecular approach

to nucleation based on quantum chemistry. In this chapter, we will first report the theoretical formalism for classical nucleation and exhibit its limitations for nanoparticles. Then, we will describe how computational chemistry can be used to determine molecular cluster structures. In the last section, we demonstrate how this approach allowed us to derive a thermochemistry model for the gas composition in laser ablation. We will use this method to investigate the nature of the nucleation core in the laser ablation process.

4.1 Classical nucleation theory and its limitations

A liquid considered homogeneous is in fact always under fluctuations. These changes may lead to small molecular aggregates with higher mass density. So, little nuclei of crystal spontaneously appear. When the thermodynamic conditions (T, P) set the liquid as stable, the nucleus disappears. Otherwise, depending on its size, it can either dissolve or it can grow. The nucleus would then expand and change the whole phase of the system. The particular size at which the nucleus grows is called the *critical radius*. This phenomenological approach is called *classical nucleation theory* and was originally derived by Volmer, Weber and Farkas [112, 113] followed by Becker and Doring [114]. It is observed in crystallization but it can also be observed in any first-order phase transitions such as melting, vapor-phase condensation, boiling, solid-state precipitation, glass and binary separations [115–118]. A very nice picture of the nucleation stages was recently published by Chakraborty et al. [119]. They studied the nucleation of NaCl crystal in water using molecular dynamics simulations and followed the early-stage nucleation leading to the growth of the crystal. In figure 4.1, one can observe that after 90 ns, a crystal-like structure seems to appear spontaneously and grow hereafter.

4.1.1 Nucleation core

The nucleation core size and its appearance rate are two characteristics that ought to be investigated. Let us consider n_0 moles of pure phase in liquid phase at the temperature T_0 and the pressure P_0 . We will suppose the creation of a crystal nucleus of n moles at T_c and P_c . The grand canonical point of view is adopted, the mechanical and thermal equilibria are established rapidly leading to:

$$T_c = T_0 \quad \& \quad P_c = P_0 + \frac{2\gamma}{r} \quad (4.1)$$

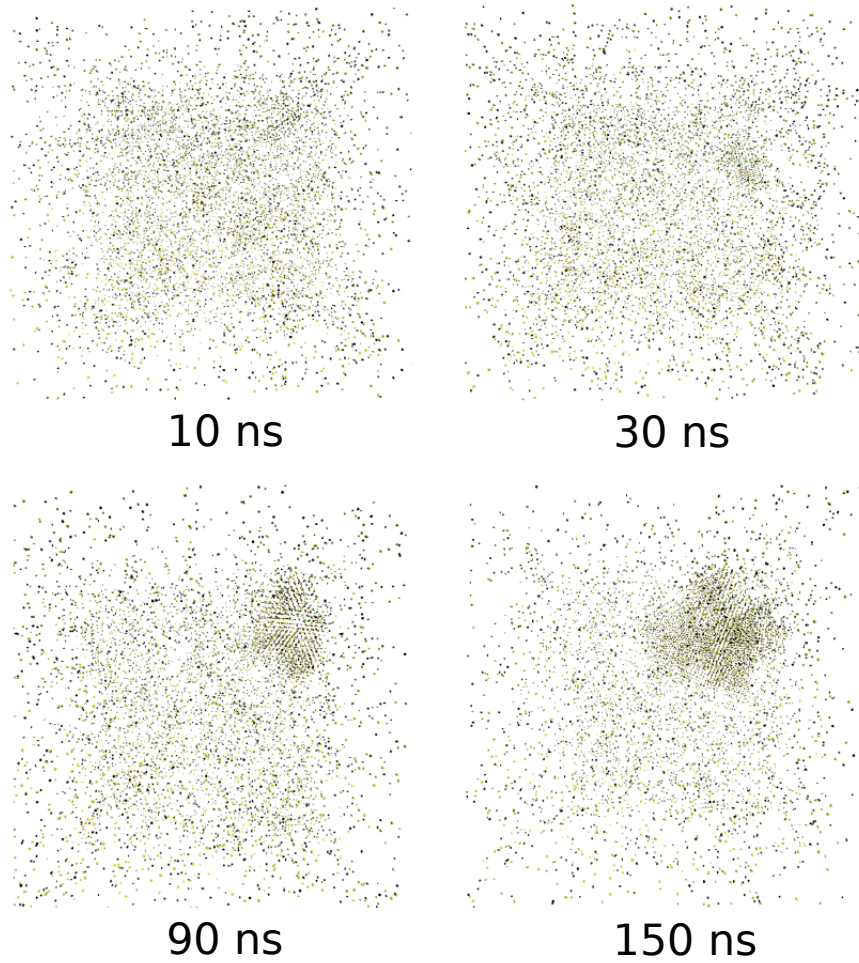


FIGURE 4.1: Temporal evolution of the Na⁺ (blue) and Cl⁻ (yellow) ions during the crystal growth in water. Figures are reprinted from Chakraborty et al. [119].

where γ is the surface tension and r is the nucleus size. We define the thermodynamical potential, G , as the Gibbs free enthalpy:

$$G \equiv U - T_0 S + P_0 V \quad (4.2)$$

Let us consider the evolution from the homogeneous liquid to the same homogeneous liquid with a crystal nucleus inside it. The variation of G induced by such a transition is given by the difference in chemical potential plus the surface energy induced by the appearance of an interface. More explicitly, we have:

$$\Delta G_0 = n \{ \mu_c(T_0, P_c) - \mu_l(T_0, P_0) \} + \gamma s \quad (4.3)$$

where n is the number of moles, s is the nuclei surface and μ is the molar chemical potential. The r dependence of n and s allows us to describe ΔG_0 as a function of r :

$$\Delta G_0(T_0, P_0, r) = \frac{4\pi r^3}{3v_c(T_0, P_0)} [\mu_c(T_0, P_c) - \mu_l(T_0, P_0)] + 4\pi\gamma r^2 \quad (4.4)$$

where v_c is the molar volume of the nucleating phase. This expression for ΔG_0 is called the *capillary approximation*. If the crystal phase is the most stable, $\mu_c(T_0, P_c) < \mu_l(T_0, P_0)$, one can calculate a critical value of r following the condition $\frac{\partial \Delta G_0}{\partial r} \Big|_{r=r^*} = 0$,

$$r^* = \frac{2\gamma v_c(T_0, P_0)}{\mu_l(T_0, P_0) - \mu_c(T_0, P_c)} \quad (4.5)$$

r^* is the critical radius, i.e. the smallest size of a germ that can turn into the new phase. In homogeneous nucleation, spontaneous fluctuations are required to create such a germ which would then produce the phase transition. In addition, the nucleation rate, J i.e. the number of clusters of the new phase appearing per unit of time and volume can be derived as a Arrhenius's perspective using:

$$J = K \exp\left(-\frac{\Delta G_0(T_0, P_0, r^*)}{kT_0}\right) \quad (4.6)$$

where K is the kinetic prefactor according to Becker and Döring [114]. For homogeneous nucleation in supersaturated vapor, CNT appears to be very successful. Indeed, Strey et al. observed nucleation events in an expansion chamber loaded with 1-butanol vapor and measured the number of droplets through a Lorentz-Mie scattering measurement [120]. They calculated nucleation rates and proved that the experimental results agreed with CNT predictions. More recently, Diemand et al. used large-scale molecular dynamics simulations to cover the homogeneous bubble nucleation (liquid-to-vapor transition) [121]. Half a million Lennard-Jones atoms during 56 million time steps were examined allowing the authors to observe the nucleation at unprecedented accuracy. In this context, they showed that CNT could be applied to predict the nucleation rate.

4.1.2 Beyond classical nucleation theory

Limitations CNT is very practical to interpret classical phase transitions especially for gas to liquid transitions. However, this approach still remains controversial for quantitative results [122–124]. More particularly, for the growth of nano-materials, the approach has several limitations.

The capillary approximation assumes that the nucleation core properties are equivalent to the bulk one. Especially, the surface tension γ is considered equal when changing

the size of the nucleus. This hypothesis is very crude since the notion of volume and surface is not so consistent for small clusters where there can be more molecules located at the surface than in the volume. In addition, γ can hardly be approximated to the bulk value. Indeed, for liquid in vapor, Tolman proved that the surface tension decreases with the droplet size [125]. Also, according to the experimental observation of Ostwald's rule, the most stable phase is not always the one that grows first. In other words, there is no reason why the nucleation core should be similar to the final phase. Geometrical reorganisation can occur. Therefore, the parameters such as the molar volume and the surface tension of the growing cluster can be different from those of the final phase. Moreover, in CNT the nucleus is considered homogenous, only one parameter drives the nucleation i.e. the nucleus radius.

Other approaches to nucleation Historically three paths have been studied to improve CNT:

- *Modification of the capillarity approximation:* Lothe and Pound proposed to add translational and rotational degrees of freedom in the free energy expression [126]. This development results in an increase of 10^{17} in the nucleation rate leading to an even worse accuracy than CNT. To improve the free energy expression Dillmann and Meier added semi-phenomenological considerations by trying to take into account the change of the surface tension with the size of the cluster [127, 128]. An agreement with experimental results was found for the vapor-to-liquid transition in several systems such as nonane, water and alcohols. More developments can be found in Strey's article [120].
- *Kinetic approach:* Similarly to the thermodynamic approach to CNT, a cluster dynamic resolution can be derived [116]. It is a kinetic method based on a master equation:

$$\frac{\partial C(n, t)}{\partial t} = \beta(n-1)C(n-1, t) - \gamma(n)C(n, t) \quad (4.7)$$

$$-\beta(n)C(n, t) + \gamma(n+1)C(n+1, t) \quad (4.8)$$

where $C(n, t)$ designates the concentration of clusters with n monomers and where $\beta(n)$ and $\gamma(n)$ designate respectively the forward rate at which the cluster of n gains particles and loses particles. Martin et al. proved that this second approach is fairly equivalent to the CNT [129]. One breakthrough concerns nonetheless the fact that β_n and γ_n can be parametrized through the knowledge of the cluster properties [130]. Very recently, Lee et al. used computational chemistry to optimize $(\text{TiO}_2)_n$ clusters and extrapolated the size dependence of the free energy

to build the kinetic model of nucleation [131]. However, their results ought to be confirmed experimentally and lack considerations on the stoichiometry of the clusters. They imposed the atoms to recombine via $(\text{TiO}_2)_n$ molecules which is not evident especially at high temperature.

- *Classical density functional theory*: The first set of methods concerned thermodynamics of macroscale systems while the second set of methods was focused on a microscopic approach. In classical density functional theory, an intermediate approach is followed where the macroscopic scale is taken into account through the use of an average density and where the calculations are done at molecular distance scales. The free energy is then expressed as a functional of the density and the challenge is to determine a clear picture of the functional and the density. In addition, the nucleation rate expressed in the Arrhenius's perspective [See equation 4.6] can be completed through diffusion equation in space [132]. For additional information, one can refer to these articles [133–135].

For further details on the CNT's limitations, the reader can refer to Oxtoby's article [136]

Regardless of the employed method, approaches based on stoichiometric growth should be avoided for nanoparticle crystallization since chemically induced transformation must be considered. In the contexts of PLAL and synthesis of aluminum oxide, we deal with a binary system made of aluminum and oxygen atoms which is driven in a highly non equilibrium states due to the liquid confinement. The synthesized nanoparticles still hail from nucleation and growth. The nature of the nucleation core however is not clear and can hardly be explored experimentally. In the following section, we will describe how computational chemistry can be used to identify the molecular steps leading to the creation of the nucleation core.

4.2 Computational chemistry to investigate the intermediate clusters

Emerging with the birth of quantum mechanics, computational chemistry has attracted more and more attention thanks to the increase of computer capacities. The general idea is to use the power of computers to solve mathematically problems from chemistry. More precisely, the aim of computational chemistry is to provide quantitative information on the structural and the thermodynamic properties of materials. In this section, I will

begin by briefly reviewing different methods. Then, I will describe the approach we used to investigate the alumina clusters.

4.2.1 Computational methods

Three methods for computational chemistry are commonly used: ab initio, quantum density functional theory (DFT) and semiempirical approaches. They are all derived from the the Schrödinger equation:

$$\hat{H}\Psi = E\Psi \quad (4.9)$$

where Ψ is a wavefunction, E is the total energy and \hat{H} is the Hamiltonian operator expressed under the Born-Oppenheimer approximation [137] as follow:

$$\hat{H} = - \sum_i^{electrons} \frac{\nabla_i^2}{2} - \sum_i^{nuclei} \sum_j^{electrons} \frac{Z_i}{r_{ij}} - \sum_{i < j}^{electrons} \sum \frac{1}{r_{ij}} \quad (4.10)$$

where r_{ij} is the distance between the particles i and j , ∇_i^2 is the Laplacian operator acting on the particle i , Z_i is the charge of the nucleus i . The first term designates the kinetic energy of each electron while the nuclei are considered fixed. In the second term, the Coulombic interaction between the electrons and the nuclei are grouped. In the last term, we consider the electron-electron repulsion.

Ab initio methods In Latin, ab initio means "from the beginning". In the particular context of computational chemistry, this term designates all the methods in which nothing more than the Schrödinger equation is exploited. The first attempt at using this approach concerns the Hartree-Fock (HF) calculation. The idea is to approximate the electron-electron repulsion term to consider only one-electron interactions with an averaged Coulombic field meaning that no correlation between electrons is taken into account. In other words, the behavior of electrons only depends on the positions of the nuclei. In addition, the wavefunctions are constrained under linear combinations of atomic orbitals (Hartree-Fock orbitals).

The accuracy of the calculation is improved by taking into account electron correlations. The Møller-Plesset approach is then often employed. Here, the wavefunction is considered in a perturbation theory and each additional term constitutes an improvement of the calculation. These calculations are called MPn methods where n designates the number of iterative perturbations.

Quantum Density functional theory In the ab initio approach, the Hamiltonian is fully described and obtaining accurate wavefunctions constitutes the cornerstone of the calculation. In density function theory, the general idea is to substitute the wavefunction with the electron density, $\rho(\vec{r})$ in order to reduce the number of degrees of freedom from $3N$ to 3 . However, in this formalism, the Hamiltonian is no longer determined analytically since it is no longer a functional of the wavefunction but of the electron density. In the DFT approach, the Coulombic interaction is then separated into two terms, an electron-electron interaction, E_{ee} , and an "external potential", V_{ext} , which takes into account the nuclei attraction. Hohenberg and Kohn proved two theorems that set the basis of DFT in 1964. **(i)** First, they demonstrated that there exists an unequivocal relation between the electron density and this external potential which then could determine the classical Hamiltonian and the wavefunction. In other words, the two formalisms are completely equivalent. For one expression of ρ , there exists a unique V_{ext} so that the energy, E is given by:

$$E[\rho] = V_{ext}[\rho] + T[\rho] + E_{ee}[\rho] = V_{ext}[\rho] + F_{HK}[\rho] \quad (4.11)$$

where $T[\rho]$ is the total kinetic energy. The two terms are regrouped and named the functional of Hohenberg and Kohn, F_{HK} which is universal for any system since ρ only determines V_{ext} . But no analytical expression for the functional of Hohenberg and Kohn has been found yet, mostly due to the complexity in expressing the kinetic energy in terms of a functional of ρ . **(ii)** Later, Hohenberg and Kohn also showed that the density obeys a variational principle where the ground state energy E_0 can be expressed as:

$$E_0 = \min_{\rho} E[\rho] \quad (4.12)$$

thus allowing to find E_0 by minimizing the expression of $E[\rho]$ with respect to ρ . We emphasised previously that the critical point was to determine F_{HK} . In 1965, Kohn and Sham highlighted that the problem could be considerably reduced by substituting the interacting electrons moving in V_{ext} for non-interacting electrons moving in an fictive potential V_s . In practice, one defines the fully classical term of the Coulombic interaction, $J[\rho]$, following:

$$J[\rho] = E_{ee}[\rho] - E_q[\rho] = \frac{1}{2} \int \int \frac{\rho(\vec{r})\rho(\vec{r}')}{|\vec{r} - \vec{r}'|} d\vec{r}d\vec{r}' \quad (4.13)$$

where $E_q[\rho]$ is the quantum term of the Coulombian interaction which takes into account the exchange and the correlation terms. From here, $E[\rho]$ is rewritten as:

$$E[\rho] = T_s[\rho] + J[\rho] + V_{ext}[\rho] + T[\rho] - T_s[\rho] + E_{ee}[\rho] - J[\rho] \quad (4.14)$$

where $T_s[\rho]$ designates the kinetic energy of the fictive system meaning the non-interacting electrons moving in the fictive potential V_s . The first three terms can be calculated analytically while the four others are regrouped into the exchange-correlation functional, E_{xc} so that:

$$E[\rho] = T_s[\rho] + J[\rho] + V_{ext}[\rho] + E_{xc}[\rho] \quad (4.15)$$

This designation of E_{xc} arises from the fact that the classical electron-electron repulsion does not take into account correlation and exchange in the electron-electron interaction. Indeed, to get a better perception of this approximation, for a one electron system, J , as expressed in the equation 4.13, is not equal to zero while no electron-electron interaction should emerge. There is a need for a correction term which would stand as a "hole" in the system. This particular case materializes the concept beneath the exchange-correlation term.

From here, according to the Kohn-Sham theorem, the fictitious system made of non-interacting electrons moving in the effective potential V_s should have the same energy as the real one given by the equation 4.15:

$$T_s[\rho] + V_{ext}[\rho] = T_s[\rho] + J[\rho] + V_s[\rho] + E_{xc}[\rho] \quad (4.16)$$

By differentiating with respect to the electron density ρ , one obtains an equation to link V_s the fictive potential to the real energy components:

$$V_s = V_{ext} + \int \frac{\rho(\vec{r}')}{|\vec{r} - \vec{r}'|} d\vec{r}' + V_{xc} \quad (4.17)$$

where V_{xc} is the functional derivative of E_{xc} . Granted by an expression of E_{xc} , one can calculate V_s and deduce ρ . The procedure is then reiterated to deduce from ρ a new value of V_s and the calculation is stopped when both V_s and ρ converge. Yet, the calculation of V_s requires the knowledge of the exchange correlation functional, E_{xc} . Practically, different expressions for E_{xc} have been developed from fundamental quantum mechanics or from parametrizing functions reproducing experimental results.

The breakthrough lies in the fact that calculations are no longer made within a 3N dimensional space (3 per electrons) but within a 3 dimensional space. This achievement reduces considerably the computational time. However, the choice of the functional is crucial to performsho accurate calculation.

Semiempirical approach In a semiempirical calculation, the wavefunction/Hamiltonian formalism is adopted. However, numerous approximations are used to facilitate

the computation. The core electrons are often neglected just like some of the two-electron interactions since for large molecules the term $\frac{1}{r_{ij}}$ can be considered as equal to zero. Apart from these mathematical approximations, the correlation between electrons that were omitted in the Hartree-Fock calculation are now approximated through several parameters. These parameters are chosen to reproduce experimental results and the best ab initio calculations. This parametrization is the reason why the method is called "semiempirical".

For more details, please refer to books and reviews describing mathematically and qualitatively methods of computational chemistry [138–140].

4.2.2 The case of aluminum oxide clusters

Review of the previous studies on aluminum oxide clusters The main idea beneath the previous works done on aluminum oxide clusters was to use computational chemistry to understand the photoelectron spectra. Indeed, Desai et al., for example, focused on Al_xO_y^- with $x = 1 - 2$ and $y = 1 - 5$ [141]. They calculated the binding energy and vibrational frequencies of Al_xO_y^- clusters with their excited states but only clusters from specific symmetry properties were considered. Later, Ghanty et al. accomplished a similar work for aluminum clusters with more atoms of aluminum i.e. Al_3O_2 and Al_3O_3 [142]. This time, HF and DFT were used and a full structural characterization was presented. Again, photoelectron spectra were simulated and a qualitative agreement with experimental measurements was found. The group of Sülzle published two articles in 2000 and in 2005 where they worked on bigger clusters until Al_4O_4 [143, 144]. They showed first that the functional named BP86/6-31G(d) was a good compromise between computational cost and accuracy for Al_4O_4 . Then, they performed geometrical optimization on all the clusters Al_xO_y for $[x, y] \in [1, 4]$. In addition, more recently, several papers have been published specifically on $(\text{Al}_2\text{O}_3)_n$ [145–150]. Especially, we would like to mention the work of Sharipov et al. where the heat capacity of clusters with $n \in [1 : 4]$ were calculated [147]. Also, in both articles written by Rahane et al. and Li et al., a systematic geometrical optimization approach was used [145, 146]. Indeed, they used, respectively, a generic algorithm and simulated annealing calculations. Moreover, Rahane pushed the calculations to $(\text{Al}_2\text{O}_3)_{10}$ and showed that the clusters are more similar to γ - (Al_2O_3) than to α - (Al_2O_3) . This latter result could be related to the work already mentioned in the chapter 2 on alumina structural stability with respect to size [60] where it was shown that γ - (Al_2O_3) should be the most stable structure below 10 nm.

This short review illustrates the idea that aluminum oxide clusters have been explored by numerous research groups in the past two decades. However, no systematic optimization approach for the structures has been employed to cover both small clusters and big ones. Also, few papers performed calculations at ab initio levels of theory. Moreover, while stoichiometrically stable clusters i.e. $(\text{Al}_2\text{O}_3)_n$ were studied frequently, no calculation has been done to address out-of-stoichiometry clusters such as Al_xO_y . In the next paragraph, we propose a systematic optimization approach combining a semi-empirical approach with DFT and ab initio calculations to cover clusters Al_xO_y with $[x, y] \in [1, 12]$ in the most stable geometry but also in more unstable isomers.

A systematic optimization approach Figure 4.2 reviews schematically the computational algorithm used for the structural investigation. For each value of x and y , we start from a set of 1000 geometries where atoms are randomly disposed with interatomic distances corresponding to the covalent bond distances. The system is then relaxed via a PM3 semi-empirical method [151]. The remaining geometries are then optimized using Density Functional Theory (DFT) calculation. Two sets of bases are used successively, B3LYP/6-31G* and B3LYP/6-311+G(3df,3pd).

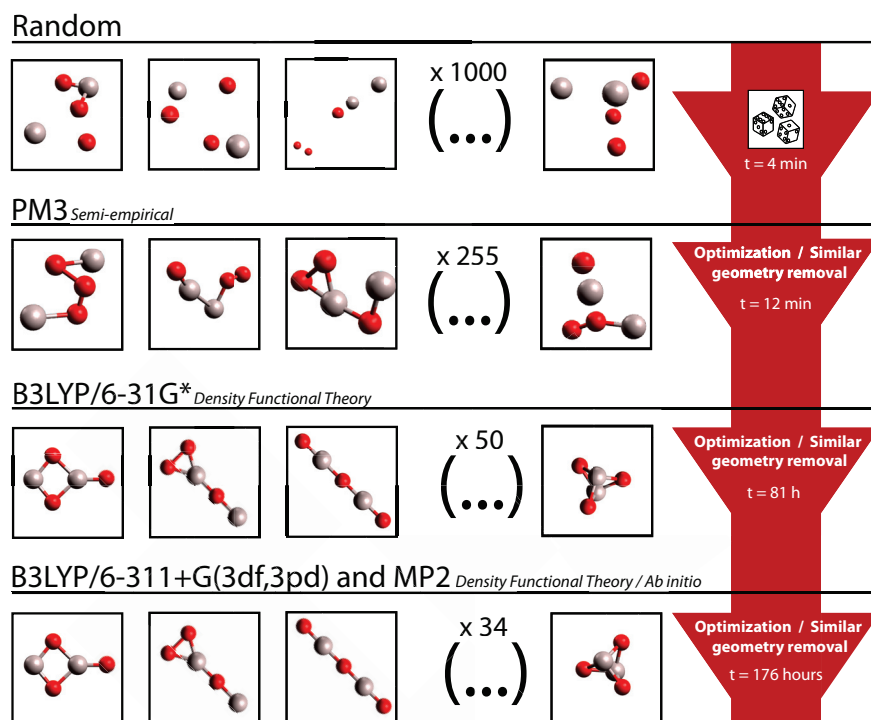


FIGURE 4.2: Computational optimization algorithm illustrated by the example of Al_2O_3 molecules. After each step, similar geometries are removed. The number of remaining geometries is indicated above the brackets. The time corresponds to the computational time for each step.

The dissociated geometries are removed and only geometries whose energy is at most 2 eV higher than the ground state are kept as the others are not relevant for the temperatures studied. For the biggest clusters $(\text{Al}_2\text{O}_3)_3$ and $(\text{Al}_2\text{O}_3)_4$, the structures published by Sharipov et al. [147] were used as inputs in our optimization process. DFT and MP2 calculations were performed with the Gaussian09 D01 revision.[152]

The Gibbs energies were determined using MP2 and B3LYP according to the following steps. The harmonic frequencies were calculated by B3LYP/6-311+G(3df,3pd) using the structures optimized. MP2 thermochemistry was determined by adding B3LYP thermal correction factors to the MP2 single-point energies and is reported as MP2/6-311++G(3df,3pd)//B3LYP/6-311+G(3df,3pd).

We investigated all the molecular formulas following $(x, y) \in [1; 4]$. In addition, two stoichiometric trends were followed, $(\text{AlO})_n$ and $(\text{Al}_2\text{O}_3)_n$. $(\text{AlO})_n$ with $n \leq 8$ were chosen because Patzer et al. demonstrated that for clusters with x and y smaller than 4, this stoichiometry is the most stable [143]. $(\text{Al}_2\text{O}_3)_n$ with $n \leq 4$ were investigated because it corresponds to the bulk stoichiometry. The figure 4.3 shows the most stable structures obtained in this work.

Comparison with previous works For most of the molecules, the results are consistent with various work published previously [143, 146, 147].

Nevertheless, for others clusters such as AlO_4 and Al_2O_3 , our most stable structures are different from Patzer's work [143]:

- For AlO_4 , the most stable structure obtained with our method places the aluminum in the center of 4 atoms of oxygen regrouped in pairs [See figure 4.4(a)]. We optimized both geometries using BP86/6-31G(d), and just like in Patzer's article it was shown that our structure remains the most stable regardless of the level of theory used for optimization. As a consequence, our optimization approach allowed us to determine more structures than the Patzer's method since it is more systematic.
- For Al_2O_3 , the two structures are very similar in energy using BP86/6-31G(d) while the kite-shaped is slightly more stable [See figure 4.4(b)]. But, using MP2/6-311+G(3df,3pd), the linear structure is found to be indeed more stable.

The method presented in figure 4.2 displays two main advantages. First, it is systematic and allows for the investigation of multiple structures at a time without any

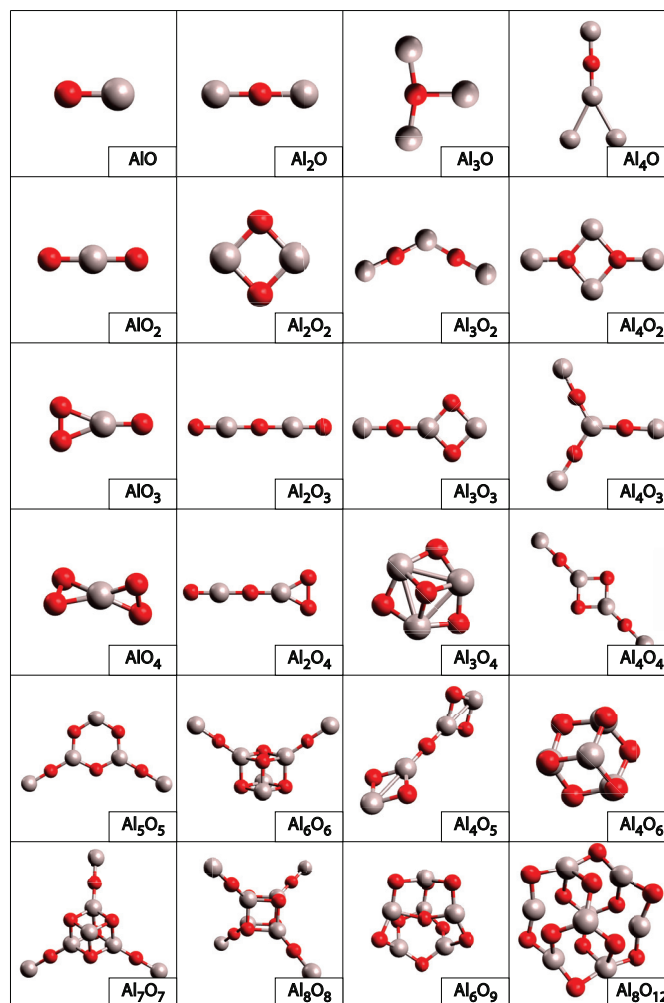


FIGURE 4.3: Most stable structures obtained at MP2/6-311++G(3df,3pd)//B3LYP/6-311+G(3df,3pd) level of theory. The grey spheres and the red spheres correspond respectively to the aluminum atoms and the oxygen atoms.

biased consideration of symmetry. Then, the level of theory reaches ab initio MP2/6-311+G(3df,3pd) and is therefore more accurate when it comes to the calculation of energies.

Based on these isomers, we can derive the equilibrium composition of a gas composed of aluminum and oxygen atoms as a function of the temperature and the initial proportion of elements. To that end, we will first introduce the Van't Hoff law which characterizes the equilibrium condition between chemical components and then we will show how to use it in practice.

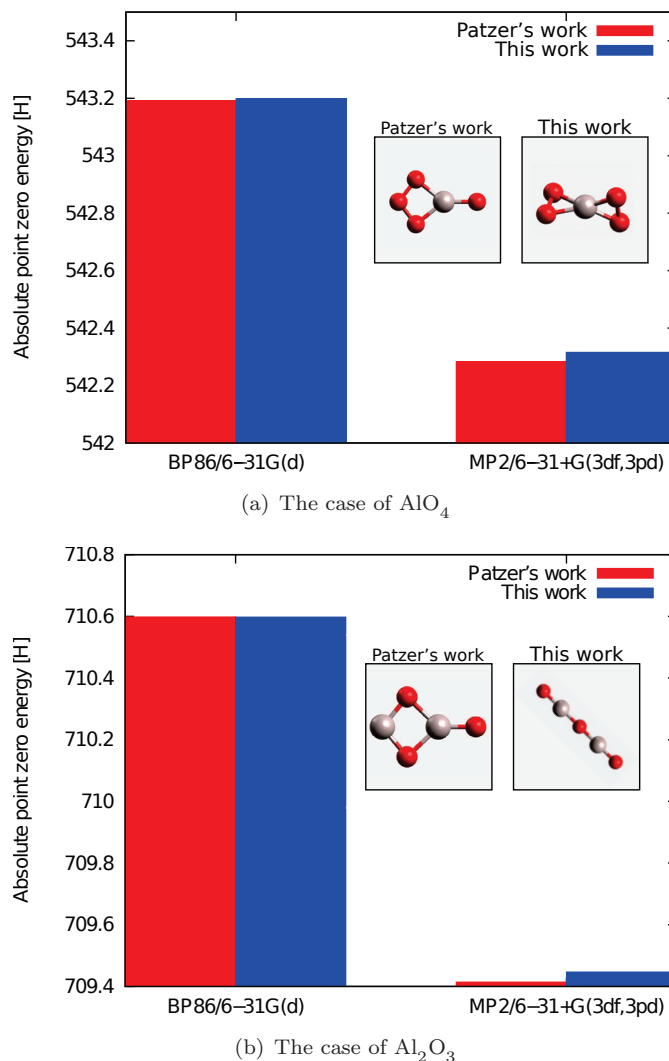


FIGURE 4.4: Absolute zero point energy for two isomers at different levels of theory.

4.3 A thermochemistry model for the gas composition and its experimental justifications

4.3.1 Theoretical model

The Van't Hoff law Let us consider a chemical reaction such as :

$$\sum_{i=0}^n \nu_i X_i = 0 \quad (4.18)$$

where X_i are the chemical compounds and ν_i are the stoichiometric coefficients that can be either positive or negative. The expression of the chemical reaction implies a

relationship between the different numbers of molecules N_i :

$$\frac{dN_1}{\nu_1} = \frac{dN_2}{\nu_2} = \dots = \frac{dN_n}{\nu_n} \quad (4.19)$$

At equilibrium, G reaches a minimum at T and P constants so that $dG = -SdT + VdP + \sum_{i=0}^n \mu_i dN_i = 0$. Considering the equation 4.19, we can write:

$$\sum_{i=0}^n \nu_i \mu_i(T, P, \{N_i\}) = 0 \quad (4.20)$$

In the meantime, we can derive an expression for μ_i using the total partition functions $Z = \prod_i \frac{z_i}{N_i!}$. The Gibbs free energy is given by: $G = E_{elec} - k_B T \ln Z$ where $E_{elec} \equiv \sum_i N_i E_i$ stands for the electronic term of the total internal energy. Using the Stirling approximation, this equation can be developed:

$$G = \sum_i N_i E_i - k_B T \left\{ - (N_i \ln N_i - N_i) + N_i \ln z_i + \ln Z' \right\} \quad (4.21)$$

Then, the chemical potential is related to the Gibbs free energy through: $\mu_i = \frac{\partial G}{\partial N_i}$.

$$\mu_i = E_i - k_B T (\ln z_i - \ln N_i) \quad (4.22)$$

From the expression of z_i and more specifically the expression of z_{trans} , one can extract the volume and include the volumetric concentration in the equation:

$$\mu_i = E_i - k_B T \left\{ \ln \left(\frac{(2\pi m_i k_B T)^{3/2}}{h^3} z_{vib,i} z_{rot,i} \right) - \ln C_i \right\} \quad (4.23)$$

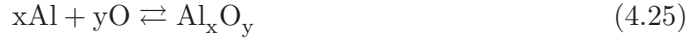
The equilibrium condition given by the equation 4.20 can, now, be written in terms of concentrations:

$$\boxed{K(T) \equiv \prod_{i=1}^n C_i^{\nu_i} = \prod_{i=1}^n \left(\frac{(2\pi m_i k_B T)^{3/2}}{h^3} z_{vib,i} z_{rot,i} \right)^{\nu_i} \times e^{-E_0/k_B T}} \quad (4.24)$$

where E_0 is the difference in electronic energy between the two sides of the chemical reactions and results from $\sum \nu_i E_i$. K is called the equilibrium constant. The equation 4.24 is the Van't Hoff law that allows one to connect the ratio in concentrations at equilibrium with the microscopic features of the molecules. The nature of the chemical equilibrium is entirely driven by the electronic, vibrational and rotational properties of the composing molecules.

The case of aluminum oxide clusters Following Patzer's model [143], we want to derive the equilibrium composition of a gas composed of aluminum and oxygen atoms

as a function of the temperature (T), the initial proportion of elements ($\lambda \equiv N_{Al}/N_O$) and the pressure (P_o). Atoms recombine into different molecules defined by a certain stoichiometry Al_xO_y . We considered a set of reactions corresponding to the formation of the $Al_xO_y^{(i)}$ molecules from an atomic gas:



i denotes the Al_xO_y isomer considered. The equilibrium condition is driven by the constant of dissociation:

$$K_{Al_xO_y^{(i)}} = \frac{P_{Al_xO_y^{(i)}} P_o^{(x+y)-1}}{P_{Al}^x P_O^y} \quad (4.26)$$

where $P_{Al_xO_y^{(i)}}$, P_{Al} and P_O are respectively the partial pressure of the $Al_xO_y^{(i)}$ molecule, the partial pressure of aluminum atoms and the partial pressure of oxygen atoms. Each $K_{Al_xO_y^{(i)}}$ is expressed using the Van't Hoff law:

$$K_{Al_xO_y^{(i)}} = \exp\left(-\frac{\Delta_r G_{Al_xO_y^{(i)}}(T, P_o)}{k_B T}\right) \quad (4.27)$$

where $\Delta_f G_{Al_xO_y^{(i)}}$ is the Gibbs free energy of formation of each $Al_xO_y^{(i)}$ and is computed from the dissociation energy, the vibrational and rotational constants. Assuming a perfect gas, we define the quantities P_{Al}^{tot} and P_O^{tot} which respectively map the total number of aluminum atoms and oxygen atoms:

$$\begin{aligned} P_{Al}^{tot} &= \sum_{x,y,i} x P_{Al_xO_y^{(i)}} \\ &= \sum_{x,y,i} x K_{Al_xO_y^{(i)}} P_{Al}^x P_O^y P_o^{1-(x+y)} \\ P_O^{tot} &= \sum_{x,y,i} y P_{Al_xO_y^{(i)}} \\ &= \sum_{x,y,i} y K_{Al_xO_y^{(i)}} P_{Al}^x P_O^y P_o^{1-(x+y)} \end{aligned} \quad (4.28)$$

The proportion of elements follows the ratio $\lambda = P_{Al}^{tot}/P_O^{tot}$. The mass conservation leads to $P_o = P_{Al}^{tot} + P_O^{tot}$. As a consequence, each (P_o, λ) pair defines the quantities P_{Al}^{tot} and P_O^{tot} . The set of equations (4.28) is then solved numerically to obtain the partial pressures P_{Al} and the P_O . Finally, the partial pressures of all $Al_xO_y^{(i)}$ molecules composing the system are calculated from the equation (4.26).

We improved the Patzer's model by taking into account the temperature and pressure dependences of $\Delta_r G_{Al_xO_y^{(i)}}$ and the contribution of all isomers for each molecules.

4.3.2 Application for the ablation in air

In **air**, the ratio in density between aluminum monoxide molecules and aluminum atoms was measured [See figure 4.5]. The electronic temperature measured in figure 3.16 was used to calculate the proportionality factor using equation 3.29 assuming $T_{elec} = T_{vib}$ and the ratio was then corrected using equation 3.14 [See figure 4.5].

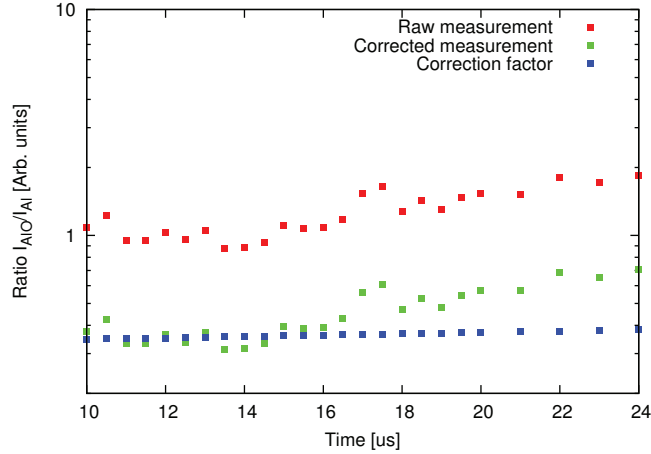


FIGURE 4.5: Influence of the electronic temperature for the measured ratio between aluminum monoxide and aluminum atoms.

In the meantime, we had measured previously the rotational temperature which can be considered as a probe of the kinetic temperature of atoms [See section 3.3.2]. As a consequence, the temperature used in the Van't Hoff law corresponds to the rotational temperature. Finally, we can transfer the temporal evolution of the density ratio of aluminum monoxide to aluminum atoms to a temperature evolution and compare it to the result of the model described in the previous section.

In figure 4.6, the experimental measurements from $10 \mu\text{s}$ to $24 \mu\text{s}$ are compared with these calculations using the Pearson's cumulative test statistic ($\chi^2 = \sum \frac{(X_{th} - X_{exp})^2}{X_{exp}}$). We can see a valley of highest likelihood obtained for P from 2 bars to 10 bars and λ from 0.01 to 1. In figure 4.7, corrected experimental measurements are plotted along with several theoretical curves in order to assess the quality of agreement between experimental measurements and theoretical calculations. The center of the valley shows that there is no unique value that can match the experimental data. Yet, the smallest χ^2 is obtained for $P=4$ and $\lambda = 0.6$. This result is promising since the expected value should be $\lambda = 2/3$ for alumina target. This agreement between purely theoretical calculation and experiment data relies on the idea that the plasma is not really in an out-of-equilibrium condition. This means that the chemical reactions that turn aluminum and oxygen atoms

into clusters are so rapid that the chemical composition is only driven by temperature variations.

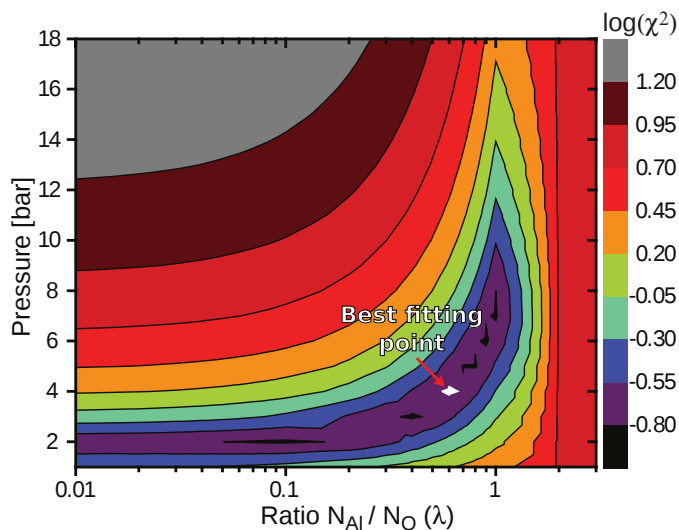


FIGURE 4.6: Likelihood between the corrected experimental ratio N_{AlO}/N_{Al} measured from $10 \mu\text{s}$ to $24 \mu\text{s}$ and the theoretical ratio as a function of the ambient pressure P_0 and the stoichiometry λ . The white area stands for the best fitting point.

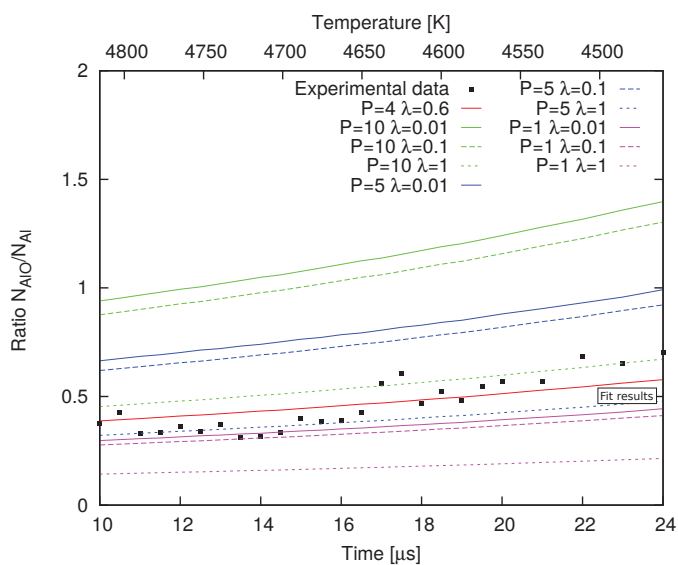


FIGURE 4.7: Comparison between the experimental measurements (black dots) and the numerical calculations for different values of λ and P at short time scale ($10 \mu\text{s}$ - $25 \mu\text{s}$).

The difficulty to obtain similar results in liquid can be explained by the lack of temporal evolution of the rotational temperature. Because the plasma quenches more rapidly, we have no ability to probe the rotational temperature as a function of the time.

4.4 An extension towards lower temperature

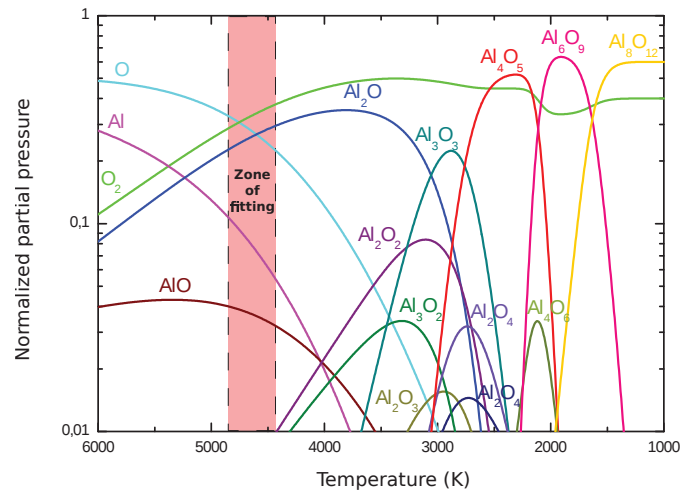


FIGURE 4.8: Evolution of the gas-phase composition from 6000 K to 1000 K considering $P=4$ bar and $\lambda=0.6$.

The previous section shows that a model based solely on computational chemistry can be used to reproduce experimental data from plasma spectroscopy. Now, the calculation is applied to larger time scales i.e. lower temperatures where diatomic molecules will react to form bigger clusters [See figure 4.8]. As expected, at high temperature ($T \gtrsim 5000$ K) i.e. short times, the gas is mainly composed of the smaller species i.e. Al, O, O_2 , AlO and Al_2O . Later, the decrease of Al_2O coincides with that of O and consequently the increase $(AlO)_n$ namely Al_2O_2 and Al_3O_3 . We emphasize that Al_2O_3 is never predominant at this stage. The stoichiometry of alumina, corresponding to Al_6O_9 and Al_8O_{12} molecules, emerges only for temperatures lower than 2000 K.

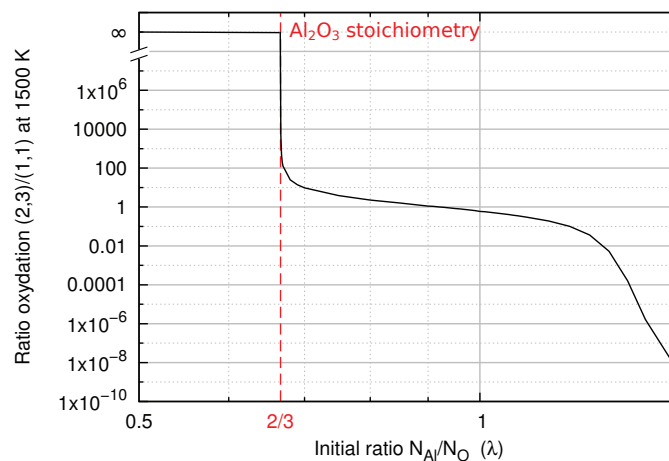


FIGURE 4.9: Ratio in composition between (2,3) and (1,1) contributions as a function of the ratio aluminum/Oxygen calculated at 1500 K.

In addition, figure 4.9 shows the ratio in composition between (2,3) and (1,1) contributions as a function of λ . The ratio is calculated at 1500 K and $(\text{Al}_2\text{O}_3)_n$ with $n \in [1 : 4]$ (resp. $(\text{AlO})_n$ with $n \in [1 : 8]$) are taken into account for (2,3) (resp. (1,1)). The values are not very relevant since they must arise from computational limitation especially for the plateau observed at low λ . Yet, below $\lambda = 2/3$, the ratio rapidly increases which means that the bulk oxide stoichiometry is favored as soon as the system is slightly saturated in oxygen. This computational result is consistent with experimental results from plasma enhanced chemical vapor deposition and pulsed laser deposition where the best crystallization for oxides is obtained when the system is loaded with oxygen [153–155]. Later, around $\lambda = 1$, a second transition seems to emerge indicating the presence of mainly suboxidized structures.

4.5 Conclusion

In summary, from atoms and molecules to nanoparticles, nucleation occurs and most theoretical works done so far cannot really describe the underlying mechanisms. Indeed, classical nucleation theory is not relevant in our case since it only illustrates the size dependence and does not take into account either stoichiometric effects or geometrical distortions. Other attempts at reaching a more complete understanding have been followed. Yet, the works usually suffer from the lack of consideration for binary systems and from explicit experimental justifications. Moreover, the nucleation in the particular context of aluminum oxide gas generated by pulsed laser ablation have certainly not been investigated so far. In this work, first principle calculations were employed to investigate aluminum oxide clusters at different stoichiometries. A systematic optimization approach was followed to obtain the stable structures. It showed singular results in comparison with the work published previously especially for the Al_2O_3 molecule [143]. Temperature-dependent evolution of the composition of a gas made of aluminum and oxygen atoms was also calculated using these molecular properties. We demonstrated that plasma spectroscopy could be used to assess the accuracy of such computational work. The best agreement between experimental results and thermochemistry calculations was obtained around $P = 4$ bars and $\lambda = 0.6$. Although for high temperature, $(\text{AlO})_n$ is the most predominant structure, the bulk aluminum oxide stoichiometry (2:3) starts to exceed the (1:1) stoichiometry for temperature lower than 2000 K. We were also able to recover that an oxygen rich gas is required for synthesizing the desired oxide stoichiometry. This result is consistent with what is commonly acknowledged for oxide synthesis. Yet, besides the equilibrium considerations, the question of whether or not these chemical reactions are kinetically favourable is not addressed here. A presence in equilibrium conditions does not mean that the molecule is necessarily going to appear. Especially, at low temperature, plasma spectroscopy can no longer provide the chemical composition since the system does not emit visible light. Nevertheless, the theoretical absorption and emission spectra can be deduced from our first-principles calculations. Laser induced fluorescence could then be performed to probe these particular molecules and assess the validity of our model for lower temperature. Finally, the high level of theory employed in our calculations precludes the addressing of bigger clusters. A complementary work could consist of using the clusters we obtained to parametrize a semi-empirical model and perform molecular dynamics simulations.

Chapter 5

Out-of-equilibrium hydrodynamics of the expanding bubble

“Measure what can be measured, and make measurable what cannot be measured.”

Galileo Galilei

Contents

5.1	The shadowgraphy technique	80
5.1.1	Experimental setup	80
5.1.2	A review of the previous works	81
5.1.3	The Rayleigh-Plesset model of the bubble dynamics	83
5.2	The bubble dynamics in three different solvents	84
5.2.1	Qualitative considerations and consequences	84
5.2.2	Thermodynamic analysis	87
5.3	Conclusion	91

As we showed in the last chapter, the model developed for the nucleation of aluminium oxide proved its reliability in air. It delivered numerous information on the reaction and the paths followed by atoms to finally become a nanoparticle. The model benefits from plasma spectroscopy since it provides precious information on the temporal evolution of the temperature. However, in liquid-phase ablation, the plasma is rapidly quenched and the formation of a bubble is observed. If we want to use the microscopic approach to nucleation introduced previously, we need to develop a method to probe the temperature inside the bubble. Another remaining interrogation concerns the composition of the bubble itself. The physical and the chemical mechanisms beneath the appearance of the bubble are still under lots of controversies. Is it a bubble made of the ablated material or is it the solvent that is evaporated? In the second case, when does the evaporation occur? In this chapter, we report on the growth and collapse of bubbles induced by laser ablation in liquid. First, bubble images were acquired using an ultra-fast camera to measure an entire dynamical evolution for each laser shot thus

overcoming reproducibility issues. Furthermore, we developed an analytical approach based on cavitation models to demonstrate that the system evolution is mostly inertial and adiabatic. We deduced quantitative thermodynamic properties inside the bubble and proved that it is mainly composed of solvent molecules whose number does not vary significantly.

5.1 The shadowgraphy technique

5.1.1 Experimental setup

For the PLAL, we used the experimental setup described in section 2.2.1. The bubble is a refracting system so visible light cannot pass through it. For the shadowgraphy measurement, the general idea is to illuminate the target surface and a fortiori the bubble. Then, the bubble refracts the light and images with dark hemispheres can be observed. For images with a nice contrast, one needs to homogeneously illuminate the bubble.

In our experiment, deionized and degassed water, pure ethanol (96% from Carlo Erba) and isopropanol (99.5% from Roth) were used as liquid solvent for PLAL. For the bubble images, a continuum argon laser ($\lambda = 541 \text{ nm}$, $P = 15 \text{ mW}$) coupled with lenses and a diffuser produces a shadow of the bubble. Images of 128×128 pixels are collected by an ultra-fast camera (Phantom v711 from Vision Research) coupled with a zoom lens system (Zoom 6000 from Navitar). The spatial resolution is equal to $30 \mu\text{m}$ per pixel. The camera framerate is 210000 frames per second.

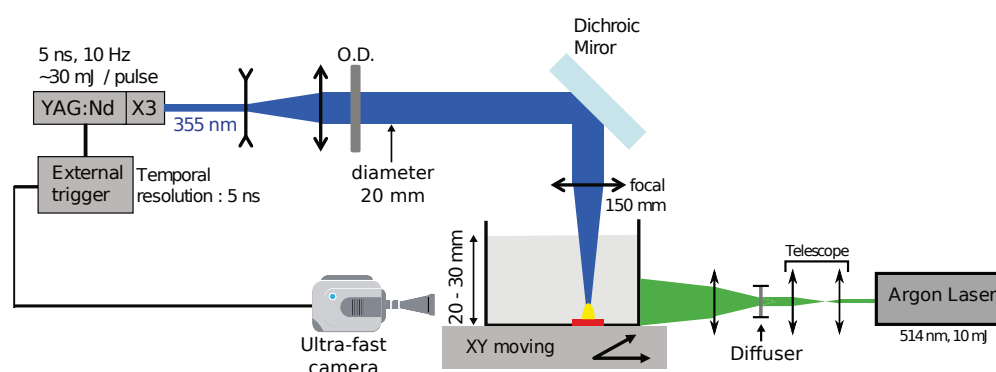


FIGURE 5.1: Sketch of the experimental setup.

5.1.2 A review of the previous works

To our knowledge, the first paper reporting the use of shadowgraphy in the context of PLAL was written by Tsuji et al. in 2004 [156]. In their article, they measured the temporal evolution of the bubble diameter after ablation of a metal target. Later, they published several other articles improving the comprehension of the physical processes underlying the bubble [157, 158]. First, a shockwave was observed. Its propagation velocity was equal to 1600 m/s [See figure 5.2 at $1.3\ \mu\text{s}$]. These results are coherent with the work of Berthe et al. who interpreted the shockwave as a result of the plasma confinement [159]. Then, from $1\ \mu\text{s}$ to $10\ \mu\text{s}$, Tsuji et al. observed a jet-shaped shadow along the laser beam [See figure 5.2]. Their original interpretation was that the jet originates from ejection of small droplets of nanoparticles. In their article published in 2007, they corrected themselves and attributed the jet to photothermal heating of the solvents since the same behaviour was observed without a solid target. They also witnessed a second shockwave after the bubble collapse that could change the formation processes [See figure 5.2 at $300\ \mu\text{s}$]. The bubble radius was also measured but no thermodynamic properties were derived.

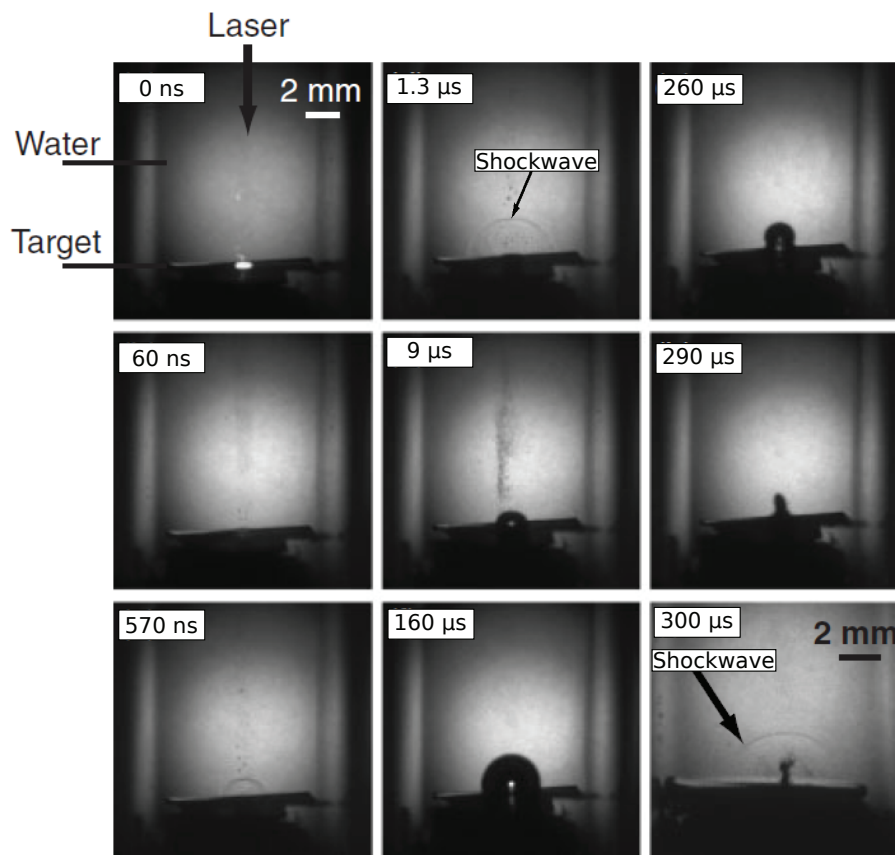


FIGURE 5.2: Shadowgraph images after laser ablation of a silver plate in water. Figures are reprinted from Tsuji et al. [158].

More recently, another study was carried out by De Giacomo et al. [160]. They observed a shockwave whose propagation velocity (1710 m/s) was similar to Tsuji et al.'s work [See figure 5.3]. In addition, the pressure induced by the shockwave was calculated using Berthe et al.'s work [159]. For the bubble dynamics, the temporal evolution of the radius was employed to obtain both temperature and pressure inside the bubble via a van der Waals model. In addition, the authors suggested that the pressure and the temperature inside the bubble are not influenced by a change in the fluence because no explicit dependence was distinguished in the van der Waals expressions. However, these equations exhibit a dependence on the bubble size and De Giacomo et al. also showed that the radius temporal evolution may change with the fluence [See figure 5.3]. Consequently, there must be a dependence of the temperature and the pressure with respect to the laser fluence.

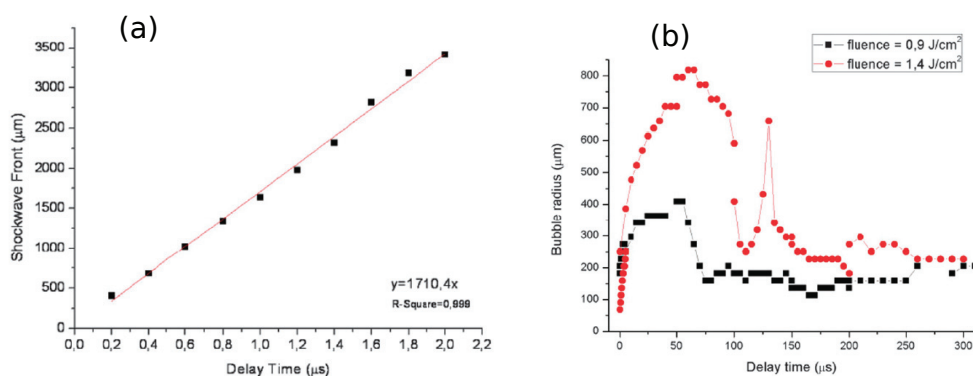


FIGURE 5.3: Temporal evolution of the shockwave front space displacement after the laser ablation of a Cu wire (a). Temporal evolution of the bubble radius after the laser ablation of an Ag wire at different laser fluences. Figures are reprinted from De Giacomo et al. [160].

In 2010, Soliman et al. published two articles on the bubble dynamics [58, 59]. In this work, a modified Rayleigh-Plesset equation which takes into account the contact angle was used to fit the temporal evolution of the bubble. From this result, the temperature and pressure were deduced using respectively the Clausius-Clapeyron relationship and Laplace's law. As a result, the calculated temperature could reach very low value (i.e. less than 10 K) which according to the authors, should explain the growth of nanoparticles. This result is somehow contradictory with the article presented previously and written by De Giacomo et al. [160].

As a result of this short review on the bubble dynamics induced by PLAL, we can see that several research groups have succeeded in measuring the temporal evolution of the bubble radius. Nevertheless, the interpretation is still controversial and no clear conclusion has been drawn yet. The bubble composition and its thermodynamic properties are still

ambiguous. In the following sections, we will use our experimental measurements and develop an improved theoretical framework to understand the bubble dynamics.

5.1.3 The Rayleigh-Plesset model of the bubble dynamics

The Rayleigh-Plesset (RP) equation aims at determining temporal evolutions of bubbles immersed in a liquid without any consideration on the bubble composition and by only adopting the liquid point of view. It is assumed that the liquid is infinite and incompressible. Far away from the bubble, the pressure and the temperature are respectively, P_l and T_0 . The bubble is considered perfectly spherical and homogeneous. Another assumption is that there is no mass transfer at the liquid-vapour interface.

First, the mass conservation equation at spherical symmetry for an incompressible fluid is given by:

$$\frac{1}{r^2} \frac{\partial}{\partial r} (\rho r^2 u_r) = 0 \quad (5.1)$$

where r is the radial position coordinate, ρ is the liquid mass density and u_r is the radial velocity of the fluid. From the integration of the equation 5.1, it emerges that:

$$u_r(r, t) = \dot{R} \frac{R^2}{r^2} \quad (5.2)$$

where R is the bubble radius and \dot{R} is the interface velocity. Then, the momentum conservation equation under spherical symmetry for incompressible fluids is given by:

$$\frac{\partial u_r}{\partial t} + u_r \frac{\partial u_r}{\partial r} = -\frac{1}{\rho} \frac{\partial P}{\partial r} + \eta \left[\frac{1}{r^2} \frac{\partial}{\partial r} \left(r^2 \frac{\partial u_r}{\partial r} \right) - \frac{2u_r}{r^2} \right] \quad (5.3)$$

where P is the pressure in the fluid located at r and η is the dynamic viscosity constant. Using 5.2, we can deduce:

$$\frac{1}{r^2} \left(2R\dot{R}^2 + R^2\ddot{R} \right) - \frac{2R^4}{r^5} \dot{R}^2 = -\frac{1}{\rho} \frac{\partial P}{\partial r} \quad (5.4)$$

By radial integration from R to ∞ , one obtains:

$$\int_R^\infty \left[\frac{1}{r^2} \left(2R\dot{R}^2 + R^2\ddot{R} \right) - \frac{2R^4}{r^5} \dot{R}^2 \right] dr = -\frac{1}{\rho} \int_{P(R)}^\infty dP \quad (5.5)$$

which reduces to:

$$R\ddot{R} + \frac{3}{2}\dot{R}^2 = \frac{P(R) - P_l}{\rho} \quad (5.6)$$

Finally, boundary condition can lead to a more explicit expression for $P(R)$ which represents the pressure at the liquid-vapour interface. The forces acting on the interface must compensate since the interface has no mass. There is one contribution from the

inner bubble and an other one from the liquid:

$$P_B - \frac{2\sigma}{R} = P(R) + \frac{4\eta\dot{R}}{R} \quad (5.7)$$

where P_B is the pressure inside the bubble considered homogeneous and varying in time. From the equations 5.6 and 5.7, we obtain the Rayleigh-Plesset equation:

$$\boxed{R\ddot{R} + \frac{3}{2}\dot{R}^2 = \frac{1}{\rho} \left[P_B(t) - P_l - \frac{2\sigma}{R} - \frac{4\eta\dot{R}}{R} \right]} \quad (5.8)$$

where R is the bubble radius, P_B is the internal pressure, P_l is the surrounding liquid pressure, γ is the fluid surface tension, ρ is the liquid mass density of the bulk and η is the dynamic viscosity of the liquid.

At this point, no consideration on the bubble is required since RP is derived by adopting the liquid point of view. We could in theory deduce the bubble pressure directly using the measurement of R .

5.2 The bubble dynamics in three different solvents

Figure 5.4 shows an example of a bubble obtained in degased water. The first image exhibits the optically active plasma and is used to set the origin for our time measurement ($t = 0 \mu s$). The bubble expands during approximately $150 \mu s$ and disappears after $300 \mu s$. Bubble radii reach a maximum typically about a few millimeters. These results are consistent with previous works [58, 59, 157, 160, 161]. After the collapse, rebounds of smaller bubbles are also observed. Figure 5.5.a shows typical temporal evolution of the bubble radius obtained after laser ablation in water, ethanol and isopropanol and figure 5.5.b shows the corresponding bubble lifetimes. The bubble radius evolution curve appears symmetric with respect to the time when it reaches its maximum. Also, the bubble dynamics is the same in ethanol and isopropanol.

5.2.1 Qualitative considerations and consequences

As demonstrated previously, the bubble dynamics can be described analytically using the Rayleigh-Plesset (RP) equation which writes:

$$R\ddot{R} + \frac{3}{2}\dot{R}^2 = \frac{1}{\rho} \left[P_B(t) - P_l - \frac{2\sigma}{R} - \frac{4\eta\dot{R}}{R} \right] \quad (5.9)$$

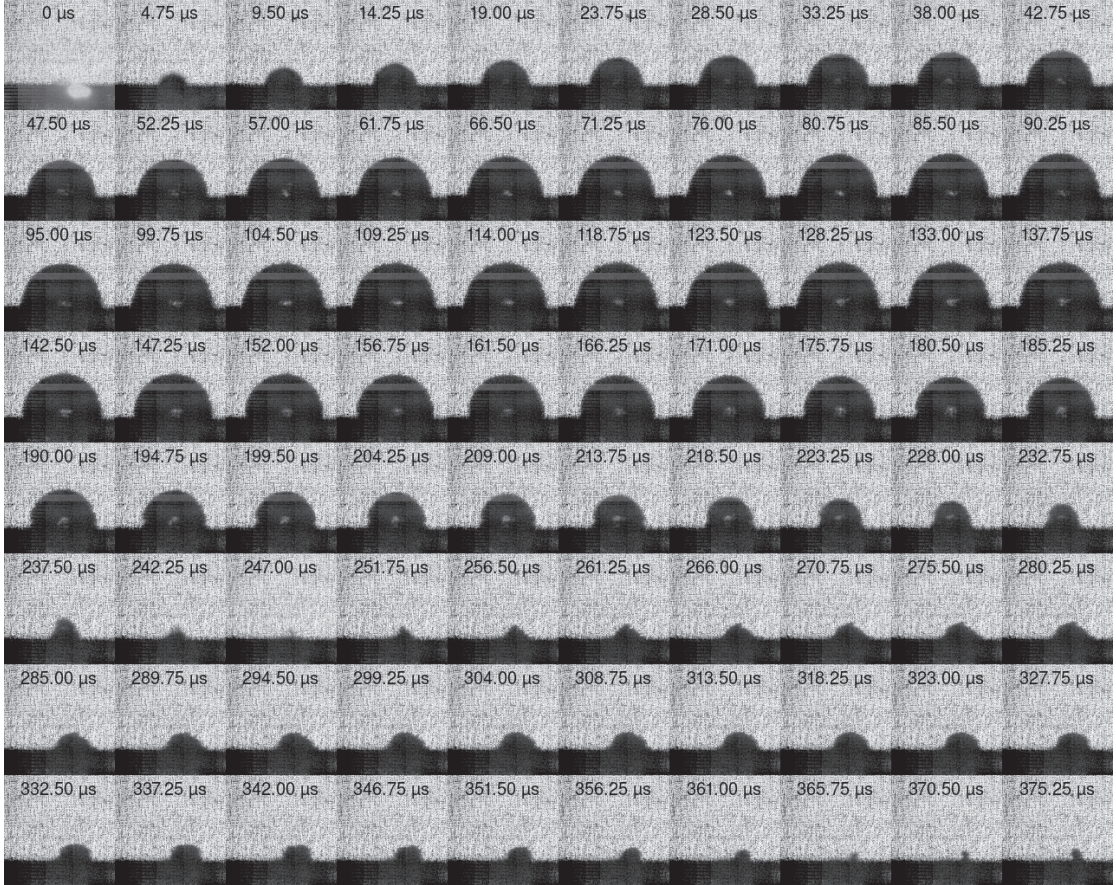


FIGURE 5.4: Shadowgraph images of an evolving bubble after laser ablation of an alumina target under degassed water. Each image is 128×128 px² representing 3.78×3.78 mm². The numbers stand for the delays between laser shots and image measurements.

where R is the bubble radius, P_B is the internal pressure, P_l is the surrounding liquid pressure, σ is the fluid surface tension, ρ is the liquid mass density of the bulk and η is the dynamic viscosity of the liquid. From here, the relative contribution of each term can be estimated. The Reynolds number which compares the inertial contribution to the viscosity is equal to $\mathcal{Re} = \rho \dot{R} R / \eta \simeq 3 \times 10^3$ using the parameters of liquid water $\rho = 10^3$ kg/m³, $\eta = 10^{-3}$ Pa·s, and for the typical length and time scales, $R \simeq 10^{-3}$ m and $t = 300$ μs. Hence, viscous terms in the Rayleigh-Plesset equation can be neglected. Moreover, the contribution of surface tension terms can be compared to inertial terms using the Weber number $We = \rho \dot{R}^2 R / \sigma \simeq 300$ which allows to discard the surface tension term as well. These qualitative considerations suggest that the chemical composition of the liquid-vapor interface and the motion of the three phase contact interface do not play a major role in the bubble dynamics. Consequently, the Rayleigh-Plesset equation is driven by the inertial terms and can be reduced as:

$$\rho(R\ddot{R} + \frac{3}{2}\dot{R}^2) = P_B(t) - P_l \quad (5.10)$$

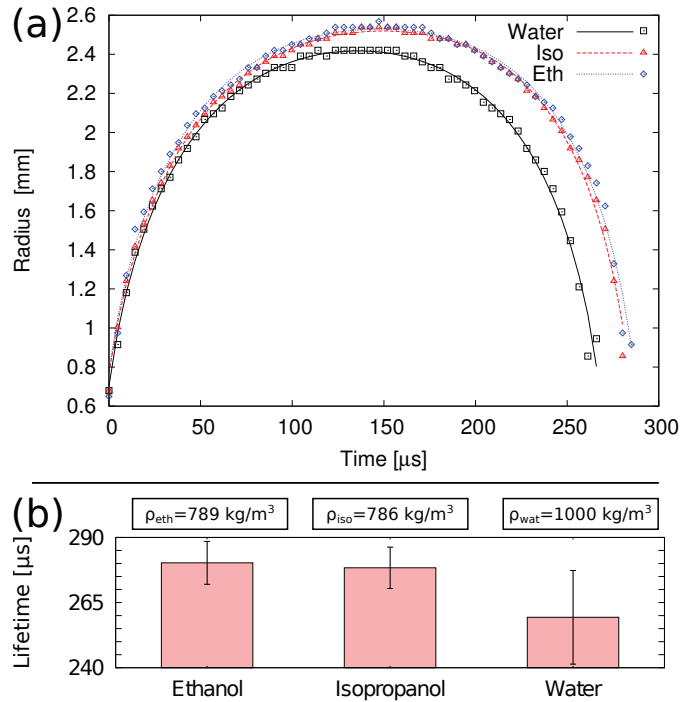


FIGURE 5.5: (a) Temporal evolution of bubble radius obtained after laser ablation in three different solvents. The solid lines stand for the corresponding polynomial regression. (b) Bubble lifetime for different solvents calculated as the average for 5 shots.

The surface effects around the bubble borders and on the target surface do not significantly contribute to the bubble dynamics. In figure 5.5.b, since the density of ethanol and isopropanol are very similar, their lifetimes are the same while shorter lifetime in water is observed due to its larger density.

Moreover, we can estimate the time scales to observe the first thermal exchanges. Energy transfer between the gas and the liquid originates mostly from convection and can be estimated using the heat transfer coefficient, h , which is at most $100 \text{ W}\cdot\text{m}^{-2}\cdot\text{K}^{-1}$ [162]. Then, the transferred power through the hemi-sphere is estimated by:

$$P_C = h\Delta T(\pi R^2 + 2\pi R^2) = 0.24 W \quad (5.11)$$

where ΔT is the difference in temperature between the bubble and the liquid which is less than 3000 K (See section 3.2.3). After $300 \mu\text{s}$, only $72 \mu\text{J}$ is evacuated which has to be compared with the 35 mJ of the laser pulse. The estimated energy transfer is weak and the process is supposed to remain adiabatic during the whole bubble lifetime. This comparison also shows that solvent evaporation can only occur during the plasma phase since no heat can be transferred to induce liquid-vapor phase transitions afterward. This deduction confirms what Tamura et al. experimentally demonstrated [163]. Indeed, they

observed that the bubble is already existing simultaneously to the plasma after 600ns. This result was interpreted as a rapid solvent evaporation.

A direct calculation of the bubble pressure using RP equation leads to singular results due to the difficulty in calculating \ddot{R} from R . Here, we will derive the bubble pressure P_B by integrating the RP equation with respect to time. Considering an adiabatic evolution and a bubble as a closed ideal system i.e. no mass transfer, the Laplace's law ($PV^\gamma = \text{const}$) can be used:

$$P_B(t) = \frac{C_0}{R^{3\gamma}} \quad (5.12)$$

where γ is the heat capacity ratio and C_0 is a constant. Moreover, the inertial terms of the RP equation can be rewritten as:

$$(R\ddot{R} + \frac{3}{2}\dot{R}^2) = \frac{1}{2R^2\dot{R}} \frac{d(R^3\dot{R}^2)}{dt} \quad (5.13)$$

Equations 5.10, 5.12 and 5.13 together lead to:

$$\frac{d}{dt} (R^3\dot{R}^2) = \frac{2}{\rho} (C_0R^{2-3\gamma}\dot{R} - P_lR^2\dot{R}) \quad (5.14)$$

Integrating the equation 5.14 leads to:

$$R^3\dot{R}^2 = \frac{2}{\rho} \left(\frac{1}{1-\gamma} \frac{C_0}{R^{3\gamma}} R^3 - P_lR^3 \right) + C_1 \quad (5.15)$$

where C_1 is the integration constant. We can substitute back $\frac{C_0}{R^{3\gamma}}$ by P_B and divide by R^3 :

$$\dot{R}^2 = \frac{2}{3\rho} \left(\frac{1}{1-\gamma} P_B - P_l \right) + \frac{C_1}{R^3} \quad (5.16)$$

The integration constant C_1 is obtained at the bubble maximum where $\dot{R} = 0$ by using the equation 5.10:

$$C_1 = \frac{2R_{max}^3}{3(\gamma-1)} \left(\frac{\gamma P_l}{\rho} + R_{max}\ddot{R}_{max} \right) \quad (5.17)$$

and the bubble pressure $P_B(t)$ is derived:

$$P_B(t) = (1-\gamma) \left\{ P_l + \frac{3\rho}{2} \left(\dot{R}^2 - \frac{C_1}{R^3} \right) \right\} \quad (5.18)$$

5.2.2 Thermodynamic analysis

Practically, the most accurate extrapolation of R is obtained when R is extracted numerically by fitting R^2 with a 5th order polynomial regression [See figure 5.5]. \dot{R} and \ddot{R} are then calculated by mathematical differentiation. R^3 is obtained from a direct

fit. P_l was set equal to 2 atm to avoid negative temperature issues. This overpressure can be attributed to a localized gradient of liquid density as reported by Lombard et al. [164] and does not affect the following considerations since similar results are obtained for P_l ranging from 2 atm to 5 atm. Figure 5.6 shows typical temporal evolution of the calculated bubble pressure obtained after laser ablation in water, ethanol and isopropanol. The pressure levels are consistent with those obtained by De Giacomo et al [160]. Yet, our approach provides a more accurate estimation than their hard core van der Waals static model since we also considered the dynamical behavior i.e. \dot{R} and \ddot{R} in the pressure determination. Moreover, our experiments lead to a more refined temporal evolution without any shot-to-shot reproducibility issues.

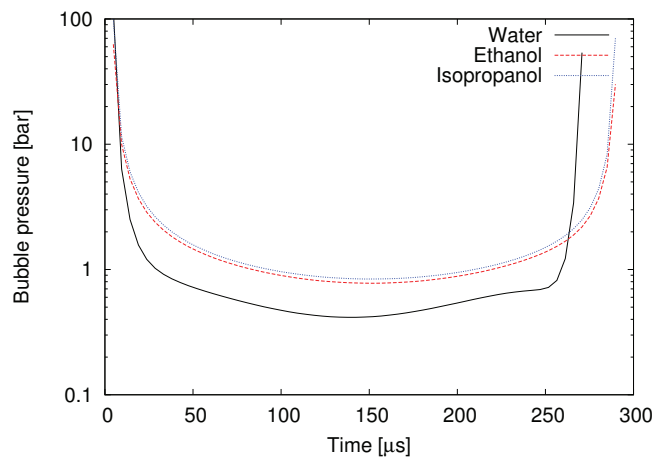


FIGURE 5.6: Bubble pressure obtained after laser ablation in three different solvents.

To assess the adiabatic and closed ideal system assumptions, $\ln P$ is plotted as a function of $\ln V$ in figure 5.7.a. We derived the adiabatic constant γ after a linear regression of $\ln P = \ln C_0 - \gamma \ln R^3$ considering the full evolution, the growth as well as the collapse for the three solvents [See figure 5.7.b]. A slight asymmetry is observed for water. This has been noticed for all the studied bubbles but, it was only limited to a narrow time interval. We found a remarkable agreement with tabulated γ in the three solvents regardless of the fitting interval i.e. full evolution, growth and collapse and regardless of the liquid pressure P_l going from 2 atm to 5 atm. These outcomes validate our original assumptions i.e. **(i)** the evolution is inertial, **(ii)** no thermal energy is transferred from the vapor to the liquid **(iii)** the number of particles inside the bubble does not vary significantly. This conclusion is supported by comparing values of γ during the growth and the collapse. We obtained values that are very similar which demonstrates that the evolution is symmetric and neither exchange of energy nor condensation or evaporation arise during the bubble evolution.

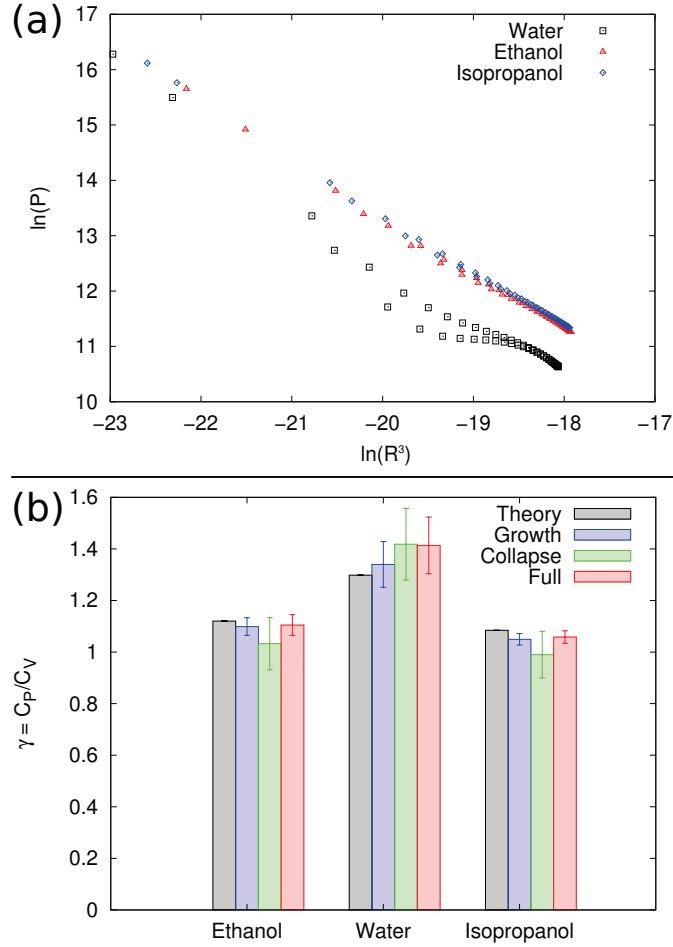


FIGURE 5.7: (a) Evolution of the pressure P_B in the vapour bubble as a function of the instantaneous volume R^3 obtained in degassed water, ethanol and isopropanol. (b) Comparison between the theoretical adiabatic constants γ and those obtained after linear regression of $\ln P = \ln C_0 - \gamma \ln R^3$ using the full evolution, only the growth and only the collapse in water, ethanol and isopropanol. The error bars correspond to standard deviation obtained for 40 bubbles.

The instantaneous temperature, $T_B(t)$, can be deduced from the Laplace's law:

$$\frac{T_B(t)}{T_0} = \left(\frac{P}{P_0} \right)^{\frac{\gamma-1}{\gamma}} \quad (5.19)$$

Figure 5.8 shows typical temporal evolution of the bubble temperature obtained after laser ablation in three solvents. The bubble in water is colder than in ethanol and isopropanol. Hence, we expect the chemical reactions to be slower and since the bubble lifetime is also smaller, smaller particles should be obtained in degassed water.

In section 3.2.3, the plasma temperature was measured as equal to $3400 \text{ K} \pm 340 \text{ K}$ at $2 \mu\text{s}$ using plasma spectroscopy and under the same experimental conditions as in this study. Assuming an ideal gas law, N , the number of particles inside the bubble can be obtained. We found approximately 9×10^{16} atoms. This value is an underestimation

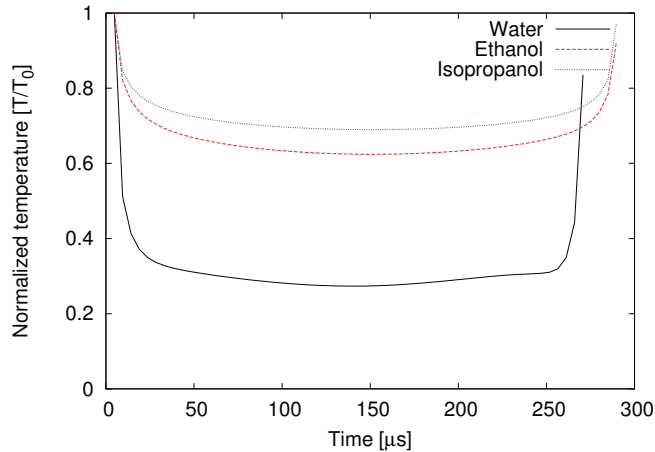


FIGURE 5.8: Rescaled temperature $T_B(t)/T_0$ obtained after laser ablation in three different solvents.

since the temperature measured with plasma spectroscopy was obtained at $2\ \mu\text{s}$ and the first point used in the calculation was at $9.5\ \mu\text{s}$. The system could easily be colder leading to higher values of N . We also estimate the number of atoms ablated by the laser to be equal to $7 \times 10^{15} \pm 70\%$ atoms following crater measurements described in section 2.2.1. The difference between the amount of particles in the bubble and the ablated material is at least of one order of magnitude. The bubble is therefore mostly composed of solvent molecules. Moreover, if there were an important amount of ablated species inside the bubble, they would suffer from chemical reactions that should induce a change in the number of moles. We already showed that the number of particles does not change during the evolution thus supporting the minor contribution of ablated matter.

Finally, since secondary bubbles generated by the rebounds are smaller than the first bubble, condensation probably occurs at the end of the collapse during short time scales. The condensation can easily originate from heterogeneous nucleation on the cold target surface or on synthesized nanoparticles. We do not address this aspect in this contribution.

5.3 Conclusion

In summary, we measured experimentally the temporal evolution of bubble radii resulting from laser ablation in liquid. The use of an ultra-fast camera provides one time-resolved measurement per bubble thus avoiding reproducibility issues. Using Rayleigh-Plesset equation, we first demonstrated that the evolution is driven by inertia implying that neither viscosity nor surface tension effects can affect the bubble dynamics. Thermal exchanges are discussed in the context of interfacial heat conduction mechanisms to demonstrate the adiabaticity of the system. The RP equation can then be solved to deduce the bubble pressure. Probing the calculated pressure as a function of the bubble volume, we obtained a power law dependence and emphasized that the number of particles in the vapor does not fluctuate. Consequently, we derive the number of particles and conclude that the bubble is essentially formed of solvent particles whose quantity does not vary significantly.

Our results are critical for nano-material elaboration because they show that the solvent plays a major role during the whole bubble lifetime. It explains for instance the striking experiment where carbon nitrides have been synthesized after carbon ablation in ammonia [28, 29]. It also explains why numerous oxides have been obtained when ablating pure metal targets [34–37] in water. Moreover, very small nanoparticles ($\lesssim 5$ nm) have been synthesized using complexing agents and this result may be interpreted as the entrance of the complexing agents right inside the bubble [21]. Moreover, if condensation occurs on the nanoparticle surface, it can also freeze the nanoparticle growth and explains why these small size distributions can be obtained.

Conclusion and perspectives

THIS manuscript was dedicated to the comprehension of the growth processes occurring in pulsed laser ablation in liquid (PLAL). We combined experimental techniques with analytical and numerical methods to investigate how the ablated species can recombine to form nanoparticles.

On the synthesis of aluminum oxide nanoparticles As a starting point, we worked on the synthesis of $\text{Al}_2\text{O}_3:\text{Cr}$. The ultra-violet nanosecond laser allowed us to generate γ - Al_2O_3 nanoparticles. This result confirms previous studies on the stability at nanometer length scales. Indeed, McHale et al. demonstrated that γ is the most stable crystallographic phase due to the emergence of surface energies [60, 61]. Then, we showed that using an infrared picosecond laser, α - Al_2O_3 nanoparticles can be obtained. This result supports the idea that PLAL allows one to reach specific applications hardly addressed elsewhere. The α - Al_2O_3 fluorescence under ultra-violet excitation depends on the local pressure in bulk. The nanoparticles we synthesized exhibit the same properties in the fluorescence emission under pressure. This similarity obtained at nanoscale for the pressure is adjacent to the additional Laplace's pressure usually included to understand surface effects. Our work will be pursued in this context to understand the contribution of surface effects to hydrostatic pressure. In addition, we studied the effect of complexing agents on the size distribution and observed a shift towards smaller nanoparticles. Although the luminescence was also recognized, we still need to characterize the pressure dependence for these very small nanoparticles. Yet, these outcomes are already promising for future applications on pressure sensing at nanoscale.

Towards the understanding of the growth processes The previous results on the synthesis of nanoparticles motivated the following work on the understanding of the growth processes. Indeed, varying the laser wavelength and the pulse duration changed drastically the results of the synthesis. Furthermore, the addition of complexing agents reduced the size distribution and stabilized the colloidal solution. Consequently, enhancing the PLAL performances requires to understand the complexity of the out-of-equilibrium processes involving multiple length and time scales. The investigation of these mechanisms was the subject of the three other chapters of this manuscript.

Underwater plasma spectroscopy and its fundamental consequences First, the laser interacts with the bulk target creating a hot and dense plasma. The excited species emit light whose spectral characterization allows us to access thermodynamic properties of the plasma. The technique is called plasma spectroscopy and is frequently employed in air for analytical chemistry. In water, fundamental difficulties arise from the liquid confinement thus preventing from observing ions and atoms. We demonstrated that the plasma could still be studied using atomic lines of aluminum and rovibrational lines of aluminum monoxide. Hence, we measured the electronic density by observing the Stark effect on the aluminum lines. Our results showed that while self-absorption may also be recognized in water, the electronic density is one order of magnitude higher than what is expected in air. For the temperature, since ions are not observed, we used the rotational lines of aluminum monoxide ($\Delta\nu = 0$). We built a numerical code to fit the experimental data and obtained a temperature of 3400 ± 340 K after $2 \mu\text{s}$. Then, we probed the ratio in intensity between aluminum and aluminum monoxide lines to monitor quantitatively the oxidation of aluminum into aluminum monoxide.

This work on the use of diatomic molecules stimulated a work on the temperature equilibration inside a molecular plasma. We then demonstrated that no equality was necessarily present between electronic temperature and rotational temperature. This difference in temperature could be attributed to a difference in the spatial distribution but also to a difference in the collisional processes which induce the energy level excitation. Indeed, electronic levels are mostly excited by collisions with electrons. Yet, for the rotational levels, an additional collision mechanism is required, the collision between heavy species. There are two collisional processes thus two different temperatures.

Moreover, the role of chemical reactions on temperature equilibration was raised in two other investigations. We, first, measured a difference between rotational and vibrational temperatures when working with aluminum monoxide during the first time scales. We consider this behavior as a result of the energy repartition following the aluminum monoxide formation. Indeed, the chemical reaction is exothermic and the remaining energy is not necessarily spread evenly between rotational and vibrational energy levels. This qualitative approach ought to be confirmed with future molecular dynamics simulations. Then, we compared the rotational temperature of aluminum monoxide with that of titanium monoxide obtained after the ablation of a composite made of aluminum oxide (75%) and titanium oxide (25%). The two temperatures are different and the rotational temperature of titanium monoxide seems to increase while matching that of aluminum monoxide. Additional work should be done to investigate the spatial distribution of these two diatomic molecules and their reaction enthalpy.

Atomistic mechanisms for the nucleation of aluminium oxide nanoparticles When the plasma is no longer active, the atoms and molecules recombine to form nanoparticles. This process begins with nucleation and is followed by growth. Although nucleation of nanoparticles concerns a wide range of applications, its mechanisms are hardly understood on the atomistic level. Very little is known, for instance, about the transient nature of the nucleation core, especially since its geometrical structure and stoichiometry do not always perfectly match that of the final structure. Here, we presented a fully microscopic approach based on a first principle study of aluminum oxide clusters. We calculated stable structures of Al_xO_y and the associated thermodynamic properties. From these data, the chemical composition of a gas made of aluminum and oxygen atoms was calculated as a function of the temperature, pressure, and aluminum to oxygen ratio. After showing the accuracy of this approach to reproduce experimental results obtained with plasma spectroscopy, we extended the calculation to lower temperature and followed the birth of alumina first bricks. On a broader perspective, this work may be extended to bigger particles. However, first principle calculations are time-consuming and it would not be realistic to address bigger particles with our method. Yet, our calculations may serve for a parametrization of a semi-empirical potential e.g. PM3. Granted with this new analytical atomic interaction, molecular dynamics could be used to investigate bigger particles.

Dynamical study of bubble expansion following laser ablation in liquid To investigate further the temperature behavior inside the bubble and to complement our nucleation work, we investigated the bubble dynamics by combining analytical methods with ultra fast experimental observations. We measured the entire bubble kinetic evolution using an ultra-fast camera thus avoiding reproducibility issues unlike experiments where the bubble kinetics is constructed from multiple laser shots. This study is reported in three different liquid solvents enabling us to compare the dynamics for different liquid properties. Moreover, we developed a quantitative thermodynamic analysis based on cavitation models showing that **(i)** the system is essentially driven by inertia, **(ii)** the evolution is adiabatic and **(iii)** the bubble is mainly composed not of the ablated material but of evaporated solvent whose quantity does not vary during the bubble lifetime. This approach allows us to clarify the complexity involved in PLAL. However, additional work may consist on the study of the rebounds. After the bubble collapse, thermal effects may arise and affect the secondary bubbles size and periodicity. The bubble generated after focusing the laser directly in the liquid without target can also be investigated because it may represent an example of homogeneous nucleation driven by temperature effects.

General perspectives

As outlined in the previous paragraphs, this PhD work tackled the problem of understanding the growth processes occurring in pulsed laser ablation in liquid using various methods. On the one hand, we went from short time scales to longer ones by working on plasma thermodynamics and bubble kinetics respectively. On the other hand, we went from small length scales to longer ones by studying the atomic mechanisms of nucleation and the synthesized nanoparticles. Conceptually, the core of the complexity presented by PLAL relies mostly on the idea that free atoms should eventually merge to form nanoparticles. This dynamical behavior is a phase transition from gas to crystal covering nucleation and growth. Our work may be applied for other synthesis methods e.g. pulsed laser deposition, plasma-enhanced chemical vapor deposition or co-precipitation where nucleation and growth also occur. Prompted by this three-years work, I believe that the dynamical study of phase transitions in general is a cornerstone in numerous research fields. For instance, cancer expansion in human body [165], galaxy formation [166], population accretion in cities [167] and epidemic spreading [168, 169] are different phenomena that could all be regarded as phase transitions and whose conceptual modeling may be analogous [170, 171]. Accordingly, studies of nucleation, clustering and growth are crucial for fundamental comprehension but also for concrete applications.

Bibliography

- [1] T. Maiman, Stimulated optical radiation in ruby, *Nature* 187 (4736) (1960) 493–494. doi:10.1038/187493a0.
- [2] A. Morales, C. Lieber, A laser ablation method for the synthesis of crystalline semiconductor nanowires, *Science* 279 (5348) (1998) 208–211. doi:10.1126/science.279.5348.208.
- [3] R. Srinivasan, B. Braren, Ultraviolet-laser ablation of organic polymers, *Chem. Rev.* 89 (6) (1989) 1303–1316. doi:10.1021/cr00096a003.
- [4] I. Herman, Laser-assisted deposition of thin films from gas-phase and surface-adsorbed molecules, *Chem. Rev.* 89 (6) (1989) 1323–1357. doi:10.1021/cr00096a005.
- [5] D. Lowndes, D. Geohegan, A. Puretzky, D. Norton, C. Rouleau, Synthesis of novel thin-film materials by pulsed laser deposition, *Science* 273 (5277) (1996) 898–903. doi:10.1126/science.273.5277.898.
- [6] Y. Lida, A. Tsuge, Y. Uwanimo, H. Morikawa, T. Ishizuka, Laser ablation in a liquid-medium as a technique for solid sampling, *J. Anal. At. Spectrom.* 6 (7) (1991) 541–544. doi:10.1039/JA9910600541.
- [7] S. Barcikowski, G. Compagnini, Advanced nanoparticle generation and excitation by lasers in liquids, *Phys. Chem. Chem. Phys.* 15 (9) (2013) 3022–3026. doi:10.1039/c2cp90132c.
- [8] B. Cushing, V. Kolesnichenko, C. O'Connor, Recent advances in the liquid-phase syntheses of inorganic nanoparticles, *Chem. Rev.* 104 (9) (2004) 3893–3946. doi:10.1021/cr030027b.
- [9] C. Phipps, *Laser Ablation and Its Applications*, Springer Series in Optical Sciences, Springer, 2007. doi:10.1007/978-0-387-30453-3.
- [10] E. Gaffet, O. Tillement, Mechanochemistry and mechanical activation, *Ann. Chim.-Sci. Mat.* 22 (6) (1997) 417–422.

- [11] L. Madler, H. Kammler, R. Mueller, S. Pratsinis, Controlled synthesis of nanostructured particles by flame spray pyrolysis, *J. Aerosol. Sci.* 33 (2) (2002) 369–389. doi:10.1016/S0021-8502(01)00159-8.
- [12] A. J. Groehn, S. E. Pratsinis, A. Sanchez-Ferrer, R. Mezzenga, K. Wegner, Scale-up of nanoparticle synthesis by flame spray pyrolysis: The high-temperature particle residence time, *Ind. Eng. Chem. Res.* 53 (26) (2014) 10734–10742. doi:10.1021/ie501709s.
- [13] C. L. Sajti, R. Sattari, B. N. Chichkov, S. Barcikowski, Gram scale synthesis of pure ceramic nanoparticles by laser ablation in liquid, *J. Phys. Chem. C* 114 (6) (2010) 2421–2427. doi:10.1021/jp906960g.
- [14] F. Mafune, J. Kohno, Y. Takeda, T. Kondow, Formation of gold nanonetworks and small gold nanoparticles by irradiation of intense pulsed laser onto gold nanoparticles, *J. Phys. Chem. B* 107 (46) (2003) 12589–12596. doi:10.1021/jp0301731.
- [15] F. Mafune, J. Kohno, Y. Takeda, T. Kondow, Formation of stable platinum nanoparticles by laser ablation in water, *J. Phys. Chem. B* 107 (18) (2003) 4218–4223. doi:10.1021/jp021580k.
- [16] A. Simakin, V. Voronov, G. Shafeev, R. Brayner, F. Bozon-Verduraz, Nanodisks of au and ag produced by laser ablation in liquid environment, *Chem. Phys. Lett.* 348 (3-4) (2001) 182–186. doi:10.1016/S0009-2614(01)01136-8.
- [17] H. Zeng, W. Cai, Y. Li, J. Hu, P. Liu, Composition structural evolution and optical properties of ZnO/Zn nanoparticles by laser ablation in liquid media, *J. Phys. Chem. B* 109 (39) (2005) 18260–18266. doi:10.1021/jp052258n.
- [18] W. O. Zhang, Y. Zhang, J. Y. Tang, Y. Zhang, L. H. Wang, Q. D. Ling, Study on preparation and optic properties of nano europium oxide-ethanol sol by pulsed laser ablation, *Thin Solid Films* 417 (1-2) (2002) 43–46. doi:10.1016/S0040-6090(02)00640-5.
- [19] W. W. An, J. P. Miao, Z. G. Zhang, Effect of laser intensity on synthesis of solid solution γ -(CeTbO₃) in the liquid induced by ND : YAG laser irradiation, *Chem. Phys. Lett.* 423 (4-6) (2006) 386–389. doi:10.1016/j.cplett.2006.04.018.
- [20] G. Ledoux, D. Amans, C. Dujardin, K. Masenelli-Varlot, Facile and rapid synthesis of highly luminescent nanoparticles via pulsed laser ablation in liquid, *Nanotechnology* 20 (44) (2009) 445605. doi:10.1088/0957-4484/20/44/445605.
- [21] D. Amans, C. Malaterre, M. Diouf, C. Mancini, F. Chaput, G. Ledoux, G. Breton, Y. Guillin, C. Dujardin, K. Masenelli-Varlot, P. Perriat, Synthesis of oxide

- nanoparticles by pulsed laser ablation in liquids containing a complexing molecule: Impact on size distributions and prepared phases, *J. Phys. Chem. C* 115 (12) (2011) 5131–5139. doi:10.1021/jp109387e.
- [22] Y. Onodera, T. Nunokawa, O. Odawara, H. Wada, Upconversion properties of $Y_2O_3 : Er, Yb$ nanoparticles prepared by laser ablation in water, *J. Lumin.* 137 (0) (2013) 220–224. doi:10.1016/j.jlumin.2012.12.033.
- [23] D. Amans, A.-C. Chenus, G. Ledoux, C. Dujardin, C. Reynaud, O. Sublemontier, K. Masenelli-Varlot, O. Guillois, Nanodiamond synthesis by pulsed laser ablation in liquids, *Diam. Relat. Mat.* 18 (2-3) (2009) 177–180. doi:10.1016/j.diamond.2008.10.035.
- [24] J. Wang, C. Zhang, X. Zhong, G. Yang, Cubic and hexagonal structures of diamond nanocrystals formed upon pulsed laser induced liquid-solid interfacial reaction, *Chem. Phys. Lett.* 361 (1-2) (2002) 86–90. doi:10.1016/S0009-2614(02)00871-0.
- [25] P. Wagener, A. Schwenke, S. Barcikowski, How citrate ligands affect nanoparticle adsorption to microparticle supports, *Langmuir* 28 (14) (2012) 6132–6140. doi:10.1021/la204839m.
- [26] M. C. Duran, S. Willenbrock, A. Barchanski, J.-M. V. Mueller, A. Maiolini, J. T. Soller, S. Barcikowski, I. Nolte, K. Feige, H. M. Escobar, Comparison of nanoparticle-mediated transfection methods for dna expression plasmids: efficiency and cytotoxicity, *J. Nanobiotechnol.* 9 (2011) 47. doi:10.1186/1477-3155-9-47.
- [27] S. Petersen, S. Barcikowski, Conjugation efficiency of laser-based bioconjugation of gold nanoparticles with nucleic acids, *J. Phys. Chem. C* 113 (46) (2009) 19830–19835. doi:10.1021/jp905962f.
- [28] L. Yang, P. W. May, L. Yin, R. Brown, T. B. Scott, Direct growth of highly organized crystalline carbon nitride from liquid-phase pulsed laser ablation, *Chem. Mat.* 18 (21) (2006) 5058–5064. doi:10.1021/cm061485e.
- [29] L. Yang, P. W. May, L. Yin, J. A. Smith, K. N. Rosser, Ultra fine carbon nitride nanocrystals synthesized by laser ablation in liquid solution, *J. Nanopart. Res.* 9 (6) (2007) 1181–1185. doi:10.1007/s11051-006-9192-4.
- [30] H. Zeng, X.-W. Du, S. C. Singh, S. A. Kulinich, S. Yang, J. He, W. Cai, Nanomaterials via laser ablation/irradiation in liquid: A review, *Adv. Funct. Mater.* 22 (7) (2012) 1333–1353. doi:10.1002/adfm.201102295.

- [31] Z. Yan, D. B. Chrisey, Pulsed laser ablation in liquid for micro-/nanostucture generation, *J. Photochem. Photobiol.* 13 (3) (2012) 204–223. doi:10.1016/j.jphotochemrev.2012.04.004.
- [32] V. Amendola, M. Meneghetti, What controls the composition and the structure of nanomaterials generated by laser ablation in liquid solution?, *Phys. Chem. Chem. Phys.* 15 (9) (2013) 3027–3046. doi:10.1039/c2cp42895d.
- [33] C. H. Lin, S. Y. Chen, P. Shen, Defects, lattice correspondence, and optical properties of spinel-like Cr_3O_4 condensates by pulsed laser ablation in water, *J. Phys. Chem. C* 113 (37) (2009) 16356–16363. doi:10.1021/jp904288n.
- [34] M. Muniz-Miranda, C. Gellini, E. Giorgetti, Surface-enhanced raman scattering from copper nanoparticles obtained by laser ablation, *J. Phys. Chem. C* 115 (12) (2011) 5021–5027. doi:10.1021/jp1086027.
- [35] A. Nath, A. Khare, Size induced structural modifications in copper oxide nanoparticles synthesized via laser ablation in liquids, *J. Appl. Phys.* 110 (4) (2011) . doi:10.1063/1.3626463.
- [36] V. Amendola, P. Riello, S. Polizzi, S. Fiameni, C. Innocenti, C. Sangregorio, M. Meneghetti, Magnetic iron oxide nanoparticles with tunable size and free surface obtained via a “green” approach based on laser irradiation in water, *J. Mater. Chem.* 21 (46) (2011) 18665–18673. doi:10.1039/c1jm13680a.
- [37] J. S. Golightly, A. W. Castleman, Jr., Analysis of titanium nanoparticles created by laser irradiation under liquid environments, *J. Phys. Chem. B* 110 (40) (2006) 19979–19984. doi:10.1021/jp062123x.
- [38] T. Tsuji, K. Iryo, Y. Nishimura, M. Tsuji, Preparation of metal colloids by a laser ablation technique in solution: influence of laser wavelength on the ablation efficiency (2), *J. Photochem. Photobiol. A-Chem.* 145 (3, SI) (2001) 201–207. doi:10.1016/S1010-6030(01)00583-4.
- [39] F. Mafune, J. Kohno, Y. Takeda, T. Kondow, Dissociation and aggregation of gold nanoparticles under laser irradiation, *J. Phys. Chem. B* 105 (38) (2001) 9050–9056. doi:10.1021/jp0111620.
- [40] W. T. Nichols, T. Sasaki, N. Koshizaki, Laser ablation of a platinum target in water. 2. ablation rate and nanoparticle size distributions, *J. Appl. Phys.* 100 (11) (2006) . doi:10.1063/1.2390641.

- [41] V. Amendola, G. Rizzi, S. Polizzi, M. Meneghetti, Synthesis of gold nanoparticles by laser ablation in toluene: Quenching and recovery of the surface plasmon absorption, *J. Phys. Chem. B* 109 (49) (2005) 23125–23128. doi:10.1021/jp055783v.
- [42] A. Vogel, V. Venugopalan, Mechanisms of pulsed laser ablation of biological tissues, *Chem. Rev.* 103 (2) (2003) 577–644. doi:10.1021/cr010379n.
- [43] A. Y. Vorobyev, C. Guo, Direct femtosecond laser surface nano/microstructuring and its applications, *Laser and Photonics Reviews* 7 (3) (2013) 385–407. doi:10.1002/lpor.201200017.
- [44] S. Sundaram, E. Mazur, Inducing and probing non-thermal transitions in semiconductors using femtosecond laser pulses, *Nat. Mater.* 1 (4) (2002) 217–224. doi:10.1038/nmat767.
- [45] A. Miotello, R. Kelly, Laser-induced phase explosion: new physical problems when a condensed phase approaches the thermodynamic critical temperature, *Appl. Phys. A-Mater. Sci. Process.* 69 (S) (1999) S67–S73. doi:10.1007/s003399900296.
- [46] D. Perez, L. Lewis, Molecular-dynamics study of ablation of solids under femtosecond laser pulses, *Phys. Rev. B* 67 (18) (2003) 184102. doi:10.1103/PhysRevB.67.184102.
- [47] P. Lorazo, L. Lewis, M. Meunier, Short-pulse laser ablation of solids: From phase explosion to fragmentation, *Phys. Rev. Lett.* 91 (22) (2003) 225502. doi:10.1103/PhysRevLett.91.225502.
- [48] P. Lorazo, L. Lewis, M. Meunier, Thermodynamic pathways to melting, ablation, and solidification in absorbing solids under pulsed laser irradiation, *Phys. Rev. B* 73 (13) (2006) 134108. doi:10.1103/PhysRevB.73.134108.
- [49] D. Bäuerle, *Laser Processing and Chemistry*, Springer, 1996. doi:10.1007/978-3-642-17613-5.
- [50] K. Sugioka, M. Meunier, A. Piqué, *Laser precision microfabrication*, Springer, 2010.
- [51] S. Besner, A. V. Kabashin, M. Meunier, Fragmentation of colloidal nanoparticles by femtosecond laser-induced supercontinuum generation, *Appl. Phys. Lett.* 89 (23) (2006) . doi:10.1063/1.2402944.

- [52] F. Mafune, J. Kohno, Y. Takeda, T. Kondow, H. Sawabe, Formation and size control of silver nanoparticles by laser ablation in aqueous solution, *J. Phys. Chem. B* 104 (39) (2000) 9111–9117. doi:10.1021/jp001336y.
- [53] B. Gökce, D. D. van't Zand, A. Menéndez-Manjón, S. Barcikowski, Ripening kinetics of laser-generated plasmonic nanoparticles in different solvents, *Chem. Phys. Lett.* 626 (0) (2015) 96 – 101. doi:10.1016/j.cplett.2015.03.010.
- [54] S. Ibrahimkutty, P. Wagener, A. Menzel, A. Plech, S. Barcikowski, Nanoparticle formation in a cavitation bubble after pulsed laser ablation in liquid studied with high time resolution small angle x-ray scattering, *Appl. Phys. Lett.* 101 (10). doi:10.1063/1.4750250.
- [55] P. Wagener, S. Ibrahimkutty, A. Menzel, A. Plech, S. Barcikowski, Dynamics of silver nanoparticle formation and agglomeration inside the cavitation bubble after pulsed laser ablation in liquid, *Phys. Chem. Chem. Phys.* 15 (9) (2013) 3068–3074. doi:10.1039/c2cp42592k.
- [56] T. Sakka, S. Iwanaga, Y. Ogata, A. Matsunawa, T. Takemoto, Laser ablation at solid-liquid interfaces: An approach from optical emission spectra, *J. Chem. Phys.* 112 (19) (2000) 8645–8653. doi:10.1063/1.481465.
- [57] T. Sakka, H. Oguchi, Y. H. Ogata, Emission spectroscopy of ablation plumes in liquid for analytical purposes, Vol. 59 of *JPCS*, 2007, pp. 559–562. doi:10.1088/1742-6596/59/1/119.
- [58] W. Soliman, T. Nakano, N. Takada, K. Sasaki, Modification of rayleigh-plesset theory for reproducing dynamics of cavitation bubbles in liquid-phase laser ablation, *Jap. J. Appl. Phys.* 49 (11) (2010) . doi:10.1143/JJAP.49.116202.
- [59] W. Soliman, N. Takada, K. Sasaki, Growth processes of nanoparticles in liquid-phase laser ablation studied by laser-light scattering, *Appl. Phys. Express* 3 (3) (2010) . doi:10.1143/APEX.3.035201.
- [60] J. McHale, A. Navrotsky, A. Perrotta, Effects of increased surface area and chemisorbed H_2O on the relative stability of nanocrystalline γ -(Al_2O_3) and α -(Al_2O_3), *J. Phys. Chem. B* 101 (4) (1997) 603–613. doi:10.1021/jp9627584.
- [61] J. McHale, A. Auroux, A. Perrotta, A. Navrotsky, Surface energies and thermodynamic phase stability in nanocrystalline aluminas, *Science* 277 (5327) (1997) 788–791. doi:10.1126/science.277.5327.788.
- [62] B. Kumar, R. K. Thareja, Synthesis of aluminum oxide nanoparticles using laser ablation in liquid 7 (5) (2010) 1409–1412. doi:10.1002/pssc.200983356.

- [63] I. L. Liu, P. Shen, S. Y. Chen, H⁺- and Al²⁺-codoped Al₂O₃ nanoparticles with spinel-type related structures by pulsed laser ablation in water, *J. Phys. Chem. C* 114 (17) (2010) 7751–7757. doi:10.1021/jp1002325.
- [64] I. L. Liu, B. C. Lin, S. Y. Chen, P. Shen, NaAlO₂ and gamma-Al₂O₃ nanoparticles by pulsed laser ablation in aqueous solution, *J. Phys. Chem. C* 115 (12) (2011) 4994–5002. doi:10.1021/jp107030h.
- [65] Y. Lee, Y. Liu, C. Yeh, Formation of bayerite, gibbsite and boehmite particles by laser ablation, *Phys. Chem. Chem. Phys.* 1 (19) (1999) 4681–4686. doi:10.1039/a905178c.
- [66] R. Forman, G. Piermari, J. Barnett, S. Block, Pressure measurement made by the utilization of ruby sharp-line luminescence, *Science* 176 (4032) (1972) 284–&. doi:10.1126/science.176.4032.284.
- [67] R. Pecora, Dynamic light scattering measurement of nanometer particles in liquids, *J. Nanopart. Res.* 2 (2) (2000) 123–131. doi:10.1023/A:1010067107182.
- [68] H. Li, E. A. Ghezal, A. Nehari, G. Alombert-Goget, A. Brenier, K. Lebbou, Bubbles defects distribution in sapphire bulk crystals grown by czochralski technique, *Opt. Mater.* 35 (5) (2013) 1071–1076. doi:10.1016/j.optmat.2012.12.022.
- [69] H. Li, E. A. Ghezal, G. Alombert-Goget, G. Breton, J. M. Ingargiola, A. Brenier, K. Lebbou, Qualitative and quantitative bubbles defects analysis in undoped and Ti-doped sapphire crystals grown by czochralski technique, *Opt. Mater.* 37 (2014) 132–138. doi:10.1016/j.optmat.2014.05.012.
- [70] C. Wang, G. Yang, Thermodynamics of metastable phase nucleation at the nanoscale, *Mater. Sci. Eng. R-Rep* 49 (6) (2005) 157–202. doi:10.1016/j.mser.2005.06.002.
- [71] L. Sancey, V. Motto-Ros, B. Busser, S. Kotb, J. M. Benoit, A. Piednoir, F. Lux, O. Tillement, G. Panczer, J. Yu, Laser spectrometry for multi-elemental imaging of biological tissues, *Sci. Rep.* 4 (2014) . doi:10.1038/srep06065.
- [72] A. Knight, N. Scherbarth, D. Cremers, M. Ferris, Characterization of laser-induced breakdown spectroscopy (LIBS) for application to space exploration, *Appl. Spectrosc.* 54 (3) (2000) 331–340. doi:10.1366/0003702001949591.
- [73] B. Salle, J. Lacour, P. Mauchien, P. Fichet, S. Maurice, G. Manhes, Comparative study of different methodologies for quantitative rock analysis by laser-induced breakdown spectroscopy in a simulated martian atmosphere, *Spectrochim. Acta Part B* 61 (3) (2006) 301–313. doi:10.1016/j.sab.2006.02.003.

- [74] M. Tofanelli, L. Pardini, M. Borrini, F. Bartoli, A. Bacci, A. D'Ulivo, E. Pitzalis, M. C. Mascherpa, S. Legnaioli, G. Lorenzetti, S. Pagnotta, G. d. H. Cavalcanti, M. Lezzerini, V. Palleschi, Spectroscopic analysis of bones for forensic studies, *Spectrochim. Acta Part B* 99 (2014) 70–75. doi:10.1016/j.sab.2014.06.006.
- [75] R. L. Kurucz, SYNTHE spectrum synthesis programs and line data, 1993.
- [76] A. Kramida, Y. Ralchenko, J. Reader, N. A. Team, NIST Atomic Spectra Database (ver. 5.1) (2013).
- [77] E. Negre, V. Motto-Ros, F. Pelascini, S. Lauper, D. Denis, J. Yu, On the performance of laser-induced breakdown spectroscopy for quantitative analysis of minor and trace elements in glass, *J. Anal. At. Spectrom.* 30 (2) (2015) 417–425. doi:10.1039/c4ja00363b.
- [78] J. F. Lagrange, J. Hermann, J. Wolfman, O. Motret, Dynamical plasma study during $CaCu_3Ti_4O_{12}$ and $Ba_{0.6}Sr_{0.4}TiO_3$ pulsed laser deposition by local thermodynamic equilibrium modelling, *J. Phys. D: Appl. Phys.* 43 (28) (2010) 285202. doi:10.1088/0022-3727/43/28/285202.
- [79] J. Hermann, A. Thomann, C. Boulmer, B. Dubreuil, M. De Giorgi, A. Perrone, A. Luches, I. Mihailescu, Plasma diagnostics in pulsed laser tin layer deposition, *J. Appl. Phys.* 77 (7) (1995) 2928–2936. doi:10.1063/1.358708.
- [80] C. Aragon, J. A. Aguilera, Characterization of laser induced plasmas by optical emission spectroscopy: A review of experiments and methods, *Spectrochim. Acta Part B* 63 (9) (2008) 893–916. doi:10.1016/j.sab.2008.05.010.
- [81] J. A. Aguilera, C. Aragon, Multi-element saha-boltzmann and boltzmann plots in laser-induced plasmas, *Spectrochim. Acta Part B* 62 (4) (2007) 378–385. doi:10.1016/j.sab.2007.03.024.
- [82] J. Stark, Beobachtungen über den effekt des elektrischen felde auf spektrallinien i. quereffekt, *Ann. Phys. (Berlin)* 43 (1914) 965–983. doi:10.1002/andp.19143480702.
- [83] H. Griem, *Spectral Line Broadening by Plasmas*, Academic Press, New York, 1974.
- [84] E. Tognoni, G. Cristoforetti, S. Legnaioli, V. Palleschi, Calibration-free laser-induced breakdown spectroscopy: State of the art, *Spectrochim. Acta Part B* 65 (1) (2010) 1–14. doi:10.1016/j.sab.2009.11.006.
- [85] J. Hermann, C. Gerhard, E. Axente, C. Dutouquet, Comparative investigation of laser ablation plumes in air and argon by analysis of spectral line shapes: Insights

- on calibration-free laser-induced breakdown spectroscopy, *Spectrochim. Acta Part B* 100 (2014) 189–196. doi:10.1016/j.sab.2014.08.014.
- [86] B. Kumar, R. K. Thareja, Synthesis of nanoparticles in laser ablation of aluminum in liquid, *J. Appl. Phys.* 108 (6) (2010) . doi:10.1063/1.3486517.
- [87] B. Kumar, R. K. Thareja, Laser ablated copper plasmas in liquid and gas ambient, *Phys. Plasmas* 20 (5) (2013) . doi:10.1063/1.4807041.
- [88] B. Kumar, R. K. Thareja, Growth of titanium nanoparticles in confined plasma, *Phys. Plasmas* 19 (3) (2012) . doi:10.1063/1.3697978.
- [89] J. Lam, V. Motto-Ros, D. Misiak, C. Dujardin, G. Ledoux, D. Amans, Investigation of local thermodynamic equilibrium in laser-induced plasmas: Measurements of rotational and excitation temperatures at long time scales, *Spectrochim. Acta Part B* 101 (2014) 86–92, 7th Euro-Mediterranean Symposium on Laser Induced Breakdown Spectroscopy (EMSLIBS), Bari, ITALY, SEP 16-20, 2013. doi:10.1016/j.sab.2014.07.013.
- [90] H. F. Berg, A. W. Ali, R. Lincke, H. R. Griem, Measurement of stark profiles of neutral and ionized helium and hydrogen lines from shock-heated plasmas in electromagnetic t tubes, *Phys. Rev.* 125 (1) (1962) 199. doi:10.1103/PhysRev.125.199.
- [91] A. M. El Sherbini, H. Hegazy, T. M. El Sherbini, Measurement of electron density utilizing the h alpha-line from laser produced plasma in air, *Spectrochim. Acta Part B* 61 (5) (2006) 532–539. doi:10.1016/j.sab.2006.03.014.
- [92] M. D. Saksena, M. N. Deo, K. Sunanda, S. H. Behere, C. T. Londhe, Fourier transform spectral study of b-2 sigma(+)-x-2 sigma(+) system of alo, *J. Mol. Spectrosc.* 247 (1) (2008) 47–56. doi:10.1016/j.jms.2007.10.002.
- [93] G. R. Hebert, R. W. Nichols, C. Linton, Absolute band strengths for the alo blue-green $B^2\Sigma^+-X^2\Sigma^+$ band system, *J. Quant. Spectrosc. Radiat. Transfer* 23 (2) (1980) 229–235. doi:10.1016/0022-4073(80)90010-2.
- [94] I. Kovacs, *Rotational structure in the spectra of diatomic molecules*, 1969.
- [95] K. Saito, T. Sakka, Y. Ogata, Rotational spectra and temperature evaluation of C_2 molecules produced by pulsed laser irradiation to a graphite-water interface, *J. Appl. Phys.* 94 (9) (2003) 5530–5536. doi:10.1063/1.1614431.

- [96] T. Sakka, K. Saito, Y. Ogata, Emission spectra of the species ablated from a solid target submerged in liquid: vibrational temperature of C_2 molecules in water-confined geometry, *Appl. Surf. Sci.* 197 (2002) 246. doi:10.1016/S0169-4332(02)00373-2.
- [97] H. R. Griem, Validity of local thermal equilibrium in plasma spectroscopy, *Phys. Rev.* 131 (1963) 1170–1176. doi:10.1103/PhysRev.131.1170.
- [98] H. W. Drawin, Validity conditions for local thermodynamic equilibrium, *Z. Phys.* 228 (1969) 99–119. doi:10.1007/BF01397532.
- [99] R. McWhirter, *Plasma Diagnostic Techniques*, Academic Press, New York, 1965.
- [100] G. Cristoforetti, A. De Giacomo, M. Dell'Aglio, S. Legnaioli, E. Tognoni, V. Palleschi, N. Omenetto, Local thermodynamic equilibrium in laser-induced breakdown spectroscopy: Beyond the Mc Whirter criterion, *Spectrochim. Acta Part B* 65 (2010) 86–95. doi:10.1016/j.sab.2009.11.005.
- [101] G. Cristoforetti, E. Tognoni, L. A. Gizzi, Thermodynamic equilibrium states in laser-induced plasmas: From the general case to laser-induced breakdown spectroscopy plasmas, *Spectrochim. Acta Part B* 90 (2013) 1–22. doi:10.1016/j.sab.2013.09.004.
- [102] M. A. Gigosos, M. A. Gonzalez, V. Cardenoso, Computer simulated balmer-alpha, -beta and -gamma stark line profiles for non-equilibrium plasmas diagnostics, *Spectrochim. Acta Part B* 58 (8) (2003) 1489 – 1504. doi:10.1016/S0584-8547(03)00097-1.
- [103] A. Phelps, C. Greene, J. Burke, Collision cross sections for argon atoms with argon atoms for energies from 0.01 eV to 10 keV, *J. Phys. B: At. Mol. Opt. Phys.* 33 (16) (2000) 2965–2981. doi:10.1088/0953-4075/33/16/303.
- [104] P. J. Bruggeman, N. Sadeghi, D. C. Schram, V. Linss, Gas temperature determination from rotational lines in non-equilibrium plasmas: A review, *Plasma Sources Science and Technology* 23 (2) (2014) 023001. doi:10.1088/0963-0252/23/2/023001.
- [105] M. Pak, M. Gordon, Potential energy surfaces for the $Al+O_2$ reaction, *J. Chem. Phys.* 118 (10) (2003) 4471–4476. doi:10.1063/1.1542873.
- [106] F. Rezaei, P. Karimi, S. Tavassoli, Effect of self-absorption correction on LIBS measurements by calibration curve and artificial neural network, *Appl. Phys. B* 114 (4) (2014) 591–600. doi:10.1007/s00340-013-5566-3.

- [107] J. Hermann, C. Boulmer-Leborgne, D. Hong, Diagnostics of the early phase of an ultraviolet laser induced plasma by spectral line analysis considering self-absorption, *J. Appl. Phys.* 83 (2) (1998) 691–696. doi:[10.1063/1.366639](https://doi.org/10.1063/1.366639).
- [108] A. C. Woods, C. G. Parigger, Diatomic molecular emission spectroscopy of laser-induced titanium plasma, Vol. 548 of *JPCS*, 2014. doi:[10.1088/1742-6596/548/1/012037](https://doi.org/10.1088/1742-6596/548/1/012037).
- [109] J. Hermann, A. Perrone, C. Dutouquet, Analyses of the tio-gamma system for temperature measurements in a laser-induced plasma, *J. Phys. B-At. Mol. Opt. Phys.* 34 (2) (2001) 153–164. doi:[10.1088/0953-4075/34/2/303](https://doi.org/10.1088/0953-4075/34/2/303).
- [110] J. Phillips, Molecular constants of the tio molecule, *Astrophys. J. Suppl. Ser.* 26 (232) (1973) 313–331. doi:[10.1086/190283](https://doi.org/10.1086/190283).
- [111] R. Ram, P. Bernath, M. Dulick, L. Wallace, The a(3)phi-x-3 delta system (gamma bands) of tio: Laboratory and sunspot measurements, *Astrophys. J. Suppl. Ser.* 122 (1) (1999) 331–353. doi:[10.1086/313212](https://doi.org/10.1086/313212).
- [112] M. Volmer, A. Weber, Germ-formation in oversaturated figures., *Z. Phys. Chem.* 119 (3/4) (1926) 277–301.
- [113] L. Farkas, The speed of germinative formation in over saturated vapours., *Z. Phys. Chem.* 125 (3/4) (1927) 236–242.
- [114] R. Becker, W. Döring, Kinetische behandlung der keimbildung in übersättigten dämpfen, *Annalen der Physik* 416 (8) (1935) 719–752. doi:[10.1002/andp.19354160806](https://doi.org/10.1002/andp.19354160806).
- [115] I. Ford, Statistical mechanics of nucleation: a review, *Proc. Inst. Mech. Eng. Part C-J. Eng. Mech. Eng. Sci.* 218 (8) (2004) 883–899. doi:[10.1243/0954406041474183](https://doi.org/10.1243/0954406041474183).
- [116] E. Clouet, Modeling of Nucleation Processes, *ArXiv e-prints*[arXiv:1001.4131](https://arxiv.org/abs/1001.4131).
- [117] F. F. Abraham, *Homogeneous Nucleation Theory; The Pretransition Theory of Vapor Condensation*, Academic Pr, 1973.
- [118] J. W. P. Schmelzer (Ed.), *Nucleation Theory and Applications*, 1st Edition, Wiley-VCH, 2005.
- [119] D. Chakraborty, G. N. Patey, How crystals nucleate and grow in aqueous NaCl solution, *J. Phys. Chem. Lett.* 4 (4) (2013) 573–578. doi:[10.1021/jz302065w](https://doi.org/10.1021/jz302065w).

- [120] R. Strey, P. Wagner, Y. Viisanen, The problem of measuring homogeneous nucleation rates and the molecular contents of nuclei: Progress in the form of nucleation pulse measurements, *J. Phys. Chem.* 98 (32) (1994) 7748–7758. doi:[10.1021/j100083a003](https://doi.org/10.1021/j100083a003).
- [121] J. Diemand, R. Angelil, K. K. Tanaka, H. Tanaka, Direct simulations of homogeneous bubble nucleation: Agreement with classical nucleation theory and no local hot spots, *Phys. Rev. E* 90 (5) (2014) 052407. doi:[10.1103/PhysRevE.90.052407](https://doi.org/10.1103/PhysRevE.90.052407).
- [122] Y. Viisanen, R. Strey, H. Reiss, Homogeneous nucleation rates of water, *J. Chem. Phys.* 99 (6) (1993) 4680–4692. doi:[10.1063/1.466066](https://doi.org/10.1063/1.466066).
- [123] Y. Viisanen, R. Strey, Homogeneous nucleation rates of n-butanol, *J. Chem. Phys.* 101 (9) (1994) 7835–7843. doi:[10.1063/1.468208](https://doi.org/10.1063/1.468208).
- [124] J. Hruby, Y. Viisanen, R. Strey, Homogeneous nucleation rates for n-pentanol in argon: Determination of the critical cluster size, *J. Chem. Phys.* 104 (13) (1996) 5181–5187. doi:[10.1063/1.471145](https://doi.org/10.1063/1.471145).
- [125] R. Tolman, The effect of droplet size on surface tension, *J. Chem. Phys.* 17 (3) (1949) 333–337. doi:[10.1063/1.1747247](https://doi.org/10.1063/1.1747247).
- [126] J. Lothe, G. Pound, Reconsiderations of nucleation theory, *J. Chem. Phys.* 36 (8) (1962) 2080–&. doi:[10.1063/1.1732832](https://doi.org/10.1063/1.1732832).
- [127] A. Dillmann, G. Meier, Homogeneous nucleation of supersaturated vapors, *Chem. Phys. Lett.* 160 (1) (1989) 71–74. doi:[10.1016/0009-2614\(89\)87558-X](https://doi.org/10.1016/0009-2614(89)87558-X).
- [128] A. Dillmann, G. Meier, A refined droplet approach to the problem of homogeneous nucleation from the vapor phase, *J. Chem. Phys.* 94 (5) (1991) 3872–3884. doi:[10.1063/1.460663](https://doi.org/10.1063/1.460663).
- [129] G. Martin, Reconciling the classical nucleation theory and atomic scale observations and modeling, *Adv. Eng. Mater.* 8 (12) (2006) 1231–1236. doi:[10.1002/adem.200600247](https://doi.org/10.1002/adem.200600247).
- [130] C. R. A. Catlow, S. T. Bromley, S. Hamad, M. Mora-Fonz, A. A. Sokol, S. M. Woodley, Modelling nano-clusters and nucleation, *Phys. Chem. Chem. Phys.* 12 (2010) 786–811. doi:[10.1039/B916069H](https://doi.org/10.1039/B916069H).
- [131] G. Lee, C. Helling, H. Giles, S. T. Bromley, Dust in brown dwarfs and extra-solar planets iv. assessing (TiO_2) and sio nucleation for cloud formation modelling, *Astron. Astrophys.* 575 (2015) A11. doi:[10.1051/0004-6361/201424621](https://doi.org/10.1051/0004-6361/201424621).

- [132] J. Langer, L. Turski, Hydrodynamic model of the condensation of a vapor near its critical point, *Phys. Rev. A* 8 (6) (1973) 3230–3243. doi:10.1103/PhysRevA.8.3230.
- [133] J. Langer, Statistical decay of metastable states, *Ann. Phys.* 54 (2) (1969) 258. doi:10.1016/0003-4916(69)90153-5.
- [134] J. Lothe, Simplified considerations of the onsager symmetry in the general diffusion equation of nucleation theory, *J. Chem. Phys.* 45 (7) (1966) 2678. doi:10.1063/1.1727991.
- [135] J. Langer, Theory of the condensation point, *Ann. Phys.* 41 (1) (1967) 108. doi:10.1016/0003-4916(67)90200-X.
- [136] D. Oxtoby, Homogeneous nucleation: theory and experiment, *J. Phys.-Condes. Matter* 4 (38) (1992) 7627–7650. doi:10.1088/0953-8984/4/38/001.
- [137] M. Born, R. Oppenheimer, Quantum theory of molecules, *Ann. Phys.(Berlin)* 84 (20) (1927) 0457–0484.
- [138] D. Young, *Computational Chemistry: A Practical Guide for Applying Techniques to Real World Problems*, 1st Edition, Wiley-Interscience, 2001. doi:10.1002/0471220655.
- [139] E. G. Lewars, *Computational Chemistry: Introduction to the Theory and Applications of Molecular and Quantum Mechanics*, 2nd Edition, Springer, 2011. doi:10.1007/978-90-481-3862-3.
- [140] C. J. Cramer, *Essentials of Computational Chemistry: Theories and Models*, 2nd Edition, Wiley, 2004. doi:10.1007/s00214-002-0380-8.
- [141] S. Desai, H. Wu, C. Rohlfing, L. Wang, A study of the structure and bonding of small aluminum oxide clusters by photoelectron spectroscopy: $Al_xO_y^-$ ($x=1-2$, $y=1-5$), *J. Chem. Phys.* 106 (4) (1997) 1309–1317. doi:10.1063/1.474085.
- [142] T. Ghanty, E. Davidson, Theoretical interpretation of the photoelectron spectra of $(Al_3O_2)^-$ and $(Al_3O_3)^-$, *J. Phys. Chem. A* 103 (45) (1999) 8985–8993. doi:10.1021/jp9925839.
- [143] A. Patzer, C. Chang, E. Sedlmayr, D. Sulzle, A density functional study of small Al_xO_y ($x,y=1-4$) clusters and their thermodynamic properties, *Eur. Phys. J. D* 32 (3) (2005) 329–337. doi:10.1140/epjd/e2005-00026-8.
- [144] C. Chang, A. Patzer, E. Sedlmayr, T. Steinke, D. Sulzle, Electronic structure investigation of the Al_4O_4 molecule, *Chem. Phys. Lett.* 324 (1-3) (2000) 108–114. doi:10.1016/S0009-2614(00)00579-0.

- [145] A. B. Rahane, M. D. Deshpande, V. Kumar, Structural and electronic properties of $(Al_2O_3)_n$ clusters with $n=1-10$ from first principles calculations, *J. Phys. Chem. C* 115 (37) (2011) 18111–18121. doi:10.1021/jp2050614.
- [146] R. Li, L. Cheng, Structural determination of $(al_2o_3)_n$ ($n=1-7$) clusters based on density functional calculation, *Comp. Theor. Chem.* 996 (2012) 125–131. doi:10.1016/j.comptc.2012.07.027.
- [147] A. S. Sharipov, B. I. Loukhovitski, A. M. Starik, Theoretical study of structure and physical properties of $(Al_2O_3)_n$ clusters, *Physica Scripta* 88 (5) (2013) 058307. doi:10.1088/0031-8949/88/05/058307.
- [148] S. M. Woodley, Atomistic and electronic structure of $(X_2O_3)_n$ nanoclusters; $n=1-5$, $x = b, al, ga, in$ and tl , *Proc. R. Soc. A-Math. Phys. Eng. Sci.* 467 (2131) (2011) 2020–2042. doi:10.1098/rspa.2011.0009.
- [149] J. Sun, W.-C. Lu, W. Zhang, L.-Z. Zhao, Z.-S. Li, C.-C. Sun, Theoretical study on $(Al_2O_3)_n$ ($n=1-10$ and 30) fullerenes and h-2 adsorption properties, *Inorg. Chem.* 47 (7) (2008) 2274–2279. doi:10.1021/ic7011364.
- [150] Y. Gu, Q. Di, M. Lin, K. Tan, Theoretical study of medium-sized clusters of $(Al_2O_3)_n$ - from single cage to core-shell cage, *Comput. Theor. Chem.* 981 (2012) 86–89. doi:10.1016/j.comptc.2011.11.051.
- [151] J. J. P. Stewart, Optimization of parameters for semiempirical methods I. method, *J. Comput. Chem.* 10 (2) (1989) 209–220. doi:10.1002/jcc.540100208.
- [152] M. J. Frisch, G. W. Trucks, H. B. Schlegel, G. E. Scuseria, M. A. Robb, J. R. Cheeseman, G. Scalmani, V. Barone, B. Mennucci, G. A. Petersson, H. Nakatsuji, M. Caricato, X. Li, H. P. Hratchian, A. F. Izmaylov, J. Bloino, G. Zheng, J. L. Sonnenberg, M. Hada, M. Ehara, K. Toyota, R. Fukuda, J. Hasegawa, M. Ishida, T. Nakajima, Y. Honda, O. Kitao, H. Nakai, T. Vreven, J. A. Montgomery, Jr., J. E. Peralta, F. Ogliaro, M. Bearpark, J. J. Heyd, E. Brothers, K. N. Kudin, V. N. Staroverov, R. Kobayashi, J. Normand, K. Raghavachari, A. Rendell, J. C. Burant, S. S. Iyengar, J. Tomasi, M. Cossi, N. Rega, J. M. Millam, M. Klene, J. E. Knox, J. B. Cross, V. Bakken, C. Adamo, J. Jaramillo, R. Gomperts, R. E. Stratmann, O. Yazyev, A. J. Austin, R. Cammi, C. Pomelli, J. W. Ochterski, R. L. Martin, K. Morokuma, V. G. Zakrzewski, G. A. Voth, P. Salvador, J. J. Dannenberg, S. Dapprich, A. D. Daniels, O. Farkas, J. B. Foresman, J. V. Ortiz, J. Cioslowski, D. J. Fox, Gaussian 09 Revision D.01, gaussian Inc. Wallingford CT 2009.

- [153] S. Callard, B. Masenelli, A. Gagnaire, J. Joseph, Dielectric film deposition for optical applications, *Vide-Sci. Techn. Appl.* 54 (1999) 58. doi:10.1088/0034-4885/33/1/305.
- [154] C. Martinet, V. Paillard, A. Gagnaire, J. Joseph, Deposition of sio2 and tio2 thin films by plasma enhanced chemical vapor deposition for antireflection coating, *J. Non-Cryst. Solids* 216 (1997) 77. doi:10.1016/S0022-3093(97)00175-0.
- [155] A. Pillonnet, A. Pereira, O. Marty, C. Champeaux, Valence state of europium doping ions during pulsed-laser deposition, *J. Phys. D-Appl. Phys.* 44 (2011) 375402. doi:10.1088/0022-3727/44/37/375402.
- [156] T. Tsuji, Y. Tsuboi, N. Kitamura, M. Tsuji, Microsecond-resolved imaging of laser ablation at solid-liquid interface: investigation of formation process of nano-size metal colloids, *Appl. Surf. Sci.* 229 (1-4) (2004) 365–371. doi:10.1016/j.apsusc.2004.02.013.
- [157] T. Tsuji, Y. Okazaki, Y. Tsuboi, M. Tsuji, Nanosecond time-resolved observations of laser ablation of silver in water, *Jpn. J. Appl. Phys. Part 1 - Regul. Pap. Brief Commun. Rev. Pap.* 46 (4A) (2007) 1533–1535. doi:10.1143/JJAP.46.1533.
- [158] T. Tsuji, D. H. Thang, Y. Okazaki, M. Nakanishi, Y. Tsuboi, M. Tsuji, Preparation of silver nanoparticles by laser ablation in polyvinylpyrrolidone solutions, *Appl. Surf. Sci.* 254 (16) (2008) 5224–5230. doi:10.1016/j.apsusc.2008.02.048.
- [159] L. Berthe, R. Fabbro, P. Peyre, L. TOLLIER, E. Bartnicki, Shock waves from a water-confined laser-generated plasma, *J. Appl. Phys.* 82 (6) (1997) 2826–2832. doi:10.1063/1.366113.
- [160] A. De Giacomo, M. Dell’Aglia, A. Santagata, R. Gaudiuso, O. De Pascale, P. Wagnener, G. C. Messina, G. Compagnini, S. Barcikowski, Cavitation dynamics of laser ablation of bulk and wire-shaped metals in water during nanoparticles production, *Phys. Chem. Chem. Phys.* 15 (9) (2013) 3083–3092. doi:10.1039/c2cp42649h.
- [161] V. Lazic, S. Jovicevic, M. Carpanese, Laser induced bubbles inside liquids: Transient optical properties and effects on a beam propagation, *Appl. Phys. Lett.* 101 (5) (2012) . doi:10.1063/1.4739851.
- [162] T. Bergman, F. Incropera, A. Lavine, *Fundamentals of Heat and Mass Transfer*, Wiley, 2011.
- [163] A. Tamura, A. Matsumoto, K. Fukami, N. Nishi, T. Sakka, Simultaneous observation of nascent plasma and bubble induced by laser ablation in water with various pulse durations, *J. Appl. Phys.* 117 (17) (2015) . doi:10.1063/1.4919729.

- [164] J. Lombard, T. Biben, S. Merabia, [Nanobubbles around plasmonic nanoparticles: Thermodynamic analysis](#), *Phys. Rev. E* 91 (2015) 043007. doi:[10.1103/PhysRevE.91.043007](#).
URL <http://link.aps.org/doi/10.1103/PhysRevE.91.043007>
- [165] S. A. Menchón, C. A. Condat, Cancer growth: Predictions of a realistic model, *Phys. Rev. E* 78 (2008) 022901. doi:[10.1103/PhysRevE.78.022901](#).
- [166] W. Press, P. Schechter, Formation of Galaxies and Clusters of Galaxies by Self-Similar Gravitational Condensation, *Astrophys. J* 187 (3) (1974) 425–438. doi:[10.1086/152650](#).
- [167] L. M. A. Bettencourt, The origins of scaling in cities, *Science* 340 (6139) (2013) 1438–1441. doi:[10.1126/science.1235823](#).
- [168] R. Juhász, I. A. Kovács, F. Iglói, Long-range epidemic spreading in a random environment, *Phys. Rev. E* 91 (2015) 032815. doi:[10.1103/PhysRevE.91.032815](#).
- [169] S. Riley, Large-scale spatial-transmission models of infectious disease, *Science* 316 (5829) (2007) 1298–1301. doi:[10.1126/science.1134695](#).
- [170] P. Castorina, P. P. Delsanto, C. Guiot, Classification scheme for phenomenological universalities in growth problems in physics and other sciences, *Phys. Rev. Lett.* 96 (2006) 188701. doi:[10.1103/PhysRevLett.96.188701](#).
- [171] H. Lin, A. Loeb, A Unifying Theory for Scaling Laws of Human Populations, ArXiv e-prints [arXiv:1501.00738v2](#).

Vers la compréhension des processus de croissance en ablation laser en milieu liquide

SUITES aux prédictions de Richard Feynman formulées en Décembre 1959, l'utilisation des nanomatériaux suscite aujourd'hui un intérêt grandissant dans de nombreux domaines, allant de la médecine à l'optique, en passant par la mécanique. Par définition, un nanomatériau est un matériau possédant au moins une de ses longueurs plus petite qu'un millionième de mètre. Cette propriété de taille engendre des propriétés physiques particulières qui confèrent aux matériaux des avantages d'utilisation sans commune mesure. En médecine, par exemple, on constate de nombreuses utilisations de nanoparticules d'or pour le traitement des cancers ou pour l'imagerie médicale. Alors que de nombreuses équipes de recherche ont porté leur attention sur les mécanismes propres aux nanomatériaux, la fabrication même de ces tout petits objets demeure un domaine de recherche en pleine effervescence.

Les méthodes de synthèse par voie chimique ont prouvé par le passé leur capacité à répondre à ce problème réussissant notamment à élaborer une grande famille de dérivés du carbone graphitique. Les nanotubes de carbone, les feuillets de graphène et les fullerènes sont autant d'exemple de l'incroyable réussite de la chimie dans le contrôle de la synthèse de nanomatériaux. Néanmoins, dans certaines circonstances, il peut être nécessaire de se doter d'autres méthodes pour la fabrication de nanomatériaux notamment les matériaux aux stœchiométries complexes. C'est dans ce contexte que s'inscrit l'ablation laser en milieu liquide.

Dans cette méthode, un laser pulsé est focalisé sur une cible solide immergée dans un liquide. Chaque impulsion du laser arrache de la matière qui se recombine au sein du liquide pour former des nanoparticules. La méthode attire de plus en plus d'attention parce qu'elle permet d'obtenir directement une solution colloïdale de nanoparticules sans ajout de molécules complexantes, dans un environnement dénué d'espèces chimiques issues de la synthèse. La stabilité de la solution est alors assurée par les charges en surface qui empêchent les nanoparticules de s'agréger. Cependant, la combinaison des effets physiques provenant de l'interaction du laser avec la cible et des effets chimiques dus à l'utilisation d'un solvant liquide engendre une importante complexité dans la

compréhension des processus de croissance. En effet, quelques centaines de picosecondes après l'impulsion laser, la matière arrachée forme un plasma composé d'électrons, d'ions, d'atomes et de molécules. Les collisions entre les espèces et le gaz d'électrons excitent les niveaux électroniques et la désexcitation engendre une émission de lumière. Le plasma n'est plus optiquement actif lorsque le gaz d'électrons se neutralise c'est-à-dire après quelques microsecondes. On observe alors une bulle de gaz dans laquelle des réactions chimiques entre les espèces arrachées peuvent avoir lieu. La bulle grossit et puis décroît au bout de quelques centaines de microsecondes. La matière se retrouve dans le liquide où les particules peuvent soit s'agréger soit réagir avec les molécules du solvant.

L'enjeu de ce travail de thèse est de comprendre plus en détail ces différents mécanismes et d'élaborer un scénario de la formation des nanoparticules durant l'ablation laser en milieu liquide. Je commencerai par présenter un état de l'art de l'utilisation de la méthode pour la synthèse des nanoparticules. Ensuite, je montrerai que sous certaines conditions, la méthode permet de synthétiser des nanoparticules d'alumine dopées chrome en vue d'applications en tant que sondes de pression. Par la suite, je développerai notre travail concernant la compréhension des processus de croissance amenant les atomes ablatés à se recombiner pour former des nanoparticules.

Premièrement, pendant la phase plasma, la lumière émise par les espèces excitées permet de caractériser certaines propriétés thermodynamiques du système. En effet, chaque espèce chimique possède un diagramme d'énergie singulier et la distribution spectrale de la lumière émise en est une signature. En collectant la lumière et en la résolvant en longueur d'onde, on est ainsi capable de déterminer la composition chimique du plasma. Par ailleurs, la répartition des populations dans les niveaux excités est déterminée par la température en tant qu'outil statistique. En comparant les rapports d'intensité de lumière provenant de la même espèce chimique mais de différents niveaux électroniques, on parvient à mesurer la température du plasma. Ces méthodes sont bien connues et déjà employées en milieu gazeux. C'est ce qu'on appelle la spectroscopie sur plasma induit par laser ou LIBS (pour Laser-induced breakdown spectroscopy). Notre travail a été d'appliquer ces méthodes à l'environnement liquide, où des difficultés expérimentales apparaissent, dues en grande partie au confinement spatial et temporel engendré par le liquide. Après avoir démontré la possibilité d'appliquer la LIBS en milieu liquide, nous avons soulevé l'intérêt de l'utilisation d'espèces diatomiques pour la mesure de la température. Nous avons alors cherché à étendre la notion d'équilibre thermodynamique dans un gaz moléculaire. Nos études ont permis notamment d'établir l'absence d'équilibre entre les températures électroniques des ions et des atomes d'une part et la température rotationnelle des molécules d'autre part.

Deuxièmement, lorsque le plasma n'est plus optiquement actif la composition chimique ne peut plus être sondée expérimentalement. Cependant, les atomes continuent de réagir pour former des molécules de plus en plus grandes jusqu'à une certaine distribution de taille que l'on pourrait assimiler classiquement à un noyau de nucléation. Dès lors, le mécanisme permettant aux particules de grandir n'est plus piloté par la chimie mais par l'agrégation de ces objets. Nous proposons d'utiliser les outils de la chimie quantique pour retracer le scénario du processus amenant à l'apparition du noyau de nucléation. Dans un premier temps, les structures géométriques les plus stables pour les molécules Al_xO_y avec x et y allant de 1 à 12 sont déterminées à l'aide de méthodes de chimie quantique. La prépondérance de ces molécules est tracée pour différentes températures et pressions, à l'aide d'un modèle théorique combinant les résultats des simulations numériques à la thermochimie des équilibres. Ces résultats purement théoriques sont comparés aux résultats expérimentaux de spectroscopie des plasmas. Un bon accord est obtenu aux hautes températures lorsque le plasma est encore optiquement actif. Cela permet d'étendre l'étude aux basses températures. On observe l'émergence de Al_8O_{12} semblant indiquer qu'il s'agit là du noyau de nucléation, première brique amenant la formation des nanoparticules d'oxide d'aluminium $(\text{Al}_2\text{O}_3)_n$.

Troisièmement, nous avons étudié la dynamique de la bulle induite par ablation laser en milieu liquide. Pour cela, une caméra ultra-rapide a été utilisée afin d'acquérir par ombrographie des images de la bulle. Une telle méthode permet de s'affranchir des problèmes de reproductibilité dus aux fluctuations du laser et à l'état de la cible. Ensuite, nous avons développé une méthode analytique basée sur l'équation de Rayleigh-Plesset. L'étude permet alors de calculer la pression et la température au sein de la bulle. En traçant la pression en fonction du volume, on observe une évolution en loi de puissance dont on déduit plusieurs propriétés pour l'évolution de la bulle: (i) le système est adiabatique, (ii) le gaz peut être assimilé à un gaz parfait (iii) la bulle est majoritairement composée de solvants, (iv) la quantité de matière ne varie pas de manière significative.

Pour conclure, dans ce manuscrit de thèse, il est présenté un travail varié où différentes méthodes ont été employées afin d'étudier les mécanismes présents durant l'ablation laser en milieu liquide. Des nanoparticules d'alumine dopées chrome ont été obtenues et caractérisées, à la fois en microscopie et en luminescence sous pression. Ensuite, la spectroscopie des plasmas a permis d'étudier quantitativement les propriétés thermodynamiques du plasma et d'en déduire la composition chimique, la densité électronique et la température. Cela a soulevé de nombreuses questions concernant l'équilibre thermodynamique. Un premier travail prospectif tente de résoudre ces interrogations. Par la suite, la nucléation des nanoparticules a été étudiée à l'aide d'outils de la chimie quantique. Nous avons démontré que Al_8O_{12} pourrait être considéré comme le noyau

de nucléation, permettant la croissance de nanoparticules d'alumine. Enfin, nous avons examiné la dynamique de la bulle et nous avons montré qu'elle est majoritairement composée de molécules du solvant dont la quantité de matière ne varie quasiment pas. Ce travail a permis la publication de plusieurs articles dont vous pourrez trouver les références à la fin de ce manuscrit.

List of publications

1. J. Lam, J. Lombard, C. Dujardin, G. Ledoux, S. Merabia and D. Amans, “Dynamical study of bubble expansion following laser ablation in liquids”, *in preparation*.
2. J. Lam, D. Amans, C. Dujardin, G. Ledoux and A-R. Allouche, “**Atomistic Mechanisms for the Nucleation of Aluminium Oxide Nanoparticles**”, *J. Phys. Chem. A* **119**, 8944-8949 (2015).
3. J. Lam, V. Motto-Ros, D. Misiak, C. Dujardin, G. Ledoux, D. Amans, “**Investigation of Local Thermodynamic Equilibrium in Laser-induced Plasmas: Measurements of Rotational and Excitation Temperatures at Long Time Scales**”, *Spectrochimica Acta Part B* **101**, 86–92 (2014).
4. J. Lam, D. Amans, F. Chaput, M. Diouf, G. Ledoux, N. Mary, K. Masenelli-Varlot, V. Motto-Ros and C. Dujardin , “ **γ -Al₂O₃ nanoparticles synthesized by pulsed laser ablation in liquids: A plasma analysis**”, *Phys. Chem. Chem. Phys.* **16**, 963-97 (2014).

Pulsed Laser Ablation in Liquid: towards the comprehension of the growth processes

When a pulsed-laser is focused into a solid target immersed in water, the material is evaporated. Nucleation and growth occur in the liquid and nanoparticles are synthesized. The method can be considered as versatile because one can try to synthesize any kinds of materials. Also, the nanoparticles are directly stabilized by the solvent so there is no need of complexing agents. The nanoparticles are described as ligand-free. However, various processes can occur during the synthesis and the aim of my work is to understand these different components.

Since the laser ablation in liquid displays a wide range of timescales, we used numerous methods to address this problem. First, I will present the use of plasma spectroscopy and the questions it raises towards local thermodynamic equilibrium. Then, I will describe our microscopic approach of nucleation based on quantum chemistry techniques. Finally, I will illustrate the advantages of shadowgraphic measurements to reach a hydrodynamic understanding of the system.

Keywords: Laser ablation in liquid, nucleation, LIBS, molecular plasma, local thermodynamic equilibrium, DFT, aluminum oxide

Vers la compréhension des processus de croissance en ablation laser en milieu liquide

Lorsqu'une impulsion laser est focalisée sur une cible solide immergée dans un liquide, de la matière est vaporisée. La nucléation et la croissance ont lieu dans le liquide et des nanoparticules sont ainsi synthétisées. La méthode est très polyvalente puisqu'une grande variété de matériaux peut être générée. De plus, les nanoparticules sont directement stabilisées dans le solvant. L'ajout d'agent complexant n'est pas nécessaire mais peut tout de même permettre de mieux contrôler la taille des nanoparticules.

Cependant, de nombreux processus sont mis en jeu durant la synthèse et l'objectif de ce travail doctoral est de développer la compréhension de ces éléments. Dans la mesure où l'ablation laser déploie une multitude d'échelle de temps, il a fallu employer différentes méthodes pour élucider ces mécanismes. Pour commencer, je définirai un état de l'art de l'utilisation de l'ablation laser en milieu liquide et nos résultats concernant la synthèse d'aluminium oxyde dopé chrome. Par la suite, je présenterai la spectroscopie des plasmas et les questions sous-jacentes à la notion d'équilibre dans un plasma moléculaire. Ensuite, je décrirai notre approche atomistique de la nucléation basée sur les techniques de chimie quantique. Enfin, je montrerai l'apport de l'utilisation des méthodes d'ombrographie pour mieux comprendre la thermodynamique du système au temps plus long. Notre étude démontre que la bulle formée suite à l'ablation laser est constituée essentiellement de molécule du solvant dont la quantité n'évolue quasiment pas au cours du temps de vie de la bulle.

Mots clés: Ablation laser en milieu liquide, nucléation, LIBS, plasma moléculaire, équilibre thermodynamique local, DFT, oxyde d'aluminium